Graduate Theses & Non-Theses   Student Scholarship

Fall 2018

SURFACE CHEMISTRY AND MODELLING OF SALICYL HYDROXAMIC ACID ADSORPTION AT THE SURFACE OF RARE EARTH OXIDES, CARBONATES AND PHOSPHATES

Marc F. Sime
Montana Tech

Follow this and additional works at: https://digitalcommons.mtech.edu/grad_rsch

Part of the Metallurgy Commons

Recommended Citation

SURFACE CHEMISTRY AND MODELLING OF SALICYL HYDROXAMIC

ACID ADSORPTION AT THE SURFACE OF RARE EARTH OXIDES,

CARBONATES AND PHOSPHATES

by

Marc Freddy Sime

A thesis submitted in partial fulfillment of the

requirements for the degree of

Master of Science in Metallurgical and Mineral Processing Engineering

Montana Technological University

2018

Abstract

The adsorption mechanism of salicyl hydroxamic acid (SHA, $C_7H_7O_3N$) on rare earth minerals was investigated using two complementary methods: precipitation studies and modelling. Precipitation studies showed that SHA adsorption occurs through a displacement of the hydroxide ion at the surface in an ion exchange mechanism, leading to surface precipitation and/or chemisorption. Surface precipitation predominates in the light rare earth oxides (LREOs), while chemisorption predominates in the heavier REOs. Modelling revealed that adsorption of SHA on the REM surface is dependent upon the orientation of SHA on the surface as well as the distance between rare earth elements sites on the surface. It was concluded that surface precipitation predominates in the LREOs and in the heavy rare earth carbonates (HRECs), while chemisorption predominates in the HREOs and in the light rare earth carbonates (LRECs). With the rare earth phosphates, both chemisorption and surface precipitation are observed all across.

Dedication

This work is dedicated to my mom (Toussi Berthe), late dad (Sime Appolos), my seven siblings (Evelyn Joundzo, Jacob Fosso, Stephanie Tsinkou, Carine Tchouankam, Romain Tande, William Fonkou and Danielle Popwouo), my cousins, uncles and aunts for their constant and unconditional support and prayers. It is also dedicated to all the poor people and countries of the world. You have always been my highest source of motivation, and undoubtedly receive as much care as I can reasonably give throughout my life.

Acknowledgements

First and foremost, I would like shower my thesis advisor, Dr. Courtney Young, with thanks and praise. His patience, fatherly guidance and holistic approach to coaching the renegade that I am is the only reason I could complete this thesis. Secondly, I would like to thank Dr. Avimanyu Das for his tirelessness as an assistant coach to Dr. Courtney Young. Thirdly, I would like to thank Dr. Doug Coe, my third committee member, who accepted to work with me at the last minute; Dr. David Hobbs, Dr. Michael Webb and Dr. Doug Cameron, Dr. Hsin Huang for their help in acquiring and analyzing data. It was with gratitude that I continued on the path traced by William Nicholas, Rick LaDouceur, Greer Galt and Stephanie Trant, the previous and current graduate students who worked and are working on this project. Last, but most importantly, I would like to thank the Army Research Laboratory (ARL) for providing the funding necessary to complete this work.

Table of Contents

List of Tables

List of Figures

List of Equations

List of Acronyms and Important Chemical Symbols

Sc: Scandium

Y: Yttrium

La: Lanthanum

Ce: Cerium

Pr: Praseodymium

Nd: Neodymium

Pm: Promethium

Sm: Samarium

Eu: Europium

Gd: Gadolinium

Tb: Terbium

Dy: Dysprosium

Ho: Holmium

Er: Erbium

Tm: Thulium

Yb: Ytterbium

Lu: Lutetium

HCl: Hydrochloric acid

SHA: Salicylhydroxamic acid

HREEs: Heavy Rare Earth Elements

LREEs: Light Rare Earth Elements

MREEs: Medium Rare Earth Elements

REOs: Rare Earth Oxides

RECs: Rare Earth Carbonates

REPs: Rare Earth Phosphates

REMs: Rare Earth Minerals

NaOH: Sodium Hydroxide

XRPD: X-Ray Powder Diffraction

LRS: Laser Raman Spectroscopy

MW: Molecular Weight

ICDD: International Center for Diffraction Data

PDXL: Rigaku®'s Integrated X-Ray Powder Diffraction Software

USA: United States of America

LB: Langmuir-Blodgett

1. Introduction

According to the US Department of Energy, the Rare Earth Elements (REEs) are "technology metals". For the Japanese, they are the "seed of technology". REEs have weaved their way into the present high tech society, and have become indispensable to miniaturizing electronics. In their metallic state, they can combine with other metals to give alloys that make excellent batteries (e.g. NimH), superalloys, or steels; They also make excellent permanent magnets useful in motors and generators, HD Drives, Microphones and speakers, Magnetic Resonance Imaging, Magnetic Refrigeration, etc. Other uses for their metallic forms are pigment manufacturing and in the nuclear industry. In their oxidized forms, they are useful as phosphors in LED lamps, lasers, flat panel displays, fluorescent lamps, X-ray imaging, optical sensors and optical fibers. They are also excellent catalysts for the petroleum industry, for the automotive industry and for water treatment. Their oxides are also excellent in ceramics and glasses. They make UV-resistant glasses, thermal glasses, capacitors, sensors, refractories, and even superconductors.

Rare Earths are the 15 lanthanides in addition to Scandium (Sc) and Yttrium (Y). They are most often classified as light rare earth elements (LREEs) and heavy rare earth elements (HREEs) based on their atomic number and filling of the *4f* orbital. Lanthanum (La), cerium (Ce), praseodymium (Pr), neodymium (Nd), promethium (Pm), samarium (Sm), europium (Eu) and gadolinium are the LREEs, while terbium (Tb), dysprosium (Dy), holmium (Ho), erbium (Er), thulium (Tm) ytterbium (Yb) and lutetium (Lu) are the HREEs. Depending on other considerations, they can also be subdivided to include medium rare earth elements (MREEs). In this case, the first five (La through Pm) would be the LREEs, the middle five (Sm through Dy) would be the MREEs and the last five would be the HREEs. For example, with rare earth oxides

(REOs), the LREOs (La through Pm) are hexagonal, the MREOs (Sm through Dy) are monoclinic, and the HREOs (Ho through Lu) are cubic.

It is an oxymoron to say "abundant rare earths"; however, it is not ironic. REEs are actually quite abundant in the Earth's crust. As can be seen in Figure 1, cerium, for example is as plentiful as copper, and copper is quite abundant (Haxel et. al., 2002). Hence in this regard, "rare" implies finding deposits that are large and concentrated enough for economically feasible beneficiation. Furthermore, it is very difficult to separate individual REEs due to their similar properties. Also, in this figure, Cu and other base metals (Pb, Zn, Co and Ni) have approximately the same abundance as all REEs.
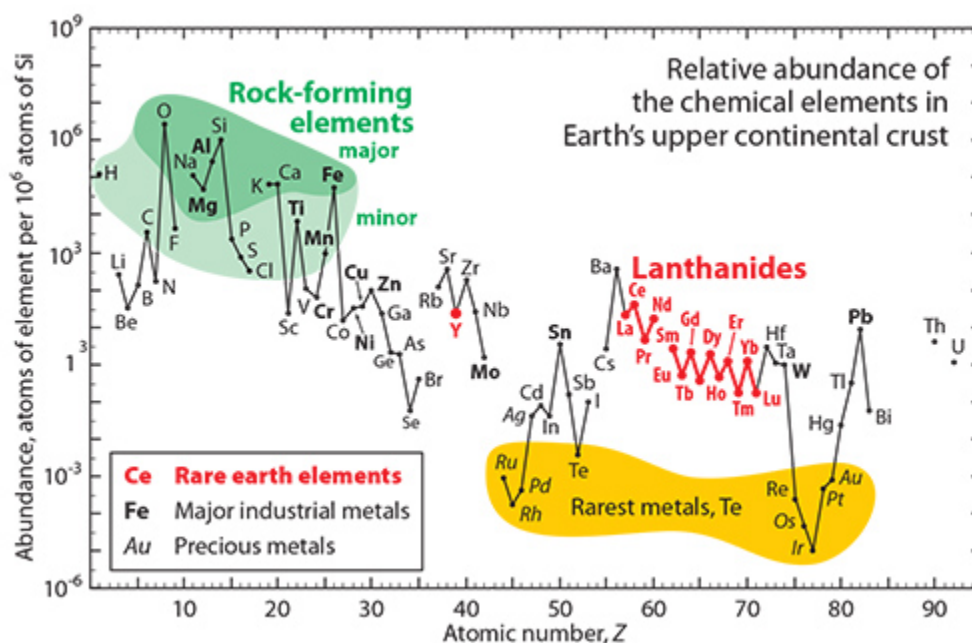
Figure 1: Abundance of elements in the Earth's upper crust (REEs are highlighted in red) (G. Haxel, 2018)

As illustrated in Table I, REEs occur in their oxidized forms, of which the +3 oxidation state dominates. The counter ions in the rare earth minerals (REMs) are usually oxygen, fluoride, carbonate, phosphate and silicate. The REEs often substitute for one another in the mineral

lattice. In addition, they can exchange with other cations (e.g. Ca^{2+}, Fe^{3+}, Na^+) (Kim & Osseo-Asare, 2012; Pavez O., Brandao P. R. G., 1996). Fluorides are often associated with phosphates and carbonates. These phenomena cause REMs to become solid solutions of variable content which create processing problems leading to low recoveries and grade of concentrates.

In this thesis, fundamental studies focus on rare earth oxides (REOs), rare earth carbonates (RECs) and rare earth phosphates (REPs), because they are the three most occurring counter ions to REEs in REMs. Consequently, this research will be applicable to all rare earth deposits.

Table I: Rare Earth Minerals and the Counter Ions Involved.

Rare Earth Mineral	formula	Counter Ion(s) Involved
Aeschynite	$(Y,Ca,Fe,Th)(Ti,Nb)_2(O,OH)_6$	Oxide, Hydroxide
Euxenite	$(Y,Ca,Er,La,Ce,U,Th)(Nb,Ta,Ti)_2O_6$	Oxide
Samarskite	$(Y,Ce,U,Fe)_3(Nb,Ta,Ti)_5O_{16}$	Oxide
Monazite	$(Ce,La)PO_4$	Phosphate
Xenotime	YPO_4	Phosphate
Brockite	$(Ca,Th,Ce)PO_4 \cdot H_2O$	Phosphate
Bastnaesite	$(Ce, La)CO_3F$	Carbonate, Fluoride
Parisite	$Ca(Ce,La)_2(CO_3)_3F_2$	Carbonate, Fluoride

To extract REMs from their ores, flotation is often used. It is a physicochemical hydrometallurgical method that relies on the differences in hydrophobicity between particles in surfaces as established naturally or synthetically. Hydrophobic particles repel water molecules and attach to bubbles (usually air bubbles) in a flotation tank. For REMs, hydrophobicity is not natural and must be imparted by means of surfactants, also called collectors in the case of flotation. A recent study established that the bubbles only account for a fraction of the recovery (LaDouceur, 2018) . A lot of particles reporting to the concentrate are carried by entrainment, depending on their size, particularly if they are small.

The objective of this study was to unravel the adsorption mechanism of salicyl hydroxamic acid (SHA) on the surface REOs. Precipitates of REOs at different concentrations of

SHA were synthesized and analyzed using Laser Raman Spectroscopy (LRS) and X-Ray Powder

Diffractometry (XRPD). The background matrices (also called 0.0M REO-SHA precipitate) as

well as the bulk precipitates of REOs and SHA were synthesized according to a proven

procedure (Feng & Fernando, 1962). They were also analyzed using XRPD and LRS for

comparison purposes. Surface modeling of SHA on REOs was made to confirm the results

obtained. The surface modeling of SHA on RECs and REPs were made to conjecture a

mechanism for them. From the precipitation studies, it became apparent that including RE(SHA)

$_{3 (S)}$ Gibbs free energies in StabCal plots would give a more realistic picture of the solution

modeling.

2. Literature Review

2.1. Rare Earth Elements

2.1.1. Background

As indicated i the introduction, REEs are not "rare" in terms of abundance. They are

simply rarely found in deposits concentrated enough to allow for profitable stewardship. Also,

REEs of similar atomic numbers exhibit very similar properties, and are therefore difficult to

separate (Alonso et al., 2012). Ce and Lu have quite different properties, but Ce and Pr are

similar, so are Pr and Nd, and so are Sm and Eu and so on.

In the present market, some REEs are sought after more than others. Table II adapted

from (Binnemans et al., 2013), illustrates the average use per REE in 2010. It can be seen from

Table II that LREEs and MREEs are on the higher end of the uses.

Table II: Use by Percentages of Application for 10 of the 17 REEs

Application	La	Ce	Pr	Nd	Sm	Eu	Gd	Tb	Dy	Y	Other
magnets			23.4	69.4	3.3		2.0	0.2	5.0		
Battery alloys	50.0	33.4.	3.3	10.0							
Metallurgy	26.0	52.0	5.5	16.5							
Auto catalysts	5.0	90.0	2.0	3.0							
Polishing powders	31.5	65.0	3.5	3.0							
Glass additives	24.0	66.0	1.0							2.0	4.0
Phosphors	8.5	11.0				4.9	1.8	4.6		69.5	
Ceramics	17.0	12.0	6.0	12.0						53.0	
Others	19.0	39.0	4.0	15.0	2.0		1.0			19.0	

The common oxidation state amongst REEs is +3. This is because, in forming ions, REEs

seek to achieve a more stable electronic configuration. Filled orbitals (as in noble gases) and

half-filled orbitals are usually more stable than other occupancies of orbitals. Sc, Y and La, lose

three elections to form Sc^{+3}, Y^{+3} and La^{+3}; Ar, Kr and Xe electronic configurations are formed,

which are stable. The internal *4f*-orbital begins to fill up on Ce. It belongs to the 4th shell. The

outer orbitals occupied on the La row is the 6th shell. The 6th shell is made up of *6s* and *6p*

subshells. After the *6s* is full, electrons populate the *5d* orbital before resuming with the *6p*.

However, electrons, just after populating the first slot in the *5d*-orbital, will populate the *4f*

before continuing to populate the *5d*. The 14 elements after La, starting from Ce, constitute the

lanthanides. Because the *4f* is an inner shell, it takes a lot more energy to remove an electron

from it, unless it is to achieve a full shell (like in the case of Ce^{+4}) or a half-full shell (like in

Tb^{+4}). In most of the other cases, the energy requirement to get an electron out of the *4f*-orbital is

too great for any ligand to stabilize. Thus, the most common oxidation state of REEs is +3. As

noted, Ce^{+4} and Tb^{+4} are also encountered. Certain REEs, to achieve a full or half-filled orbital,

transfer the electron the *5d* to the *4f*, therefore only having two electrons to give up. That

explains why Eu^{+2} and Yb^{+2} are also encountered. Table III summarizes the above discussion.

Table III: REE atomic and Ionic Electronic Configurations

Rare Earth Element	Atomic Electronic Configuration	Ionic Electronic Configuration
Sc	$[Ar]4s^23d^1$	Sc^{+3}: $[Ar]$
Y	$[Kr]5s^24d^1$	Y^{+3}: $[Kr]$
La	$[Xe]6s^25d^1$	La^{+3}: $[Xe]$
Ce	$[Xe]4f^16s^25d^1$	Ce^{+3}: $[Xe]4f^1$; Ce^{+4}: $[Xe]$
Pr	$[Xe]4f^26s^25d^1$	Pr^{+3}: $[Xe]4f^2$
Nd	$[Xe]4f^36s^25d^1$	Nd^{+3}: $[Xe]4f^3$
Pm	$[Xe]4f^46s^25d^1$	Pm^{+3}: $[Xe]4f^4$
Sm	$[Xe]4f^56s^25d^1$	Sm^{+3}: $[Xe]4f^5$
Eu	$[Xe]4f^66s^25d^1$	Eu^{+3}: $[Xe]4f^6$; Eu^{+2}: $[Xe]4f^7$
Gd	$[Xe]4f^76s^25d^1$	Gd^{+3}: $[Xe]4f^7$
Tb	$[Xe]4f^86s^25d^1$	Tb^{+3}: $[Xe]4f^8$; Tb^{+4}: $[Xe]4f^7$
Dy	$[Xe]4f^96s^25d^1$	Dy^{+3}: $[Xe]4f^9$
Ho	$[Xe]4f^{10}6s^25d^1$	Ho^{+3}: $[Xe]4f^{10}$
Er	$[Xe]4f^{11}6s^25d^1$	Er^{+3}: $[Xe]4f^{11}$
Tm	$[Xe]4f^{12}6s^25d^1$	Tm^{+3}: $[Xe]4f^{12}$
Yb	$[Xe]4f^{13}6s^25d^1$	Yb^{+3}: $[Xe]4f^{13}$; Yb^{+2}: $[Xe]4f^{14}$
Lu	$[Xe]4f^{14}6s^25d^1$	Lu^{+3}: $[Xe]4f^{14}$

In the Pauling scale, REEs have very similar electronegativity values (1.12-1.27). Some of their common properties of rare earth elements are their reactions with nitrogen, carbon, hydrogen, selenium, sulfur and phosphorus to form nitrides, carbides, hydrides selenides, sulfates and sulfides, as well as phosphates and phosphides, respectively (Krishnamurthy, N., and Gupta, 2015).

The *4f*-orbital, as already discussed, is an inner orbital. Habitually, inner electrons shield outer electrons from nuclear attraction. Across a row, as the number of protons increase, so does the number of electrons. The size of an atom is determined by the attraction of the nucleus on the outermost electrons and the shielding of the outer electrons by the inner electrons. Across a period, the net effect is such that the size decreases. The *4f*-orbital exhibits poor shielding

properties, such that the outermost electrons are drawn to the nucleus more strongly, thereby allowing the nucleus to have a higher attraction on the outermost electrons, resulting in a greater than expected decrease of atomic size going from La to Ce. The drop in size is noticeable from La to Ce, but from Ce to Lu, the drop in ionic radius is minimal. That explains the similarities in the properties of lanthanides. This "lanthanide contraction" effect is responsible for a great number of properties of REEs (Krishnamurthy, N., and Gupta, 2015). Moving across the lanthanides in the periodic table, it becomes easier to ionize REEs due to the lanthanide contraction (Mackintosh, 1991; Thiel, 2003).

Ionic sizes follow the same trend as atomic sizes. They decrease with increasing atomic number. La^{+3} has a larger size than Lu^{+3}, but both have the same charge. Thus, La^{+3} is less densely charged than Lu^{+3}. According to the Hard Soft Acid Base (HSAB) theory (Pearson, 1963), Lu^{+3} is a harder acid than La^{+3} and would preferably bond with harder bases, such as F^-, O^{2-}. In nature, REEs are mostly found associated with hard counter ions (bases) such as carbonates, phosphates, fluorides and oxides.

Filling of *4f*-orbital brings about lanthanide contraction, which is responsible for all the properties discussed above. Filling the *4f*-orbital also gives rise to different magnetic properties. Magnetic susceptibility in REE tripositive ions increases with atomic number up to Gd, and then decreases until Lu. This is because Gd^{+3} has the highest number of unpaired electrons. Thus, Gd and Dy display the highest magnetic susceptibility; whereas La and Lu exhibit the smallest. The elements Gd and Dy are the most sought after for permanent magnets for various applications (Peter et al., 1999; Ericsson et al., 1995; Günthero dt et al., 1974; Legvold, 1980).

2.1.2. Significance of This Research

This research is of great importance to the US Department of Defense. The USA was the global leader of production of REEs from the 1960s to the 1980s. China has since had a near monopoly, governing about 90-95% of the market due to lower environmental standards and labor costs. Some products, such as the two strongest permanent REE magnets, neodymium iron boron (NeFeB) and samarium cobalt (SmCo) are of great importance to defense, and are currently only produced by China. The USA needs to develop that technology, which starts by producing REEs and stopping the dependence on China (Grasso, 2013).

Hydroxamates are proven to be excellent collectors for REMs. In the past, the USA used octylhydroxamic acid for flotation. Studies show with octylhydroxamic acid, just like other alkyl chain hydroxamates, recovery is temperature dependent (Sreenivas and Padmanabhan, 2002). China, on the other hand, uses salicylic hydroxamic acid, and studies suggest that recovery with it is not affected by temperature (Galt, 2017). This is why it continues to be investigated herein and elsewhere (Trant, 2018).

2.2. Rare Earth Minerals (REMs)

After having demonstrated the importance of focusing on REOs, RECs and REPs on these fundamental studies, it is logical to learn about them individually. Therefore, included in this thesis is a literature survey of REOs, RECs and REPs, with an emphasis on their crystal structures and coordination numbers. Part of this research is a theoretical modeling of the adsorption of SHA on the surface of each REM. Their crystal structures allow for accurate drawings. Coordination numbers are equally important because, with them, it is possible to estimate the size of REE ions based on calculations as determined by (Jia, 1991) from compound type, atomic number, coordination number and oxidation state. He strongly noted that REE ions

can have different sizes depending on the environment. The tables in the ensuing sections will be summaries of the literature. The cationic sizes on oxides are the most accurate, because the calculations were made based on REOs, but they are good estimates for RECs and REPs, given that the REE ions are connected to the anions via oxygen atoms.

2.2.1. Rare Earth Oxides (REOs)

According to (Atkins et al., 2010), all REOs in +3 states exhibit coordination numbers of 7 and 6, with LREEs being 7 and HREEs being 6. Literature reports an ongoing debate as to what elements are considered LREEs and which are considered HREEs. Based on atomic number, the La end will be LREEs, and the Lu end will be HREEs. However, there is a fuzzy line in the middle. Some consider that up to Gd, which has an $f^{\,7}$ (half filled) orbital, to be LREEs, and therefore the HREEs begin with Tb. Others add a transition and refer to them as medium REEs (MREEs). For those that consider the MREEs, once again, depending on the properties under analysis, the boundaries can be different. To solve this problem in the particular case of this study, crystal structures are used. It appears that REOs containing La through Pm exhibit a hexagonal or A-type crystal structure at room temperature (Bärnighausen and Schiller, 1985; Boldish and White, 1979; Zachariasen, 1926); while those from Sm through Lu are cubic or C-type (Zachariasen, 1927). Thus in this study, the hexagonal REEs shall be LREEs, and the cubic HREEs. It is therefore easy to assign the coordination number of 7 to the LREEs (La to Pm), and 6 to the HREEs (Sm to Lu), as shown in Table IV. Temperature dependent polymorphism in all REOs is observed.

At elevated temperature, LREOs transition from hexagonal to monoclinic (B-type), and from monoclinic to cubic at an even higher temperature. (Warshaw and Roy, 1961); (Guentert and Mozzi, 1958); (Atkinson, 2014); (Glushkova and Boganov, 1965). Processing of REMs are

most often performed approximately at room temperature. Therefore, in the modeling, room

temperature REOs crystal structures will be considered. Sc and Y once again confirm their

similarities in properties to the heaviest elements of the lanthanide series by displaying a cubic or

bixbyite-type (Wyckoff, 1963) ;(Paton and Maslen, 1965). In this thesis, Sc and Y were not

researched. Hence, discussions herein involving them will be sparse.

Table IV: REOs Coordination Number by Crystal Structure

REO	Crystal Structure	Coordination Number	Designation
La_2O_3	Hexagonal	7	LREE
Ce_2O_3	Hexagonal	7	LREE
Pr_2O_3	Hexagonal	7	LREE
Nd_2O_3	Hexagonal	7	LREE
Pm_2O_3	Hexagonal	7	LREE
Sm_2O_3	Cubic	6	HREE
Eu_2O_3	Cubic	6	HREE
Gd_2O_3	Cubic	6	HREE
Tb_2O_3	Cubic	6	HREE
Dy_2O_3	Cubic	6	HREE
Ho_2O_3	Cubic	6	HREE
Er_2O_3	Cubic	6	HREE
Tm_2O_3	Cubic	6	HREE
Yb_2O_3	Cubic	6	HREE
Lu_2O_3	Cubic	6	HREE

2.2.2. Rare Earth Carbonates (RECs)

The crystal structure of lanthanum carbonate octahydrate $[La_2(CO_3)_3.8H_2O]$ has been

studied and established to be orthorhombic by (Shinn and Eick, 1968). (Caro, et al., 1972)

studied the infrared spectra of all rare earth carbonates and established that, at CO_2 partial

pressure less than 1 atm, La, Ce, Pr and Nd form carbonates with 8 waters of hydrations as well.

The IR spectra indicate features attributed to the two types of carbonate sites, one monodentate,

the other bidentate, just like (Shinn and Eick, 1968) proposed in their paper, making Caro et.al, (1972) conclude that, from La to Nd, the octahydrates all have an orthorhombic crystal structure. Shinn and Eick (1968) had established a 10 coordination number for lanthanum carbonate. It is therefore safe to assume that La to Nd also have a 10 coordination number. (Caro et al., 1972) report orthorhombic crystal structures for Sm through Lu, as well, the difference being only in the waters of hydration. From Sm to Tm, there are 2 to 3 waters of hydration, and Yb and Lu are hexahydrate. Because they have the same crystal structure as well as the same trivalent change, it is hypothesized that they all have a coordination number of 10. Pm is radioactive and has no stable isotopes. So, there is no information about it. It can however be assumed that it has a C.N. of 10, since all RECs have a 10 C.N.

Table V: RECs Coordination Number by Crystal Structure

RECs	Crystal Structure	Waters of Hydration	Coordination Number	Designation
$La_2(CO_3)_3$	Orthogonal	8	10	LREE
$Ce_2(CO_3)_3$	Orthogonal	8	10	LREE
$Pr_2(CO_3)_3$	Orthogonal	8	10	LREE
$Nd_2(CO_3)_3$	Orthogonal	8	10	LREE
$Pm_2(CO_3)_3$	Orthogonal	----	10	LREE
$Sm_2(CO_3)_3$	Orthogonal	2 to 3	10	MREE
$Eu_2(CO_3)_3$	Orthogonal	2 to 3	10	MREE
$Gd_2(CO_3)_3$	Orthogonal	2 to 3	10	MREE
$Tb_2(CO_3)_3$	Orthogonal	2 to 3	10	MREE
$Dy_2(CO_3)_3$	Orthogonal	2 to 3	10	MREE
$Ho_2(CO_3)_3$	Orthogonal	2 to 3	10	HREE
$Er_2(CO_3)_3$	Orthogonal	2 to 3	10	HREE
$Tm_2(CO_3)_3$	Orthogonal	2 to 3	10	HREE
$Yb_2(CO_3)_3$	Orthogonal	2 to 3	10	HREE
$Lu_2(CO_3)_3$	Orthogonal	2 to 3	10	HREE

Crystal structure, which was the basis of distinction for LREOs, MREOs and HREOs, cannot be used here, since all RECs are orthogonal. However, based on atomic number, the fifteen RECs can be subdivided into five LRECs, five MRECs and five HRECs, just as shown on Table V.

2.2.3.   Rare Earth Phosphates (REPs)

REPs occur predominantly as phases in monazite and xenotime ores with monazite incorporating mostly LREEs (La-Gd); whereas HREEs are mostly found in xenotime (Tb-Lu as well as Sc and Y). Monazite is monoclinic, and xenotime is tetragonal. Both ores exist in a continuum of REE consistencies. Yunxiang et al., (1995) argue that monazite is monoclinic. According to Huang, (2010) rare earth phosphates exhibit a coordination of 9 from La to Gd, and 8 from Tb to Lu. Since the first half of REPs are monoclinic and the second half is tetragonal, REPs are only classified as light REPs (LREPs) and heavy REPs (HREPs). See Table VI.

Table VI: REPs Coordination Number by Crystal Structure

REPs	crystal structure	coordination number	Designation
$LaPO_4$	Monoclinic	9	LREE
$CePO_4$	Monoclinic	9	LREE
$PrPO_4$	Monoclinic	9	LREE
$NdPO_4$	Monoclinic	9	LREE
$PmPO_4$	Monoclinic	9	LREE
$SmPO_4$	Monoclinic	9	LREE
$EuPO_4$	Monoclinic	9	LREE
$GdPO_4$	Monoclinic	9	LREE
$TbPO_4$	Tetragonal	8	HREE
$DyPO_4$	Tetragonal	8	HREE
$HoPO_4$	Tetragonal	8	HREE
$ErPO_4$	Tetragonal	8	HREE
$TmPO_4$	Tetragonal	8	HREE
$YbPO_4$	Tetragonal	8	HREE
$LuPO_4$	Tetragonal	8	HREE

3. Experimental

3.1.   XRPD and LRS Studies

3.1.1.   Background to the Study

Different mechanisms exist for the adsorption of organic substances on surfaces of minerals, including REOs: chemisorption, Physisorption, surface precipitation and colloid adsorption. Chemisorption involves chemical bonds breaking and forming, large bond energies (>60kJ/mol), high activation energies, and sufficient free energies (<-20kJ/mol). It creates a surface with a monolayer or less, and causes transformation into a new material. In physisorption, the molecule usually physically attaches to the surface via an opposite charge. It does not involve bond breaking and formation, therefore no activation energy. The surface does not transform, albeit no more than a monolayer can form. Likewise, surface precipitation surface precipitation can occur as multilayers depending on mineral and collector solubilities. It typically depends on the collector being transported to the mineral surface by stirring but reacting with metal diffusing from the surface. Because the latter is considered the slow step, the process occurs at the interface and is therefore referred to as surface precipitation. The formation of surface precipitates is limited to the amount of physisorption or chemisorption that might precede it due to passivation. The type of bond ultimately formed depends on the conditions of the experiments. Finally, colloid adsorption occurs when collector molecules form colloids in solution which are often at high ionic strength. The collector forms stable colloidal phases that adsorb at the mineral surfaces in a process similar to physisorption. The conditions for colloidal adsorption do not occur in REM/SHA systems, and are consequently ignored herein. In this regard, Figure 2 depicts the various adsorption mechanisms except colloid adsorption.
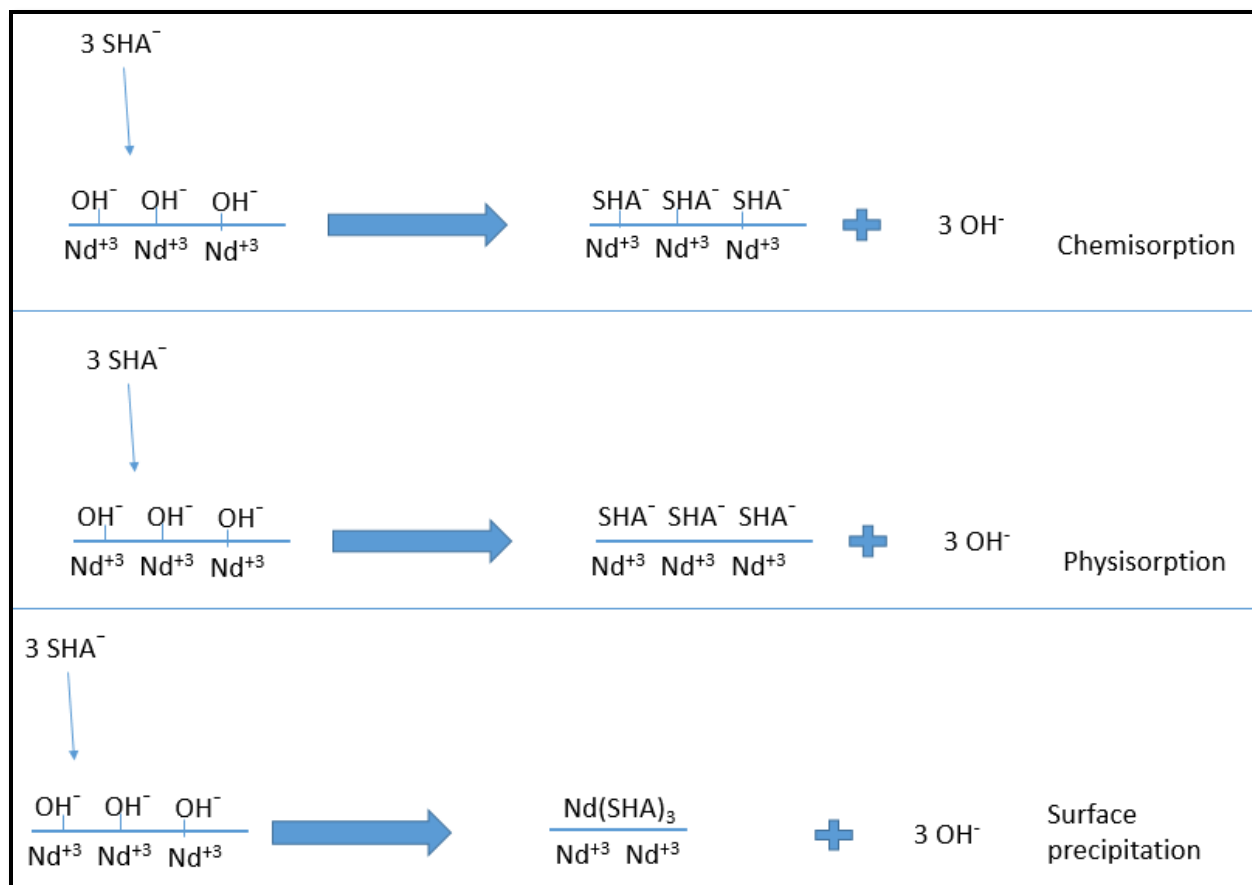
Figure 2: Illustrative drawing of chemisorption, physisorption and surface precipitation of SHA⁻ at the surface of Nd₂O₃.

In an effort to determine the mechanism of SHA adsorption on the surfaces of a suite of REOs, namely La_2O_3, Nd_2O_3, Gd_2O_3 and Dy_2O_3, increasing SHA concentrations at pH 9.5 were added to solutions of the REEs dissolved in dilute HCl. The high pH of SHA concentrations would induce REO precipitation of high surface area and allow for adsorption to be more easily observed and characterized. The adsorbed surfaces were characterized using XRPD and LRS. Although the conditions, as used here, favor surface precipitation of SHA on REOs, their characterizations by these techniques may allow other observations. The study was first performed on Nd_2O_3, and then reproduced on La_2O_3, Gd_2O_3 and Dy_2O_3.

3.1.2. La-SHA Surface Precipitation Studies

3.1.2.1. Surface Precipitates Synthesis

To five beakers containing each 0.2g of La_2O_3, a small amount of dilute HCl was added. To four other beakers containing 0.056g, 0.186g, 0.282g, 0.564g of SHA, a dilute solution of sodium hydroxide was added such that a pH 9.5 was attained. To the fifth beaker, similar to the ones containing SHA solution, a small amount of dilute NaOH solution at pH 9.5 was added. The five beakers containing each La solutions were slowly added to the other five beakers, maintaining a pH of 9.5 using concentrated NaOH solution as pH modifier. The fifth beaker containing only sodium hydroxide solution was used as background for comparison purposes. As La solution was added and the pH kept at 9.5, precipitates formed in each beaker. The precipitates were filtered, washed and left to dry in air.

3.1.2.2. La-SHA Bulk Precipitate Synthesis

For comparison purposes, a bulk precipitate of SHA and La^{3+} was also prepared using a method reported by Feng and Fernando, (1962) for preparing 4-hydroxybenzothiazoline with REEs. A Lanthanum nitrate solution was made by dissolving 0.2g Nd_2O_3 in 30mL of 70% HNO_3 and gently heated. A mixture of 10mL ethanol and 10mL distilled water was prepared, 2.18g SHA was dissolved in it, and the resulting solution was added to the neodymium nitrate solution. To aid the dissolution, the pH was brought to 10.6. With a ratio SHA:Nd_2O_3 of 6:1, the SHA solution was slowly added to the neodymium nitrate solution. Stirring was needed to redissolve any precipitates that temporarily formed. It was also noted that the reaction was exothermic, with a liberation of fumes. With stirring continued, 25% ammonium hydroxide was then added dropwise until a permanent bulk precipitate of $Nd(SHA)_3$ was formed. After the precipitation

was completed, 3 to 4 more drops were added to make sure all of the hydroxamate precipitated out.

3.1.3. Nd, Gd and Dy SHA Precipitation Studies

3.1.3.1.   Nd-SHA Surface Precipitates Syntheses

The procedures used in Section 3.1.2.1 for La_2O_3 are repeated using Nd_2O_3.

3.1.3.2.   Nd-SHA Bulk Precipitate Synthesis

The procedures used in Section 3.1.2.2 for La_2O_3 are repeated using Nd_2O_3.

3.1.3.3.   Gd-SHA Surface Precipitate Syntheses

The procedures used in Section 3.1.2.1 for La_2O_3 are repeated using Nd_2O_3.

3.1.3.4.   Gd-SHA Bulk Precipitate Synthesis

The procedures used in Section 3.1.2.2 for La_2O_3 are repeated using Gd_2O_3.

3.1.3.5.   Dy-SHA Surface Precipitate Syntheses

The procedures used in Section 3.1.2.1 for La_2O_3 are repeated using Nd_2O_3.

3.1.3.6.   Dy-SHA Bulk Precipitate Synthesis

The procedures used in Section 3.1.2.2 for La_2O_3 are repeated using Dy_2O_3.

3.2.   Gibbs Free Energy of SHA Protonation

3.2.1.   Background

The Gibbs free energy of protonation of SHA needed to be determined. It is necessary for more accurate thermodynamic calculations. It will indicate regions where salicylic hydroxamate ion would get protonated and would be less likely to adsorb at REM surfaces. To determine it, a titration of a basic solution of SHA against a solution of acid was performed. It follows Equation 1.

$$C_7H_6NO_2{}^- + H^+ \Leftrightarrow C_7H_5NO_2H$$
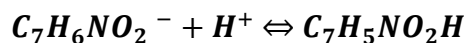
Equation 1

The aim is to obtain its pK_a from the titration curve, and ultimately its K_a value from Gibbs free

energy equation at equilibrium:

$$\Delta G = -nRTlnK_a$$

Equation 2

The Gibbs free energy of the SHA protonation reaction can then be determined allowing for

Gibbs free energy of both SHA species to be calculated. These values are needed to determine

appropriate StabCal speciation diagrams.

3.2.2.   Reagents, Set up and Procedure

A dilute hydrochloric acid solution was prepared by taking approximately 1.3mL of 6N

standardized HCl solution obtained from Alfa Aesar and diluting it to 250 mL in a volumetric

flask. The solution was then standardized against a $4.49x10^{-3}$M $CaCO_3$, and the concentration

determined to be $5.18 \ x10^{-2}$M.

To prepare the SHA solution, precautions had to be taken to avoid any significant amount

of dissolved atmospheric carbon dioxide. Dissolved carbon dioxide forms carbonic acid and, at

high pH (>12), carbonate ion would be the predominant form, such that titrating with an acid,

will cause $HCO_3{}^-$ and H_2CO_3 before dissociating back into H_2O and CO_2 at low pH. This will

interfere with SHA titration and even precipitate out dissolved REEs as RECs. So, water was

basified to pH 13.5, then boiled for a few minutes to remove any dissolved CO_2. The solution

was then cooled down under vacuum to close to or at room temperature. It was then put in a

conical flask and capped to allow it to cool down to room temperature. SHA weighing 0.2049g

was then put into clean 250 mL volumetric flask, and the CO_2 free water was added to the mark

to get a concentration of $5.35x10^{-3}$ M.

To determine whether there was any carbonate ions left in solution, a sample of CO_2 free water was titrated against HCl. For comparison purposes, a basified, not boiled solution was titrated against HCl as well. Likewise, the SHA solution was then titrated with hydrochloric acid. To do the titration, small increments of HCl solution were added and pH was simultaneously measured as illustrated in Figure 3.

0.052M HCl

5.35×10^{-3}M SHA⁻ solution
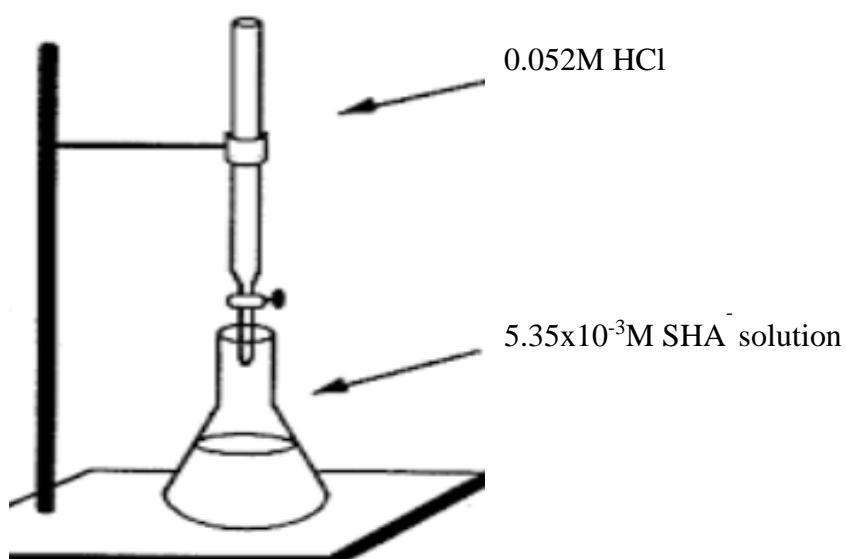
Figure 3: Schematic diagram of the titration of salicyl hydroxamate with HCl

4. Results and Discussions

4.1. Nd$_2$O$_3$

As stated in the experimental procedures, tests were carried on Nd$_2$O$_3$ first, and then repeated for La$_2$O$_3$, Gd$_2$O$_3$ and Dy$_2$O$_3$. Resulting precipitates were washed and dried in air and analyzed using XRPD and LRS techniques described earlier.

4.1.1. X-Ray Powder Diffraction

The precipitates were finely ground using a mortar and pestle, loaded on grooved glass slides, and mounted in sample chamber of Rigaku Ultima IV X-Ray Diffractometer. Cu-K$_\alpha$ radiation at 40 kV and 40 mA generated the diffraction patterns on a D/teX 1D silicon strip detector. Resulting patterns were analyzed with the PDXL software under the standard measurement mode.

Figure 4 shows the XRPD patterns of SHA, the bulk precipitate and Nd$_2$O$_3$. It can be seen that all three species are crystalline, and that they have different and clear diffraction patterns. Because there is a lack of broadening in the diffraction patterns, there are no amorphous phases. The difference between the bulk precipitate and its starting reagents show that the bulk precipitate is distinctly different and therefore is not just a mixture of SHA and Nd$_2$O$_3$. Figure 5 shows the XRPD diffractograms of the different SHA concentrations. Data analysis using the XRPD database known as International Center for Diffraction Data (ICDD) shows that the constituents of the precipitates are a mixture of Nd^{+3} bonded to all the anions present in
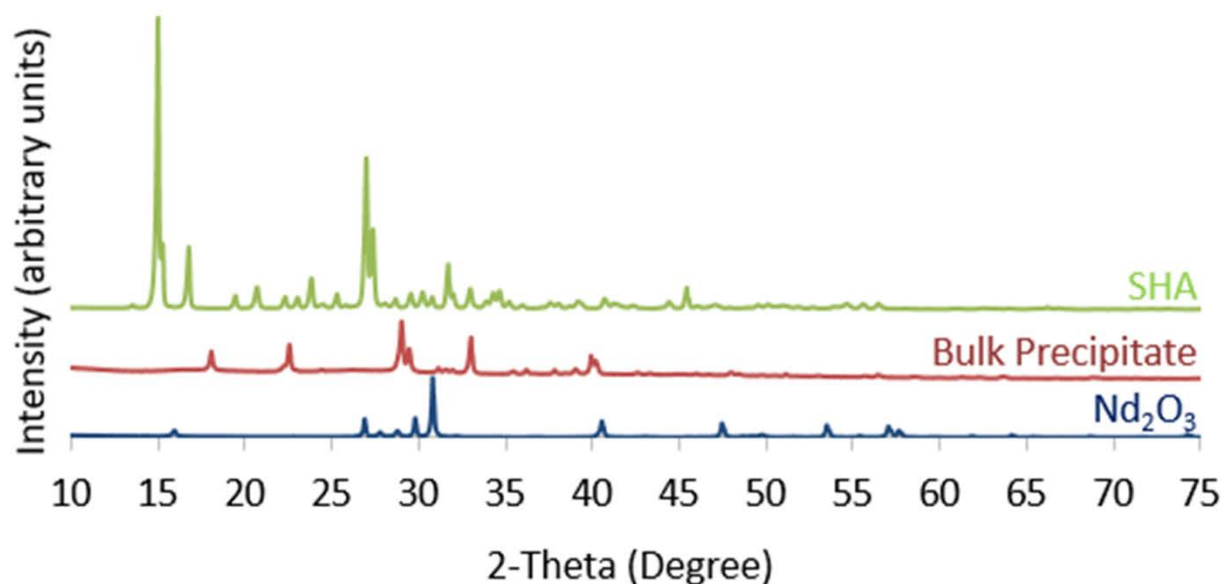
Figure 4: SHA, Nd₂O₃, and bulk precipitate XRPD patterns

solution as well as their hydrates: $Nd(OH)_3$, $Nd(OH)_3 \cdot xH_2O$, $NdCl_3$, $NdCl_3 \cdot xH_2O$, $Nd(OH)_2Cl$,

$Nd(OH)_2Cl \cdot xH_2O$, $Nd_2(CO_3)_3$ and $Nd_2(CO_3)_3 \cdot xH_2O$. $Nd(OH)_3$ and its hydrates constitute the

bigger portion, on the order of 95%. The predominance of $Nd(OH)_3$ and hydrates is explained by

its relatively low solubility at a pH range of 9 to 10. It can be observed that all of the peaks in the

background matrix match those obtained at different SHA concentrations. It is also noted that

peak intensities decrease from $5x10^{-4}$ M (low SHA concentration) to $5x10^{-1}$ M SHA (high SHA

concentration), almost to disappearance. A brief comparison between the Figure 5 patterns and

SHA pattern shows no peak match, indicating that the precipitates are distinct from their starting

reagents as well. A look at the LRS was therefore used to reveal the full story.
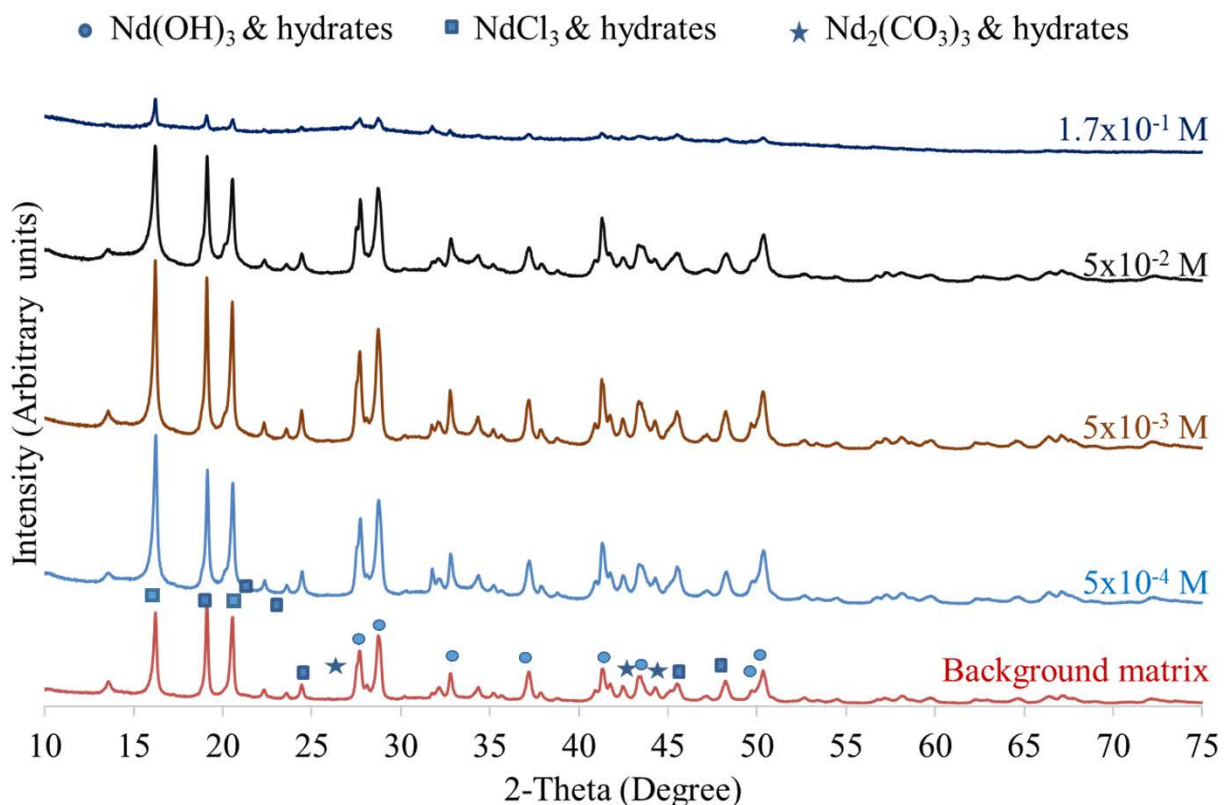
Figure 5 Nd-SHA precipitates and background matrix XRD patterns.

4.1.2. Laser Raman Spectroscopy (LRS)

Figure 6 is the LRS spectrum of SHA and its identified peaks. Figure 7 shows the LRS spectra of the Nd precipitates made at different SHA concentrations and compared to the bulk precipitate of $Nd(SHA)_3$. The spectrum titled 0.0M SHA is that of the background matrix, and, as such, is expected to be in all spectra until SHA concentrations become high enough to affect it. Consequently, the spectra obtained for low concentrations are similar. At higher SHA concentrations, particularly the highest at 1.7×10^{-1} M, the spectra become similar to the bulk precipitate. Thus, comparing Figure 5 and Figure 7 it can be seen that, as the concentration of SHA increases, an amorphous $Nd(SHA)_3$ precipitate gradually increases in amount, while the

background Nd(OH)₃ matrix decreases. This suggests that there is an ion exchange between the

background matrix anions and SHA⁻ anions in solution:

$$Nd(OH)_3 + 3SHA^- \Leftrightarrow Nd(SHA)_3 + 3OH^-$$

Equation 3

This further suggests that SHA surface precipitates on Nd₂O₃ and is likely to occur for other

REOs too.
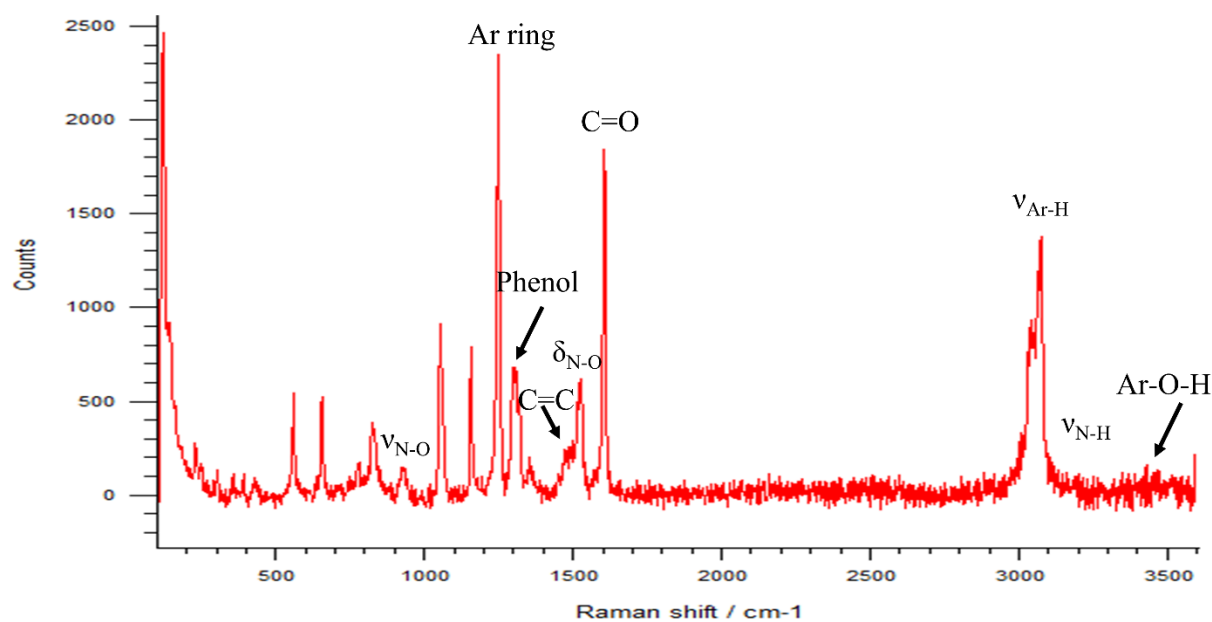
Figure 6: SHA LRS spectrum and identified peaks.
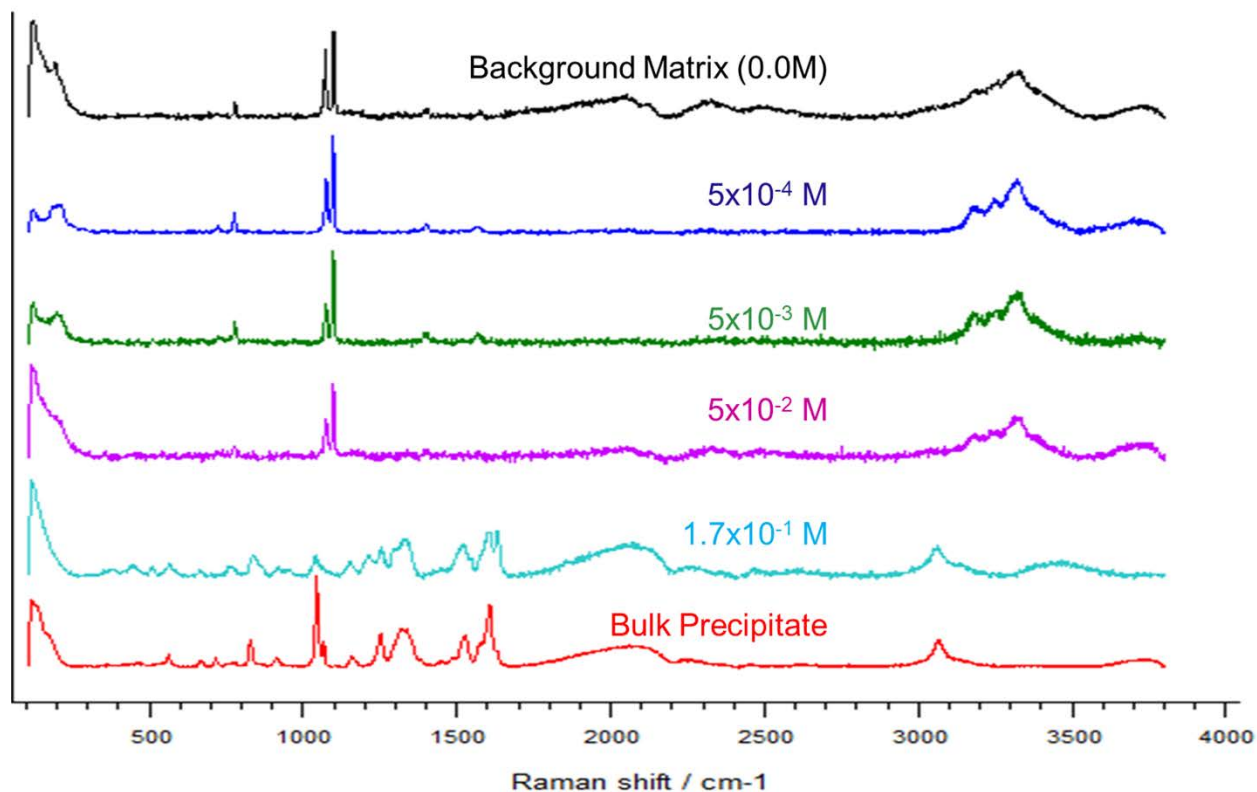
Figure 7: LRS spectra comparison of bulk precipitate to Nd-SHA precipitates at different SHA concentrations

Further analysis of the LRS at various concentrations of SHA along with that of the bulk precipitate of Nd(SHA)$_3$ reveal other patterns. First, the twin peaks around 1080 cm^{-1} are characteristic of the O-H bending vibrations from Nd(OH)$_3$ which decrease in intensity with increasing SHA concentration and disappear at very high (1.7×10^{-1} M) SHA concentration. Second, the broad characteristic O-H stretching band centered near 3300 cm^{-1} also decreases in intensity with increasing SHA concentration and disappears at the high SHA concentration of 1.7×10^{-1} M. Likewise, other bands simultaneously appear, namely CH-stretching vibrations 3050 cm^{-1} as well as NH, N-OH and Ar-OH stretching vibrations between 1000-1600 cm^{-1}. These patterns clearly indicate that OH$^-$ is being displaced from the surface by SHA$^-$ but is not always due to surface precipitation and would be attributed to an ion exchange chemisorption process:

$$Nd\text{-}OH_{ads} + SHA^- \Leftrightarrow Nd\text{-}SHA_{ads} + OH^-$$
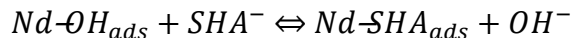
<div align="right">**Equation 4**</div>

where SHA$_{ads}$ is chemisorbed SHA. In measuring the thermodynamics of the chemisorption, Galt (2017) determined free energy values to be between -5 and -10 kcal/mol, which is neither indicative of chemisorption nor physisorption. However, because an ion exchange mechanism is involved, it is likely chemisorption.

In this regard, it is noted that this is further corroborated by the C=O band at 1610 cm^{-1} becoming a doublet at approximately 1600 and 1650 cm^{-1} for the spectrum obtained at the high SHA concentration of 1.7×10^{-1} M. This is attributed to bonding between SHA with H$^+$ (in the singlet at 1610 cm^{-1}) and Nd^{3+} (in the doublet at 1650 cm^{-1} and 1600cm^{-1}) and the latter is likely attributed to both resonance and chelation. The same thing is observed with the bulk precipitate when compared to pure SHA, where a doublet near 1040 and 1070 cm^{-1} is preceded by the C-N stretch at 1060 cm^{-1}. This too is likely due to resonance and chelation bonding. It can therefore be concluded that SHA does not physisorb on Nd$_2$O$_3$, but likely chemisorbs as well as surface precipitates.

Overall, the adsorption of SHA occurs through a displacement of hydroxide at the surface by ion exchange. This displacement results in a chelation bond generally prevalent among hydroxamates; however, at low SHA concentrations, the ion exchange and chelation forms up to a monolayer of chemisorbed SHA and, at high SHA concentrations, it leads to the precipitation of Nd(SHA)$_3$.

4.2. Comparisons to La, Gd and Dy

The patterns observed for Nd in the previous section are the same observed in La, Dy and Gd, within a few subtle differences attributed to lanthanide contraction and therefore differences in ionic size of the REEs.

4.2.1. Comparison to La

XRPD and LRS results for La are shown in Figure 7 and Figure 8, respectively. A comparison to Figure 5 and Figure 7 for Nd allows for the following to be noted:
From Figure 7 a number of trends can be observed a number of trends common to Nd-SHA are observed:

i. Although the starting material is La_2O_3/$La(OH)_3$, the XRPD patterns and LRS spectra of the precipitates are virtually the same;

ii. XRPD patterns indicate that La is predominantly present as $La(OH)_3$ and $La(OH)_3.xH_2O$ precipitates;

iii. XRPD peak intensities of these precipitates decrease with increasing SHA concentration;

iv. Some XRPD peaks appear but at lower SHA concentrations compared to Nd suggesting that La $(SHA)_3$ surface precipitates more strongly on La and therefore may be too weak and likely masked by the large amount of surface precipitation;

v. LRS spectra exhibit all the background matrix bands, and gradually modify to show more chelation bands; however there is no indication that chemisorption occurs; and
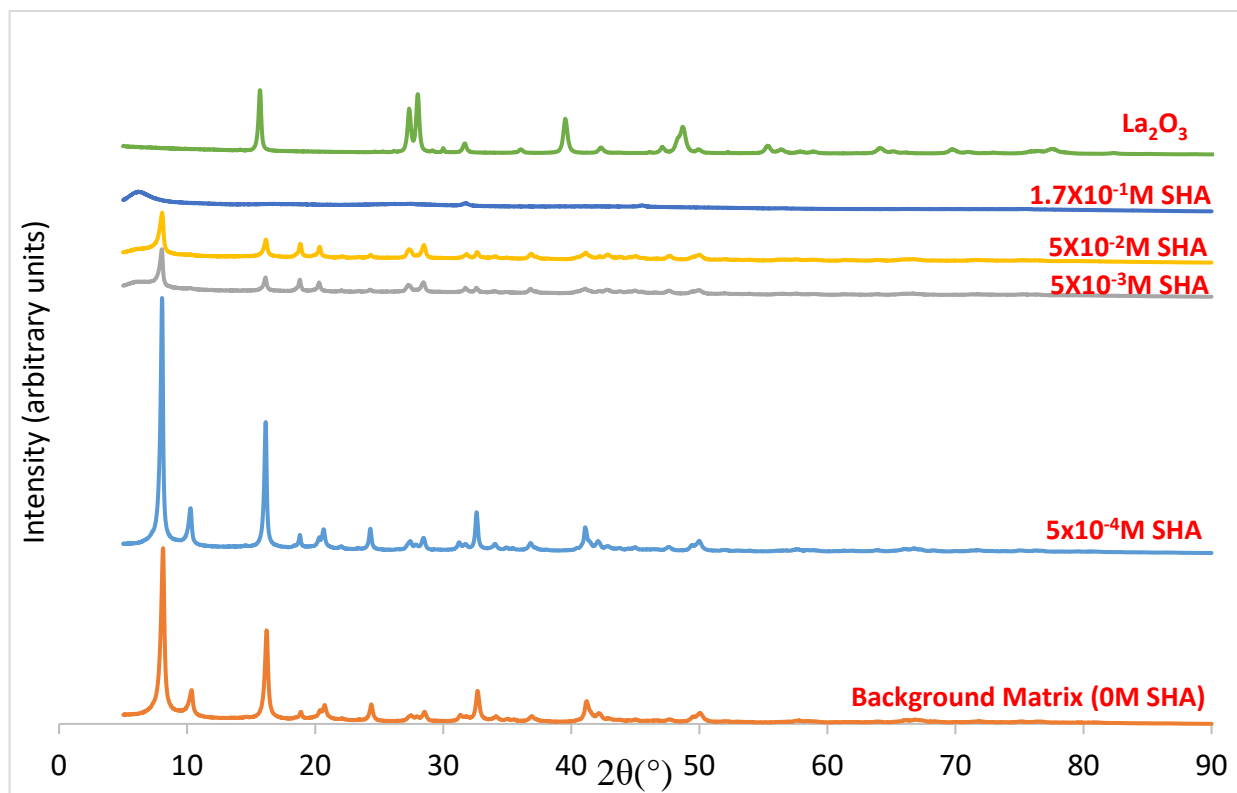
Figure 9: La-SHA precipitates and background matrix XRD patterns.
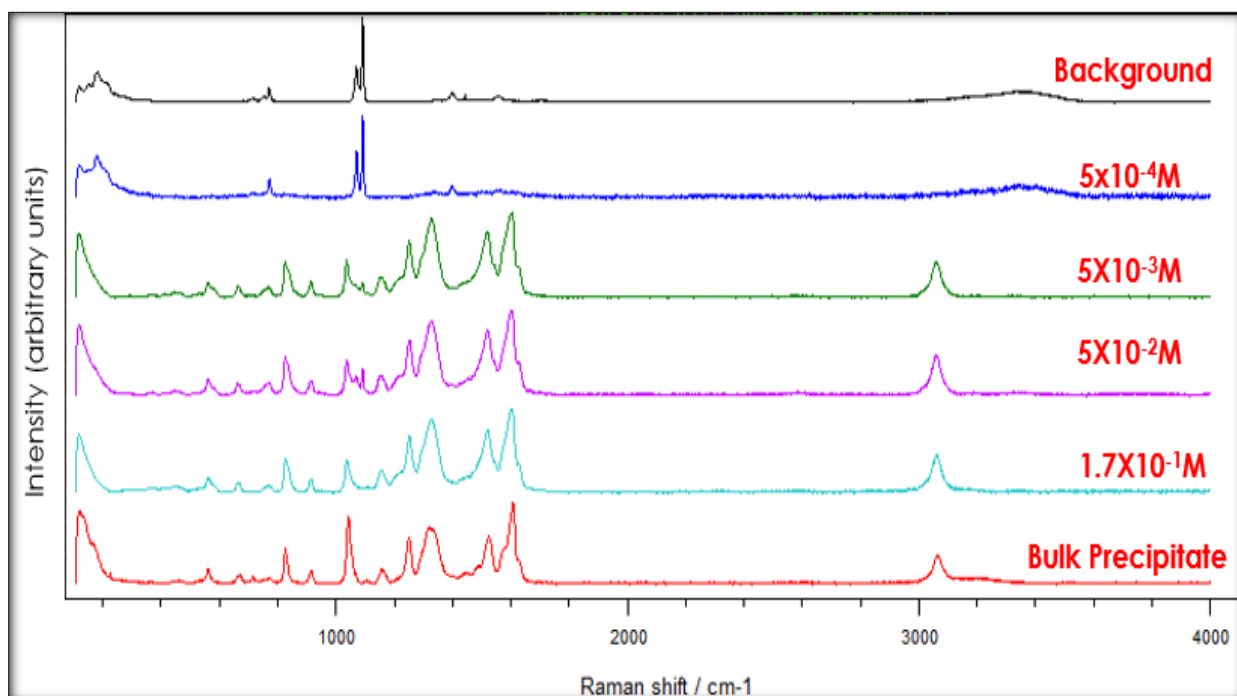
Figure 8: LRS spectra comparison of bulk precipitate to La-SHA precipitates at different SHA concentrations

vi. LRS spectra also show the disappearance of OH vibrations near 1000 and 3400 cm^{-1} and the appearance of various stretching SHA vibrations near 1050cm^{-1} between 1000-1600 cm^{-1} thereby supporting the conclusion that an ion exchange mechanism occurs.

The results to following conclusions:

i. Chelation bonding yields surface precipitation through an ion-exchange process, but at lower SHA concentrations compared to Nd:

$$La(OH)_3 + SHA^- \Leftrightarrow La(SHA)_3 + 3OH^-$$
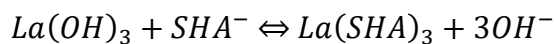
Equation 5

ii. For La, there is no evidence, one way or the other, that chemisorption occurs:

$$La\text{-}OH_{ads} + SHA^- \Leftrightarrow La\text{-}SHA_{ads} + OH^-$$
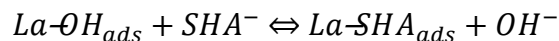
Equation 6

A theoretical study to model adsorption based on lattice and crystal structure properties was therefore undertaken to help explain this results as discussed in Section 6.

It is important to note that Galt(2017) found SHA to adsorb more extensively on La$_2$O$_3$ than Nd$_2$O$_3$ and attributed it to surface precipitation; however, she was also able to determine an adsorption free energy between -5 and -10 kcal/mol presumed to be due to chemisorption. Both mechanisms were attributed to ion exchange.

4.2.2. Comparison to Gd

XRPD and LRS results for Gd are shown in Figure 10 and Figure 11, respectively. A comparison to Nd (Figure 5 and Figure 7) and La (Figure 8 and Figure 9) allows for many of the same observations and conclusions as discussed briefly:

i. Although the starting material here is Gd$_2$O$_3$/Gd(OH)$_3$, the XRPD patterns and LRS spectra of the resulting precipitates are also the same;
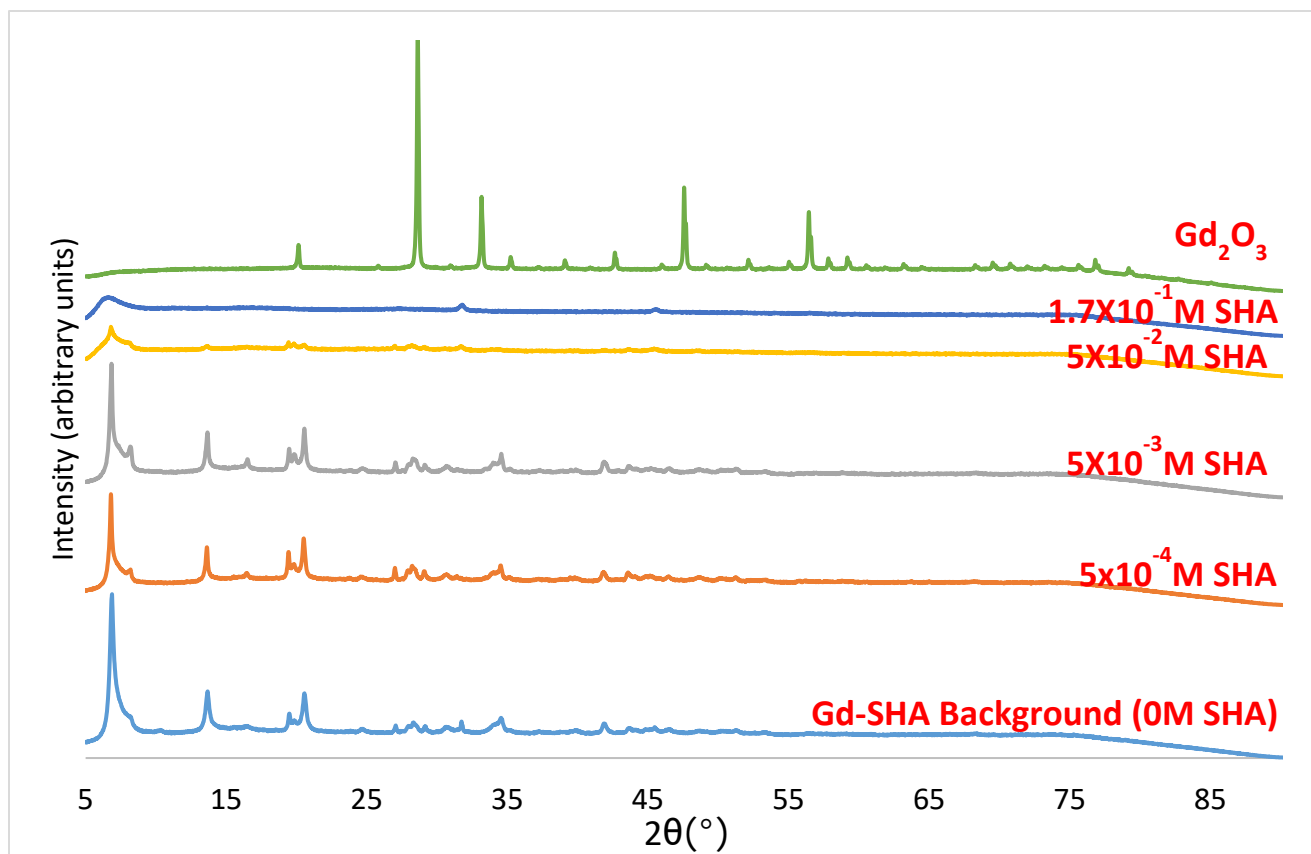
Figure 10: Gd-SHA precipitates and background matrix XRD patterns.
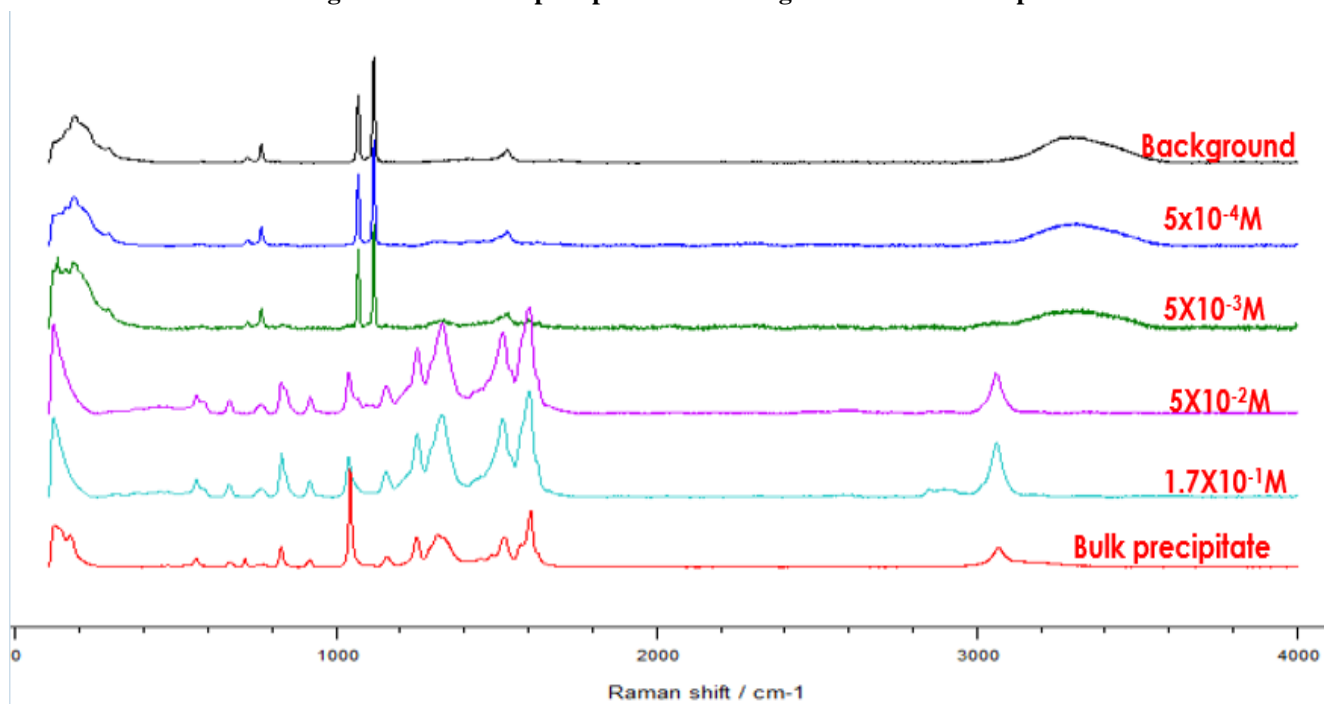
Figure 11: LRS spectra comparison of bulk precipitate to Gd-SHA precipitates at different SHA concentrations

ii.   The results show that the amorphous precipitation of RE(SHA)$_3$ occurs in an approximately constant rate: La ≈ Nd ≈ Gd.

$$Gd(OH)_3 + 3SHA^- \Leftrightarrow Gd(SHA)_3 + 3OH^-$$
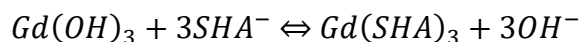
Equation 7

iii.   In this case, LRS spectra appears to suggest that both chemisorption and surface precipitation likely occur, because it is not masked by an abundant amount of surface precipitation:

$$Gd\text{-}OH_{ads} + SHA^- \Leftrightarrow Gd\text{-}SHA_{ads} + OH^-$$
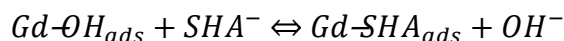
Equation 8

.

These results can indirectly be corroborated by Galt(2017). Although she did not study Gd, she determined that SHA adsorption decreased with increasing atomic number of REOs which concurs with the order just given. Modelling will also complement our understanding.

4.2.3. Comparison to Dy

XRPD and LRS results for Dy are shown in Figure 11 and Figure 12, respectively. A comparison to Nd (Figure 5 and Figure 7), La (Figure 8 and Figure 9) and Gd (Figure 10 and Figure 11) does not change any observations and conclusions as discussed briefly:

i.   In this case, the starting material is $Dy_2O_3/Dy(OH)_3$ and therefore is the REE with the highest atomic number.

ii.   Because the patterns change only in intensity, Dy(SHA)$_3$ does not appear to form in large amounts and therefore mask the pattern; hence the expected trend is observed:

La ≈ Nd ≈ Gd > Dy

$$Dy(OH)_3 + 3SHA^- \Leftrightarrow Dy(SHA)_3 + 3OH^-$$
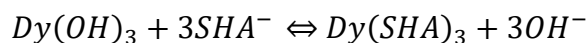
Equation 9

iii. Consequently, the LRS spectra do not appear to change with SHA concentration suggesting only chemisorption is observed and possibly at monolayer coverage independent of SHA concentration:

$$Dy\text{-}OH_{ads} + SHA^- \Leftrightarrow Dy\text{-}SHA_{ads} + OH^-$$
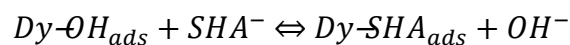
Equation 10
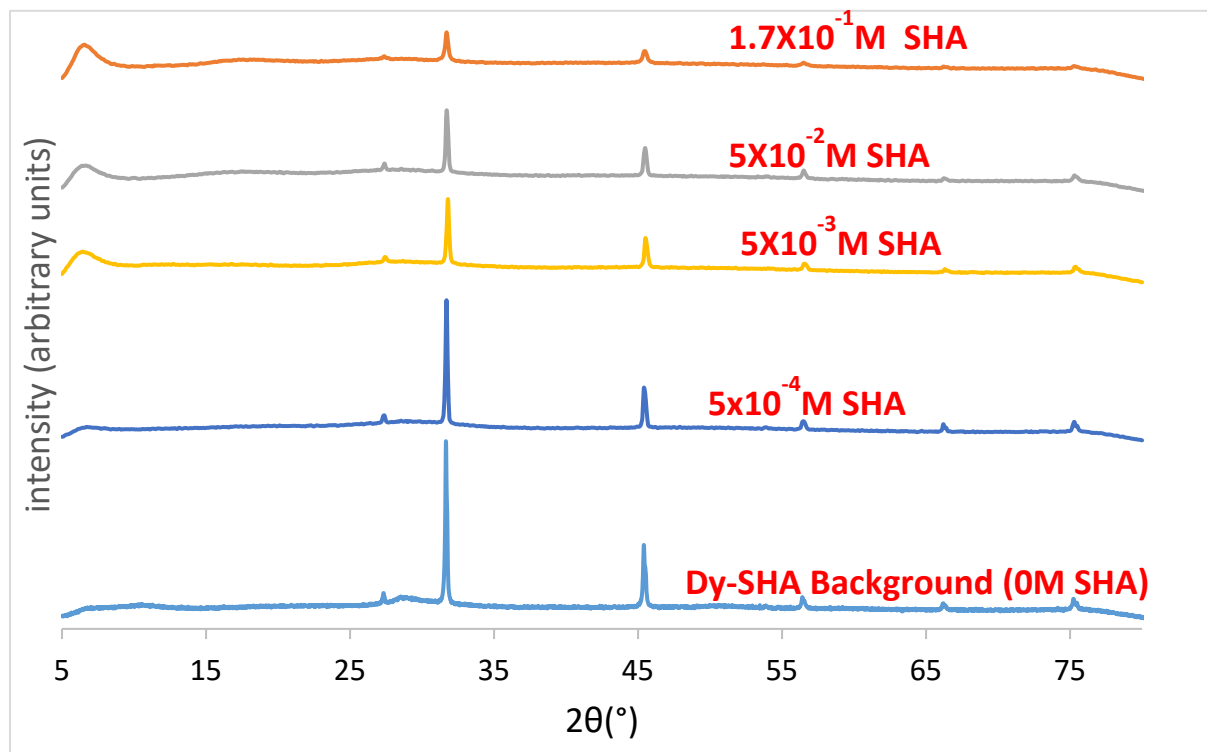
Figure 12: Dy-SHA precipitates and background matrix XRD patterns.

4.3. Conclusions for the Precipitation Studies

The conclusions are the same as those stated in the Nd section, with a touch of generalization. Overall, SHA adsorption occurs through a displacement of hydroxide at the surface in what is clearly an ion exchange mechanism. This mechanism leads to:

i. Surface precipitation which predominates for LREOs following the order La > Nd > Gd > Dy and

ii.   chemisorption, which appears to predominate in reverse order: $Dy > Gd > Nd > La$.

In essence, this order follows the atomic number and can be attributed to lanthanide contraction. Because SHA is a hydroxamate, it forms chelation bonds. Furthermore, because SHA has "claw" that is 2.42Å in size, it will favor REEs that are closest to this. For the REOs studied, it is noted that the diameters of La^{+3}, Nd^{+3}, Gd^{+3}, and Dy^{+3} are 2.46Å, 2.36Å, 2.30Å and 2.10Å, respectively. Clearly, surface precipitation favors the LREOs and not the MREOs. In this regard, it is likely these results are also dependent on the coordination number and the anion that the REEs bond to in the REMs and is the topic of the thesis by Trant (2018).

5. Thermodynamic Calculations

5.1. Gibbs Free Energy of SHA⁻ Protonation

5.1.1. Trial and Error Procedure Determination

To obtain the Gibbs free energy of protonation of SHA⁻ necessary for improving StabCal calculations, a simple pH titration needs to be performed. However, in the process, a few things had to be corrected in order to get a reproducible and trustworthy number. For example, Figure 14 shows the titration of SHA with hydrochloric acid with unboiled de-inized (DI) water. Because unboiled DI water has a slight amount of dissolved carbon dioxide its equilibrium with carbonic acid (H_2CO_3), a diprotic acid will interfere with SHA protonation as the pH is decreased from 14 to 1, with HCl titrant. As can be seen on the graph and the four others in Appendix B, the buffer region leading to the final equivalence point is perturbed, thereby yielding an inaccurate measurement of the pK_a value for SHA⁻ protonation.

In this case, two things are worth noting. First, the graph does not contain one vertical step, as would be expected of a single protonation process:

$$SHA^- + H^+ \Leftrightarrow SHAH$$
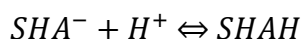
Equation 11

Rather, it appears to contain three, which the other two would be attributed to the carbonic acid:

$$CO_3^{2-} + H^+ \Leftrightarrow HCO_3^-$$

Equation 12

$$HCO_3^- + H^+ \Leftrightarrow H_2CO_3$$
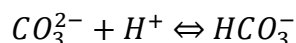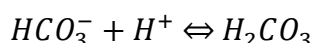
Equation 13

Second, the graph is not smooth and clearly could have other species in solution interfering with the measurement.

As the pH is decreased from near 14 to close to 1, the equilibria characteristic of the successive deprotonations of the diprotic acid will influence the equivalence of protonation of

salycilic hydroxamate ion. As can be seen on the graph below and the four others in Appendix B, the buffer region leading to equivalence point is perturbed.
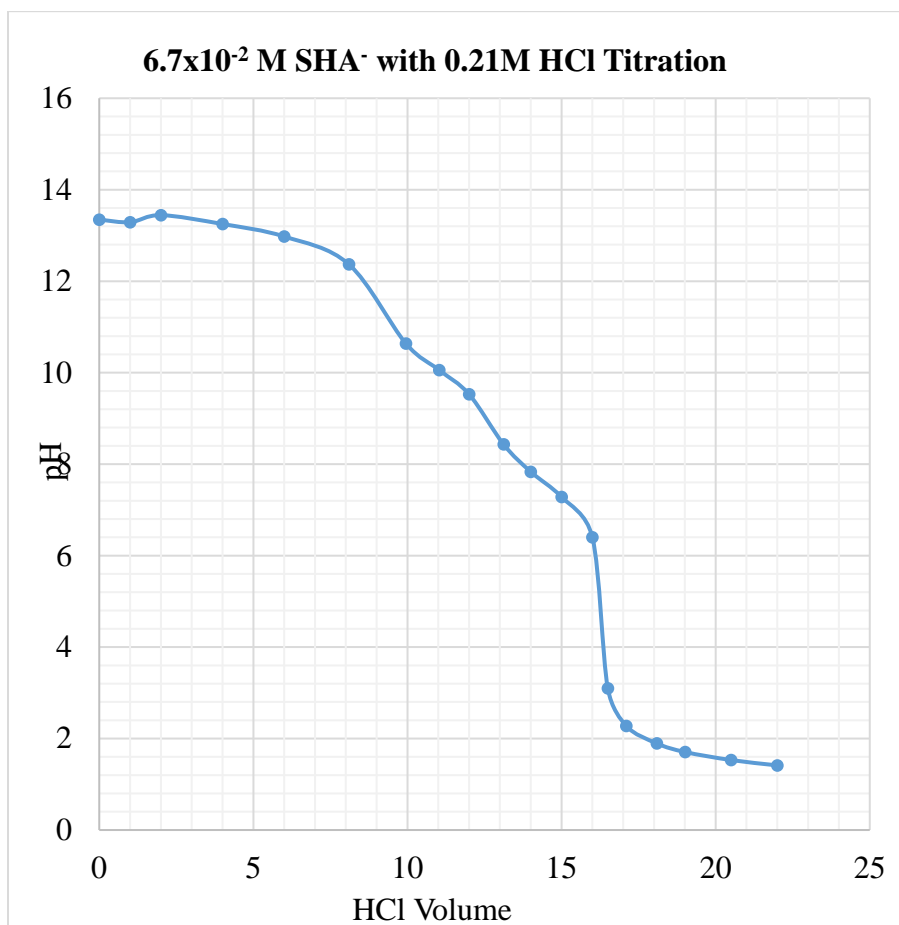
Figure 13: Titration of SHA⁻ solution against HCl prepared with CO₂-containing water

5.1.2. Gibbs Free Energy of Salicylic Hydroxamate Protonation

Figure 15 shows the titration of water in the absence of SHA. In this case, the waster was adjusted to pH 13.5 with NaOH, boiled, and then cooled under a vacuum to prevent CO_2 dissolution. Clearly, there are no perturbations and the graph is very smooth. This same procedure was hence used to make a SHA solution for determining the free energy of SHA protonation.
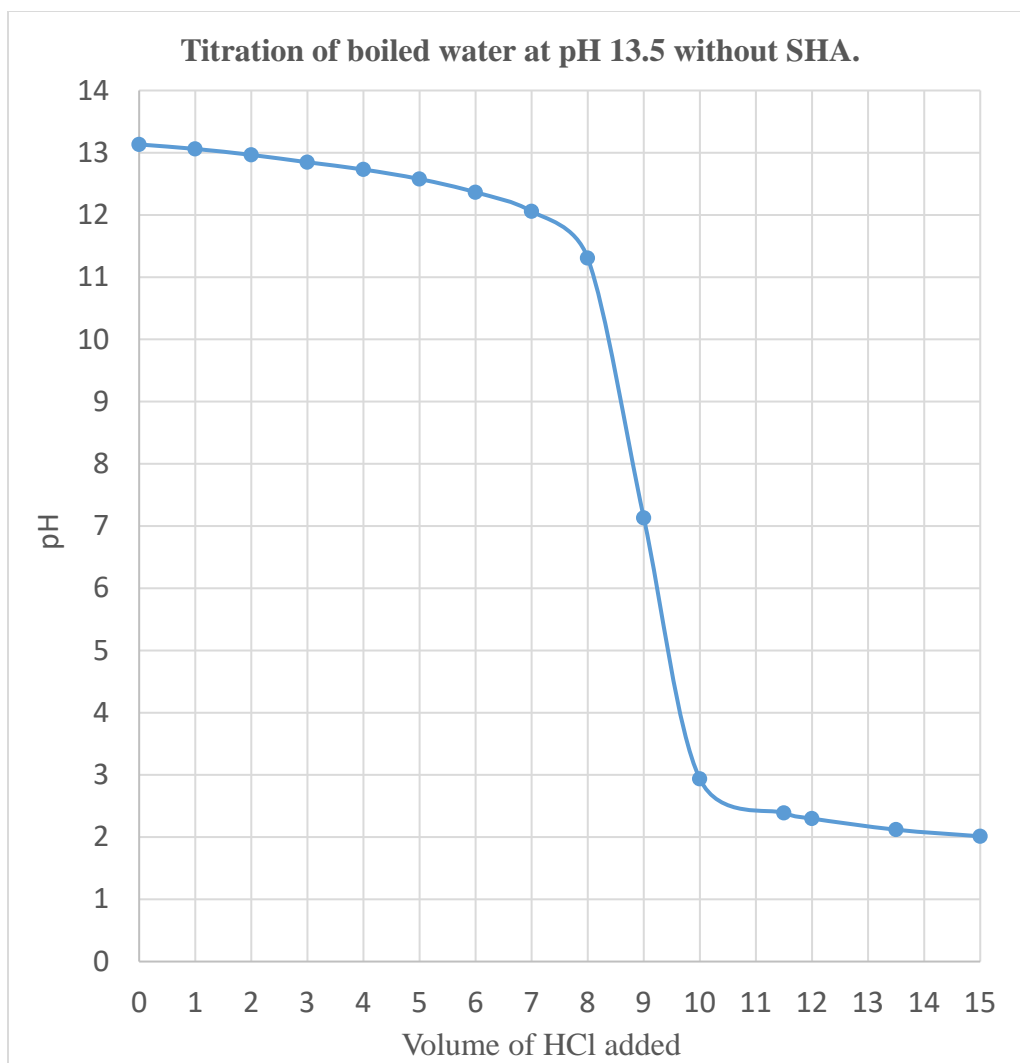
Figure 14: Titration of a solution of NaOH to verify that it is CO₂ free

To analyze the titration curve in Figure 15, it is noted that a strong base (NaOH) is being

titrated against a strong acid (HCl). It can be seen that the equivalence point is exactly at 7,

without any blemish that could be caused by dissolved carbon dioxide (carbonic acid). However,

the pK, which in this case would be that of water (pK_w) appears to be 12.7, which is less than the

14 value expected. This is due to the fact that the highest pH in this experiment is 13.2 (lower

than 14). It is additionally noted that, since HCl had a molarity of 0.0518M, corresponding to a

pH of 1.286, the titration would asymptocally get close to 1.286, and that the adding the

observed 12.7 pKw value to 1.286, one obtains 13.986 which is within within reasonable

agreement to the pKw of water not only gives confidence to using the technique, but also illustrates that the water is free of CO_2. Furthermore, there is 0.04% of CO_2 in atmosphere at sea level. At high altitude like in Butte, it is even less. If the amount that dissolves in water to form the equilibrium is considered, it is negligible. So, boiling water and cooling it under vacuum were good enough precautions to remove all of it.

Figure 16 shows the titration of 5.352×10^{-3} M SHA in CO_2 free water. To analyze, the volume of HCl needed to reach equilibrium is determined and then half of that volume is projected to the pH axis which corresponds to the pK_a value. Once obtained, the pK_a value is used to calculate K_a value and ultimately the Gibbs free energy of SHA protonation. This procedure is illustrated by the ensuing discussion regarding Figure 16.
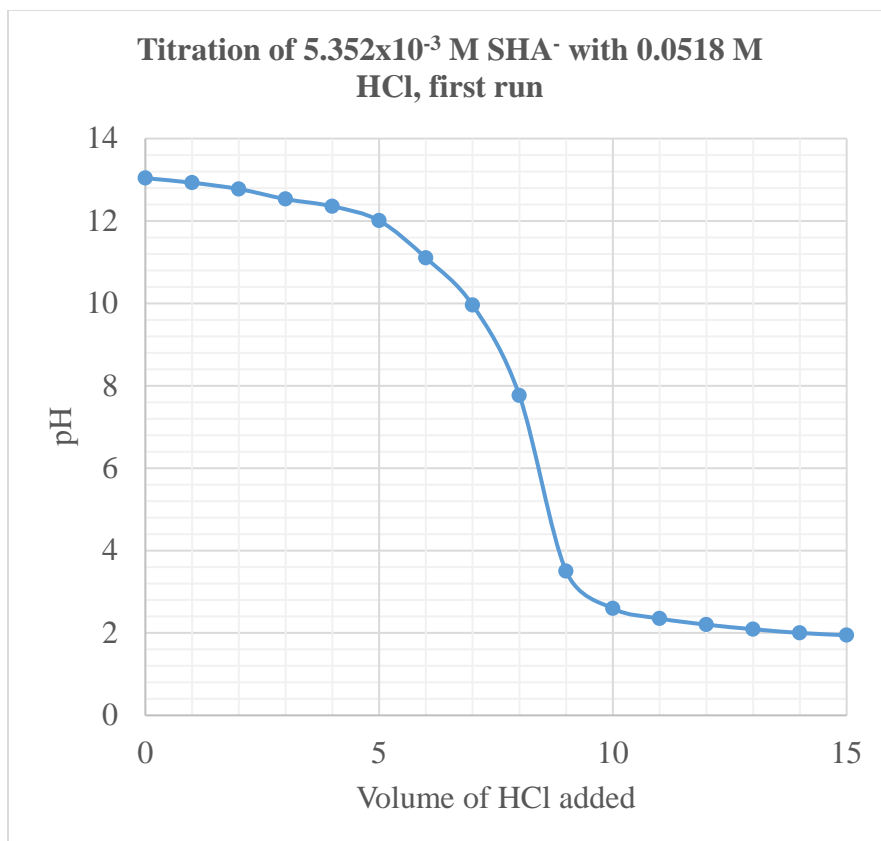
Figure 15: Titration of SHA- against HCl to determine its Gibbs free energy of protonation

First a sharp drop at pH 7.76 when 8mL of HCl is added. At this point, all of the SHA⁻ is converted to SHAH. Thus, at half (i.e., 4mL), half of the initial SHA⁻ was converted to SHAH (i.e., they are in equilibrium). By taking Equation 11, the following is deduced:

$$\frac{1}{K_a} = \frac{[SHAH]}{[SHA^-] \cdot [H^+]}$$

Equation 14

$$[H^+] = [SHAH] \cdot \frac{K_a}{[SHA^-]}$$

Equation 15

But at equilibrium, at the half equivalence point

$$[SHAH] = [SHA^-]$$

Equation 16

Equation 15 becomes

$$[H^+] = K_a$$

Equation 17

$$-\log[H^+] = -logK_a$$

Equation 18

$$pH = pK_a$$

Equation 19

Thus, at half equivalence, the pH equals the pK$_a$. With this, the Gibbs free energy obtained for Equation 11 using ΔG=-RTlnK$_a$. Results of this test (Figure 16) are averaged with the other three shown in Appendix A as seen in Table VII. The Gibbs free energy of the SHA⁻ protonation reaction in Equation 11 was therefore determined to be 16.78 kcal/mol (70.20 kJ/mol).

Table VII: Gibbs Free Energy and pKa Value of Deprotonation of SHAH

	pK$_a$	K$_a$	ΔG(kJ/mol)	ΔG(kcal/mol)
First run	12.40	3.98E-13	70.78	16.92
Second run	12.30	5.01E-13	70.20	16.78
Third run	12.30	5.01E-13	70.20	16.78
fourth run	12.20	6.31E-13	69.63	16.64
Average	**12.30**	**5.08E-13**	**70.20**	**16.78**

Another important aspect revealed by these results is the fact that salicyl hydroxamic acid once in solution, predominantly remains in a protonated form low pH to a pH of 12.3, and will exist in an anionic form above that pH. This has a huge relevance in explaining the results obtained from adsorption experiments and rationalizing the plots obtained using StabCal. It can be considered that below pH 12.3, as seen on Figure 17, predominantly neutral aqueous SHAH species exists; thus its adsorption by ion exchange actually leads to the formation of water:

$$REE\text{–}OH_{ads} + SHAH \Leftrightarrow REE\text{–}SHA_{ads} + H_2O$$
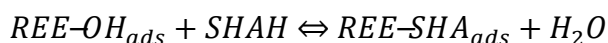
Equation 20

Likewise, the surface precipitation would as well;-

$$REE(OH)_3 + 3SHAH \Leftrightarrow REE(SHA)_3 + 3H_2O$$
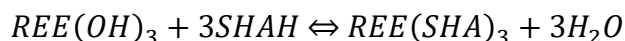
Equation 21

This is because all adsorption tests (Galt, 2017; Trant, 2018), including those herein, were conducted at pH 8-11, well below pH 12.3. Above pH 12.3, adsorption is expected to begin to drop because anionic SHA⁻ will be repelled by the negatively charged REMs.
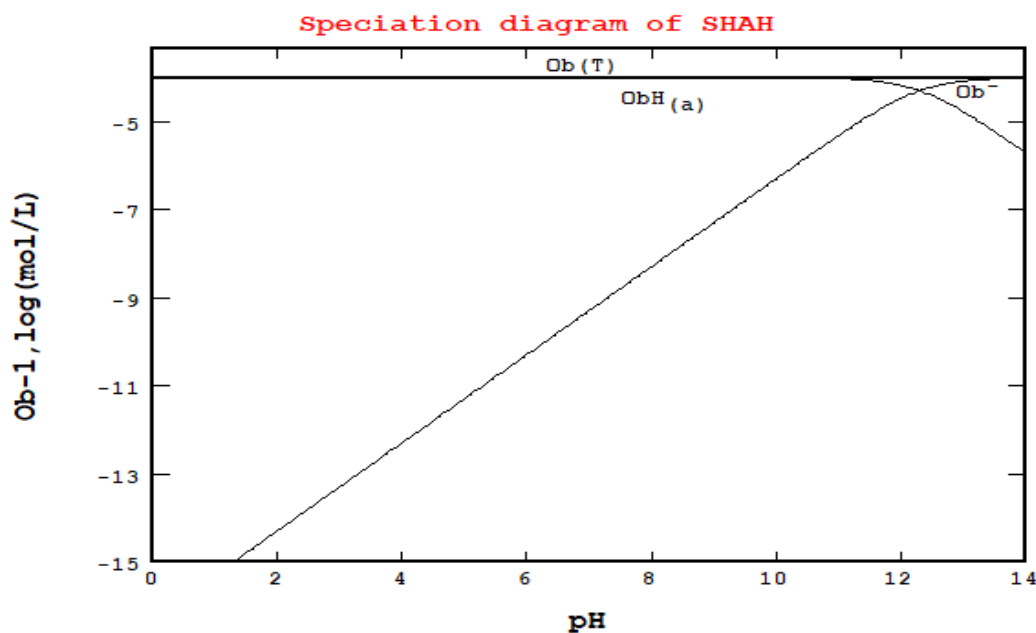
Figure 16: Predominance diagram of SHA.
*ob-1 is the name assigned to SHA⁻ in the STABCAL software, and ObH the name assigned to SHA

With the data obtained, more accurate predominance StabCal diagrams can be calculated. Using

Ce$_2$(CO$_3$)$_3$ as an example, Figure 19 was calculated with thermodynamic data (i.e., including

SHAH). Although differences are subtle, there are differences predominantly observed by the

slight change in Ce$_2$(CO$_3$)$_3$ solubility between 7 and 8. Otherwise, the diagrams are essentially

the same. The important information obtained from this section is the predominance of species

with respect to pH.

Figure 17: Ce$_2$(CO$_3$)$_3$ and SHA system prior to the Gibbs free energy of SHA protonation.

Figure 18: Ce₂(CO₃)₃ and SHA system after the Gibbs free energy of SHA protonation.

6. Theoretical Modeling: Verifications and Confirmation

This section consists of applying the dimensions of collectors "standing" (adsorbing vertically) and "laying" (adsorbing horizontally) on the surface of REO, RECs and REPs. REM structures were obtained from various literature sources. A specific plane in the crystal structure of each was chosen, and theoretical adsorption densities, based on the size of the collector molecule and the separation between atomic sites, were calculated. The objective of the modeling is purely qualitative. If SHA adsorbs on REE site in a given orientation, what is the possibility of another SHA adsorbing on the nearest sites? The site occupied by SHA as well as the sites impeded by the occupation of SHA will constitute the total adsorption area, and theoretical adsorption densities will be calculated based in that area. Illustrations will be made in the following sections.

6.1.1. Langmuir-Blodgett Monolayer Adsorption

If SHA molecules adsorb next to each other, so as to form a mono layer film, maximum adsorption would be similar to a Langmuir-Blodgett (LB) film and essentially be face centered square in its molecular arrangement (see Figure 20). To do this, SHA is assumed to occupy a rectangular form when it lies horizontally with a projected area of 7.53Å by 5.26Å and, when it adsorbs vertically, with a projected area of 5.26 Å by 2.42Å. Figure 21 below illustrates the packing of SHA to form a monolayer. In Figures 19, 20 and 21, the atoms in black are carbons, in red are oxygens, in white are hydrogens, and in blue is nitrogen. The distances indicated in the figure legends are those measured between the atoms highlighted with light yellow circles.
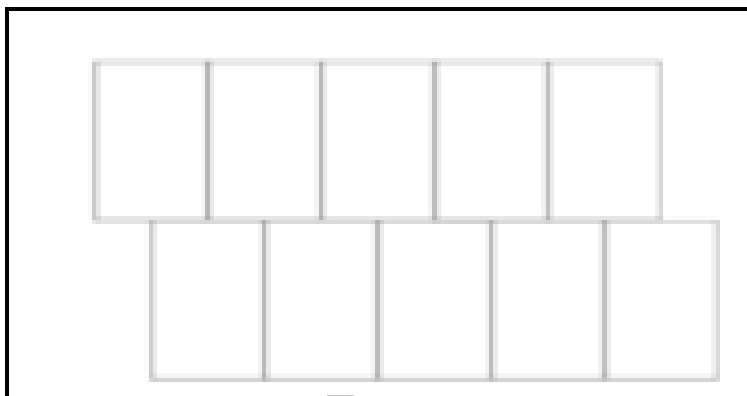
Figure 19: Maximum packing of SHA to form a Langmuir-Blodgett monolayer
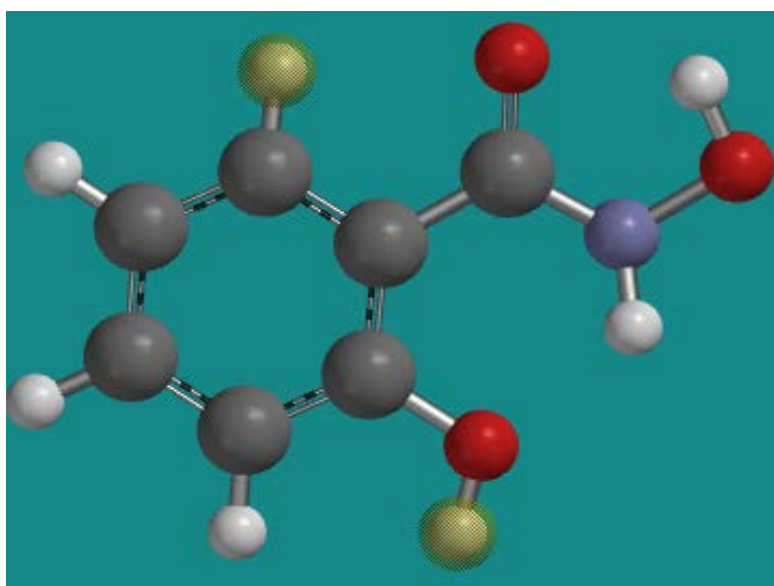
Figure 20: Illustration a short dimension of SHA at 5.26 Å
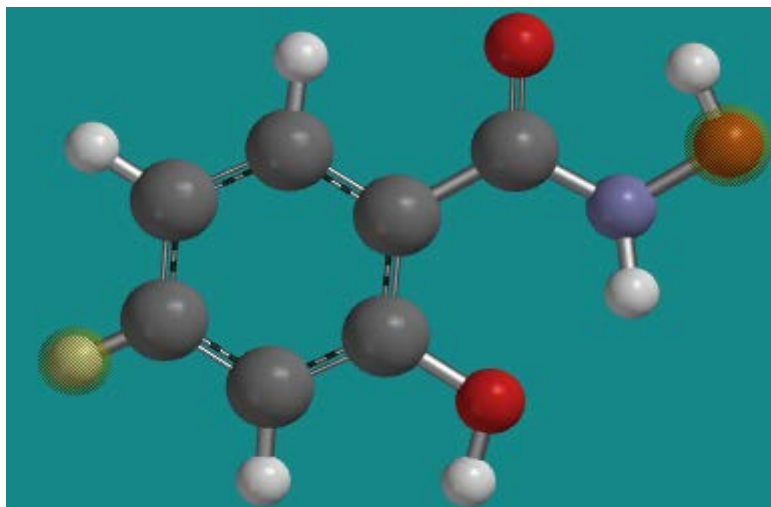
Figure 21: Illustration of the longest dimension of SHA at 7.53 Å
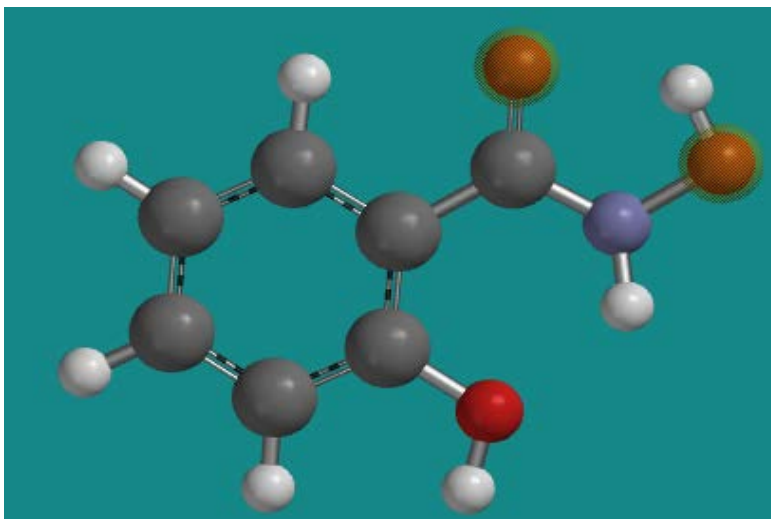
Figure 22: Illustration of the size of the head group of SHA at 2.42 Å

The horizontal adsorption is modeled by considering the distance in Figure 20 as the length (7.53 Å between the yellow highlighted atoms) and the distance in Figure 21 as the width. Similarly, the vertical adsorption uses Figure 21 and Figure 23 as length and width, respectively. In the calculations, the intermediate vertical orientation equivalent to 2.42Å by 7.35Å is ignored. Figure 21, Figure 22 and Figure 23 were drawn using Spartan® software, specifically with Density Functional EDF2 6-31G*.

In the case where SHA forms a monolayer by packing in a horizontal arrangement, the Langmuir-Blodgett monolayer will have a theoretical adsorption density of:

$$\frac{1\ SHA\ molecule \times 10^6 \frac{\mu mol}{mol}}{(7.53 \times 5.26\ Å^2) \times \left(6.02 \times 10^{23} \frac{molecules}{mole}\right) \times (10^{-20} \frac{m^2}{Å^2})} = 4.20\ \mu mol/m^2$$

<div align="right">**Equation 22**</div>

In the case where the monolayer is vertical, Langmuir-Blodgett capacity is

$$\frac{1\ SHA\ molecule \times 10^6 \frac{\mu mol}{mol}}{(5.26 \times 2.42\ Å^2) \times \left(6.02 \times 10^{23} \frac{molecules}{mole}\right) \times (10^{-20} \frac{m^2}{Å^2})} = 13.06\ \mu mol/m^2$$

<div align="right">**Equation 23**</div>

Hence, 13.06 µmol/m² should be the maximum theoretical adsorption density that can be encountered with SHA assuming a monolayer is observed either as physisorption or chemisorption. If adsorption densities higher than that are obtained in experiments, then there is multilayer adsorption, and is likely attributed to surface precipitation.

6.1.2. SHA Modeling

The size of the SHA head group plays a critical role in its adsorption and therefore REM flotation. SHA is a relatively flat molecule with limited flexibility due to the benzyl group (i.e., cyclic vs straight chain organic).

6.1.2.1. SHA-REO Modeling

REOs fall into two different crystal systems. The LREOs (La through Pm) are hexagonal (Zachariasen, 1926). Likewise, the HREOs are cubic (Zachariasen, 1927). See Table VIII. Sc and Y are cubic as well (Zachariasen, 1928). All of the isotopes of Promethium (Pm) are

radioactive and there is no information about its lattice parameters. It is, however, safe to assume that it is hexagonal like the LREOs. To obtain the ionic diameters of REE ions, a table from Jia (1991) was used. He developed a formula for calculating lanthanide ionic radii when bonded to oxygen or fluorine, as a function of the number of electrons in the *f*-orbital, the coordination number, and several other parameters. His results agree to less than 1% error with experimentally determined numbers. Because Sc and Y do not have filled *f*-orbitals, the results would not work for them. It can be safely assumed that they are of similar sizes as the HREOs since they exhibit the same crystal structure and the same coordination number. Because of their different crystal types, the modeling of LREOs will differ from the modeling of the HREOs.

Table VIII: Rare Earth Oxides Lattice Structures, Coordination Numbers, Ionic Diameters and Lattice Parameters

	Element	Lattice Structure	Coordination Number	Ionic Diameter(Å)	Lattice Parameters			
					a=b(Å)	c(Å)	α=β	γ
LREOs	La	hexagonal	7	2.46	3.93	6.12	90°	120°
	Ce	hexagonal	7	2.42	3.88	6.06	90°	120°
	Pr	hexagonal	7	2.38	3.85	6.00	90°	120°
	Nd	hexagonal	7	2.36	3.84	6.01	90°	120°
	Pm	hexagonal	7	2.34	--	--	90°	120°
	Element	Lattice Structure	Coordination Number	Ionic Diameter	Lattice Parameters			
					a=b=c(Å)		α=β=γ	
HREOs	Sm	cubic	6	2.20	10.85		90°	
	Eu	cubic	6	2.17	10.84		90°	
	Gd	cubic	6	2.16	10.79		90°	
	Tb	cubic	6	2.13	10.70		90°	
	Dy	cubic	6	2.10	10.63		90°	
	Ho	cubic	6	2.08	10.61		90°	
	Er	cubic	6	2.06	10.55		90°	
	Tm	cubic	6	2.04	10.49		90°	
	Yb	cubic	6	2.02	10.44		90°	
	Lu	cubic	6	2.00	10.39		90°	

6.1.2.1.1.   Hexagonal REOs Modeling.

To do this modeling, the hexagonal oxide with the REE of the smallest diameter was first used (i.e., Nd). Hence, after deriving the unit cell dimensions for Nd_2O_3, equations can be derived to scale up to the larger REEs. In this regard, the lattice parameters for these LREOs are needed (see Table VIII). To begin, the hexagonal crystal structure of Nd_2O_3 is shown in Figure 24. The unit cell on the right represents the bold part of the diagram on the left. The red atoms are oxygen, while the blue atoms are Nd.
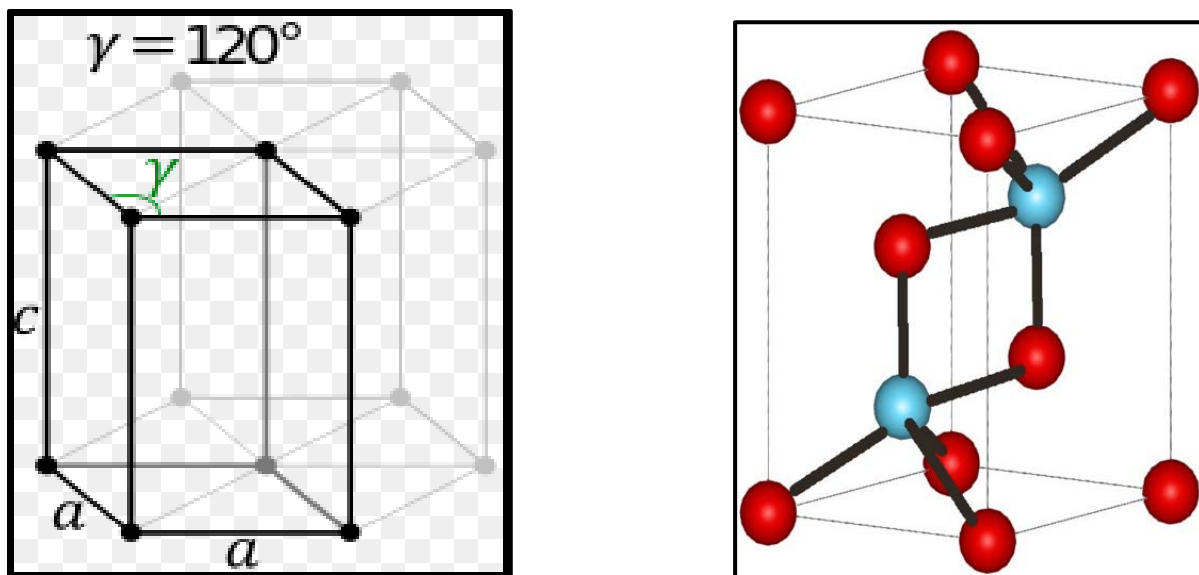
Figure 23: Unit cell representation of the Nd₂O₃ Crystal structure.

Figure 25 represents the (0-110) plane of Nd_2O_3 and is specific to the spacing of Nd atoms at the surface.
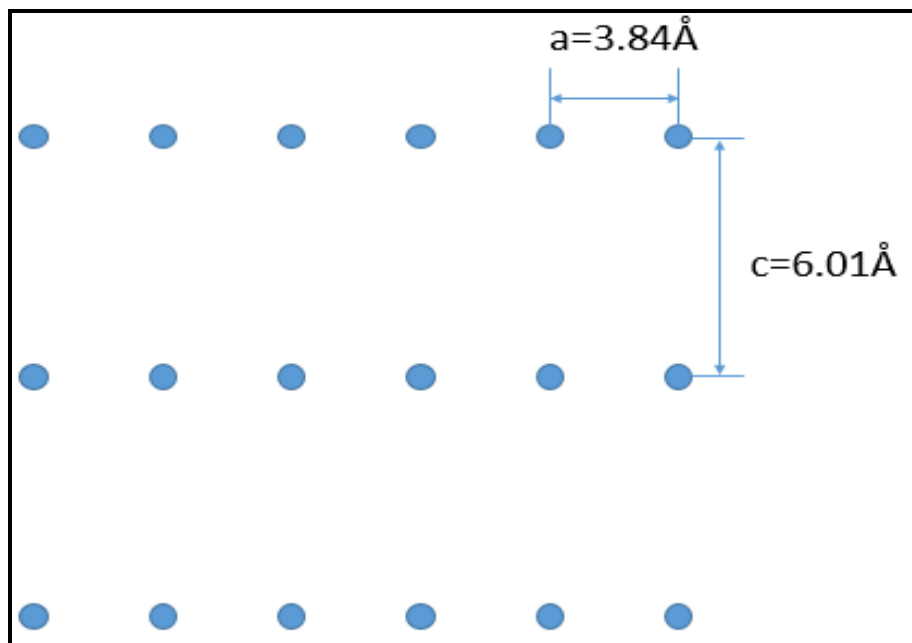
Figure 24: Representation of Nd^{+3} ions centers at the surface of a (0-110) Plane of Nd$_2$O$_3$.

If SHA adsorbs at that surface vertically, the SHA molecule can be represented by rectangles measuring 5.26 Å x 2.42 Å as shown earlier in Figure 22 and Figure 23. Thus, all the Nd sites will become occupied resulting in perfect monolayer coverage. This is shown in Figure 26. The green rectangles represent SHA molecules adsorbing onto the Nd^{+3} sites represented by blue dots. This results in a high adsorption density of 7.20 µmol/m^2:
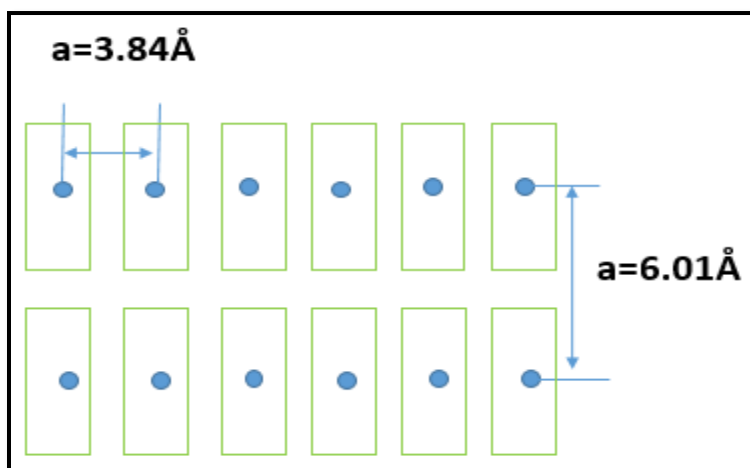
Figure 25: Vertical adsorption SHA on (0-110) plane of Nd$_2$O$_3$

$$\frac{1\ SHA\ molecule \times 10^6 \frac{\mu mol}{mol}}{\left(3.84 \times 6.01\ \text{Å}^2\right) \times \left(6.02 \times 10^{23} \frac{molecules}{mole}\right) \times \left(10^{20} \frac{m^2}{\text{Å}^2}\right)} = 7.20 \mu mol/m^2$$

Equation 24

which is approximately 55% of a LB film. Because all Nd sites are occupied, the adsorbed

monolayer would render the surface passive and essentially prevent Nd from solubilizing. Thus,

SHA surface precipitation would not be expected.

If SHA adsorbs horizontally at the surface of Nd_2O_3, there are two possibilities. The

length of SHA might align with the longer dimension of the plane, as it adsorbs on one REE site,

giving rise to a horizontal longitudinal adsorption (see Figure 27) or it might align with the

shorter dimension, giving rise to horizontal latitudinal adsorption (see Figure 28). The yellow

rectangles represent the SHA dimensions. When it adsorbs on one site, three others are impeded

from adsorption, giving a total adsorption area for one SHA molecule represented in green.
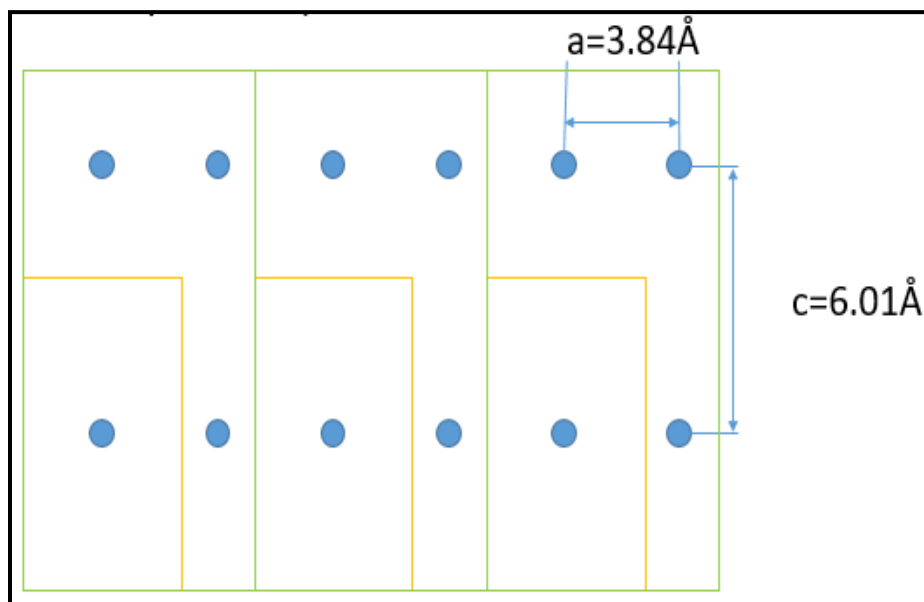
Figure 26: Horizontal longitudinal adsorption of SHA at (0-110) plane of Nd_2O_3
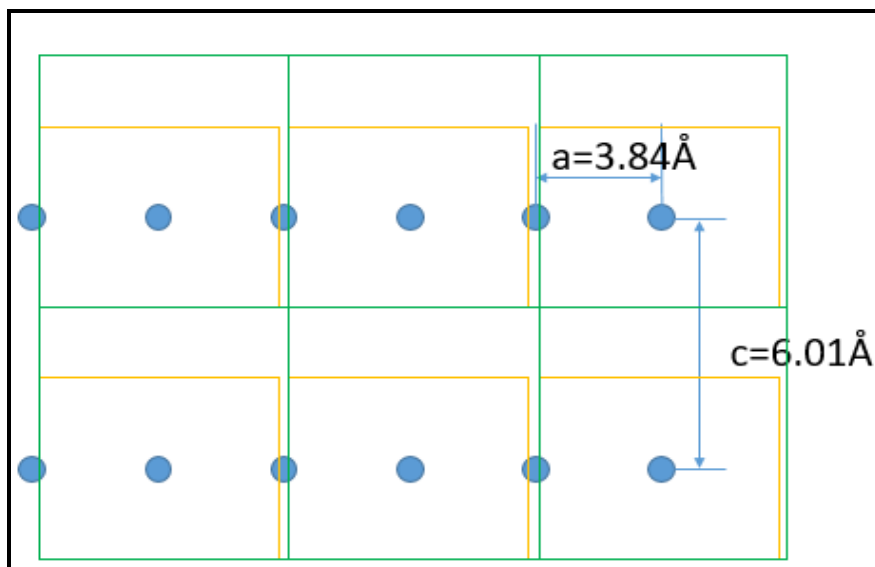
Figure 27 Horizontal latitudinal adsorption of SHA on (0-110) plane of Nd$_2$O$_3$

According to Figure 27, for every Nd site at which SHA adsorbs, three sites are impeded

from adsorption due to steric hindrance. This results in a low theoretical adsorption density of

1.80µmol/m^2:

$$\frac{1\ SHA\ molecule \times 10^6 \frac{\mu mol}{mol}}{\left(2 \times 3.84 \times 2 \times 6.01 Å^2\right) \times \left(6.02 \times 10^{23} \frac{molecules}{mole}\right) \times (10^{-20} \frac{m^2}{Å^2})} = 1.80\ \mu mol/m^2$$

Equation 25

Which is approximately 14% of an LB monolayer. Because only 25% Nd sites are occupied, the

submonolayer would allow unoccupied sites to solubilize and likely lead to surface precipitation.

By comparison, Figure 28 shows every other can get occupied thereby leading to a slightly

higher theoretical adsorption density calculated to be 3.6µmol/m^2:

$$\frac{1\ SHA\ molecule \times 10^6 \frac{\mu mol}{mol}}{\left(2 \times 3.84 \times 6.01\ Å^2\right) \times \left(6.02 \times 10^{23} \frac{molecules}{mole}\right) \times (10^{-20} \frac{sqm}{sqÅ})} = 3.60 \mu mol/m^2$$

Equation 26

which is approximately 28% of a LB film. Because only 50% of the Nd sites are occupied, the submonolayer would still allow solubilization and surface precipitation, but likely to a lesser extent.

As said above, all these results are purely qualitative. SHA adsorption on LREOs and REMs in general will not be very orderly. It can therefore be concluded that, given adequate conditions, both adsorption and surface precipitation will be responsible for REM flotation by SHA, particularly the LREO. Table IX gives a summary of adsorption densities of SHA at the (0-110) plane of each LREOs. Because all isotopes of Pm are radioactive, there was no information about its crystal structure, and so it is left blank. In general, the results show that SHA adsorption is relatively constant on the LREOs but tends to increase with increasing atomic number (La<Ce<Pr<Nd) and are very dependent on SHA's orientation at the surface as demonstrated vertically and horizontally with the latter being either latitudinal or longitudinal. Interestingly, it is predicted that surface precipitation will be greatest in the reverse order (La>Ce>Pr>Nd) because the REE sites become increasingly occupied. This order of surface precipitation was observed in Section 4 and by Galt (2017).

Table IX: Theoretical Adsorption Densities of SHA on (0-110) Plane of LREOs ($\mu mol/m^2$)

	Vertical	Horizontal Longitudinal	Horizontal Latitudinal
La	6.91	3.45	1.73
Ce	7.06	3.53	1.77
Pr	7.19	3.60	1.80
Nd	7.20	3.60	1.80
Pm	---	---	---

6.1.2.1.2.   Cubic REOs Modelling.

The previous approach for modelling SHA adsorption was used. In this case, REOs from Sm to Lu are known to have cubic crystal structure at room temperature (Atkinson, 2014). The

(001) plane was used. Equations were derived for the HREOs initially using the cubic structure

of Sc_2O_3 is shown in Figure 29.
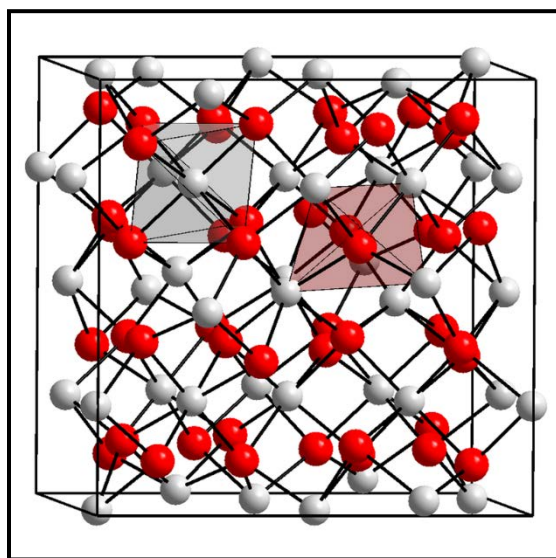
Figure 28: The cubic structure of Sc_2O_3

Illustrations for vertical, horizontal latitudinal and horizontal longitudinal are shown in Figure

30, Figure 31 and Figure 32, respectively.
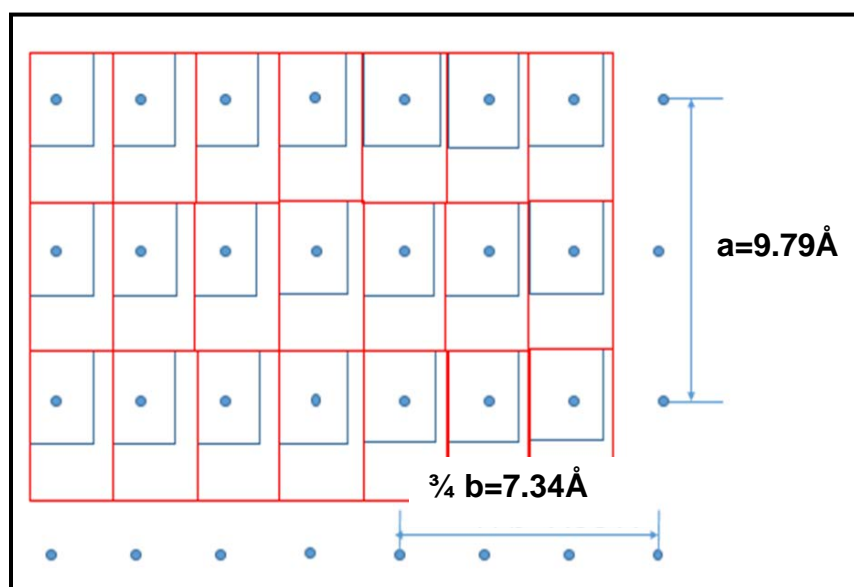
Figure 29: Vertical longitudinal at (001) plane of Sc_2O_3.
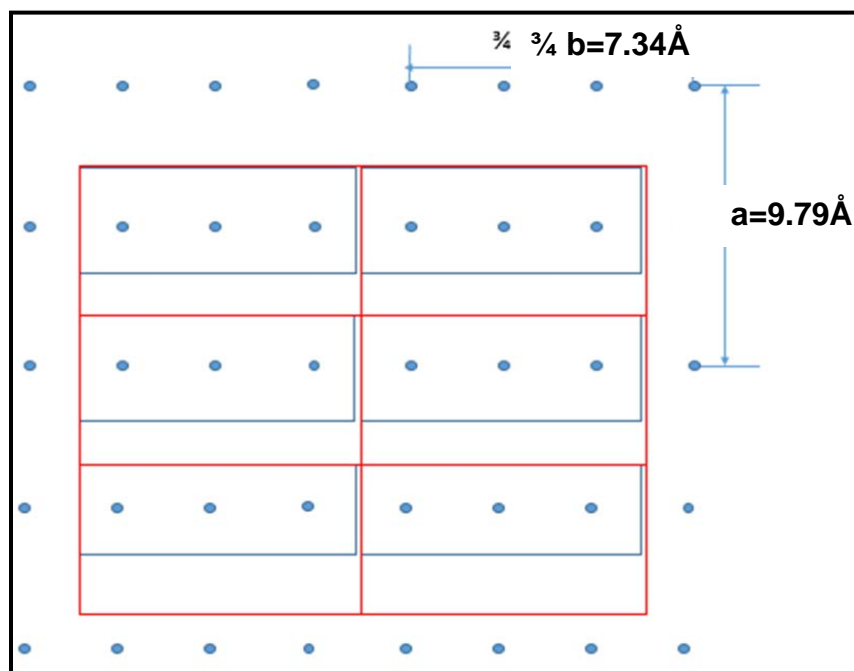
Figure 30: Horizontal latitudinal adsorption at (001) plane of Sc$_2$O$_3$.
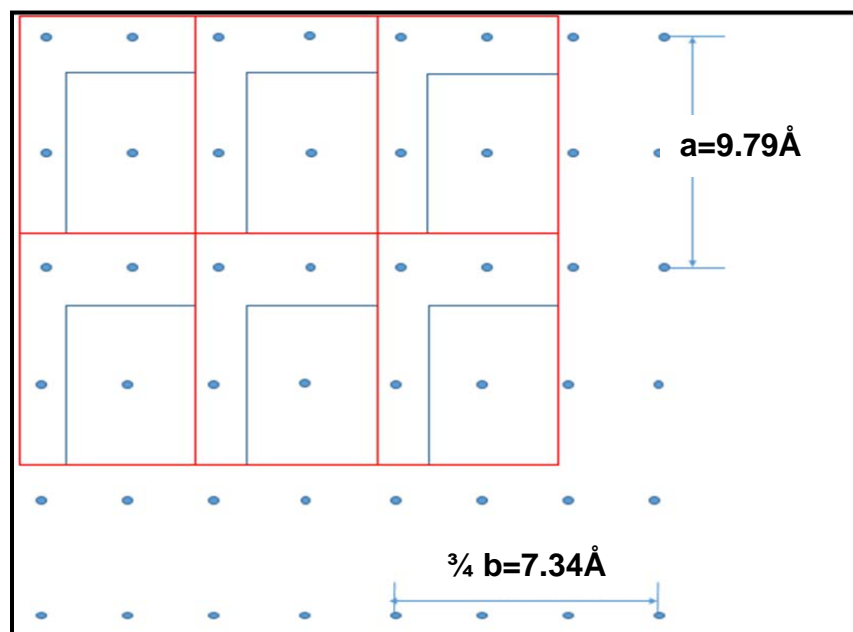
Figure 31 Horizontal longitudinal adsorption at (001) plane of Sc$_2$O$_3$.

Results of theoretical adsorption density calculations are 13.87µmol/m^2, 8.96µmol/m^2 and

2.96µmol/m^2 respectively (see Equation 27, Equation 28 and Equation 29):

$$\frac{1\ SHA\ molecule\times10^{6}\frac{\mu mol}{mol}}{\left(0.5\times9.79\times0.25\times9.79\ \text{Å}^2\right)\times\left(6.02\times10^{23}\frac{molecules}{mole}\right)\times(10^{-20}\frac{m^2}{\text{Å}^2})} = 13.87\ \mu mol/m^2$$

Equation 27

$$\frac{1\ SHA\ molecule\times10^{6}\frac{\mu mol}{mol}}{\left(0.33\times9.79\times0.5\times9.79\ \text{Å}^2\right)\times\left(6.02\times10^{23}\frac{molecules}{mole}\right)\times(10^{-20}\frac{m^2}{\text{Å}^2})} = 10.50\ \mu mol/m^2$$

Equation 28

$$\frac{1\ SHA\ molecule\times10^{6}\frac{\mu mol}{mol}}{\left(0.5\times9.79\times9.79\ \text{Å}^2\right)\times\left(6.02\times10^{23}\frac{molecules}{mole}\right)\times(10^{-20}\frac{m^2}{\text{Å}^2})} = 3.47\ \mu mol/m^2$$

Equation 29

which are equivalent to nearly 100%, 23% and 69% of a LB film. In this regard, surface

precipitation is not expected for vertical orientation, somewhat expected for horizontal latitudinal

orientation, and is expected for horizontal longitudinal orientation.

Repeating these calculations for all of the remaining REOs yields the results in Table X.

In general, the trends are the same as observed for the hexagonal LREOs and show that the

theoretical adsorption densities increase with increasing atomic number and also depend on how

SHA orients at that surface. In this case, the vertical adsorption yields 86% to 95% of an LB

film, thereby suggesting that surface precipitation will be minimal at all of their surfaces. This

would concur with the conclusions of Galt (2017) as well. However, comparing the results to

Table IX shows that the theoretical adsorption densities are practically doubled. This is an

artifact of the planes at which SHA adsorption was modeled. In this regard, it is important to

qualify the trends and not quantify the numbers.

Table X: Cubic REO Theoretical Monolayer Adsorption Densities of SHA on the (001) Plane (µmol/m²)

Element	Vertical	Horizontal Latitudinal	Horizontal Longitudinal
Sm	11.29	8.55	2.82
Eu	11.31	8.57	2.83
Gd	11.41	8.65	2.85
Tb	11.61	8.79	2.90
Dy	11.76	8.91	2.94
Ho	11.81	8.95	2.95
Er	11.94	9.05	2.98
Tm	12.08	9.15	3.02
Yb	12.20	9.25	3.05
Lu	12.31	9.33	3.08
Sc	*13.06	10.50	3.47
Y	11.83	8.96	2.96

*The monolayer adsorption density for Sc (13.87µmol/m²) is slightly higher than the LB film. So, the Langmuir Blodgett monolayer was listed instead.

6.1.2.2.   SHA-REP Modeling

As shown in Table XI and discussed in Section 2.2.3., LREPs are monoclinic with a

coordination number of 9, and HREPs are tetragonal with a coordination number of 8. Various

lattice parameters are also shown to calculate lattice spacing.

Table XI: REP Lattice Structures, Coordination Numbers, Ionic Diameters and Lattice Parameters

	Element	Lattice Structure	Coordination Number	Ionic Diameter	Lattice Parameters				
					a(Å)	b(Å)	c(Å)	α=γ	β
LREPs	La	Monoclinic	9	2.70	8.25	7.09	6.47	90°	126.16°
	Ce	Monoclinic	9	2.67	6.77	7.04	6.46	90°	104.00°
	Pr	Monoclinic	9	2.64	6.76	6.98	6.43	90°	103.53°
	Nd	Monoclinic	9	2.60	6.74	6.95	6.40	90°	103.68°
	Pm	Monoclinic	9	2.57					
	Sm	Monoclinic	9	2.54	6.68	6.89	6.37	90°	103.86°
	Eu	Monoclinic	9	2.52	6.66	6.86	6.35	90°	103.96°
	Gd	Monoclinic	9	2.49	6.64	6.84	6.33	90°	103.98°

	Element	Lattice Structure	Coordination Number	Ionic Diameter	Lattice Parameters		
					a=b(Å)	c(Å)	α=β=γ
HREPs	Tb	Tetragonal	8	2.36	6.93	6.06	90°
	Dy	Tetragonal	8	2.33	6.91	6.04	90°
	Ho	Tetragonal	8	2.30	6.88	6.02	90°
	Er	Tetragonal	8	2.29	6.85	6.00	90°
	Tm	Tetragonal	8	2.27	6.83	5.98	90°
	Yb	Tetragonal	8	2.50	6.81	5.96	90°
	Lu	Tetragonal	8	2.23	6.78	5.95	90°
Sc and Y	Sc	Tetragonal	8		6.59	5.81	90°
	Y	Tetragonal	8		6.89	6.03	90°

6.1.2.2.1. Monoclinic REP Modeling

Figure 33 illustrates the monoclinic crystal structure. The (001) plane illustrated in Figure 34 was chosen for this modeling. Illustrations for vertical, horizontal longitudinal and horizontal latitudinal are shown in Figure 35, Figure 36 and Figure 37, respectively. Results of theoretical adsorption density calculations are 7.31 μmol/m^2, 2.57 μmol/m^2 and 2.44 μmol/m^2 as determined by Equation 30, Equation 31 and Equation 32, respectively.
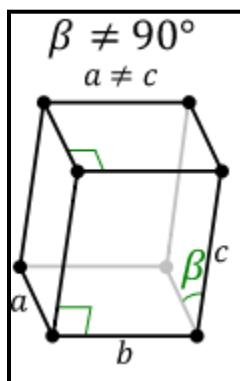
Figure 32: Representation of the monoclinic crystal structure
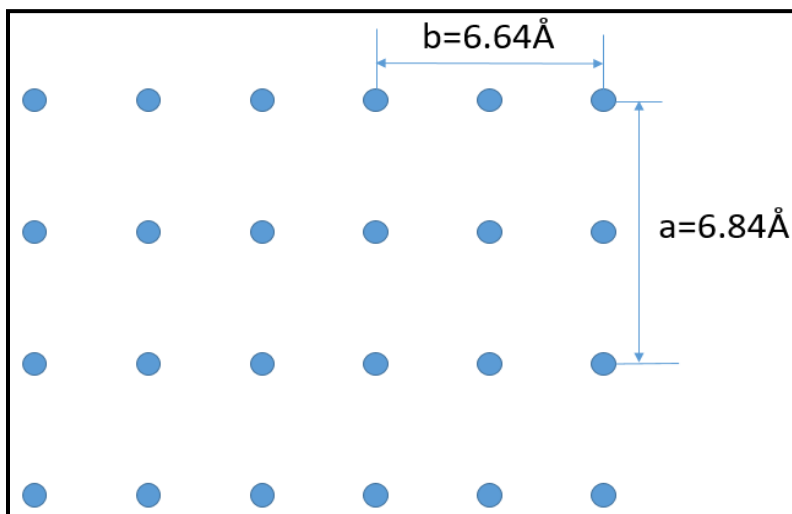
Figure 33: Representation of Gd^{+3} ions centers on the surface of a (001) plane of Gd$_2$O$_3$.
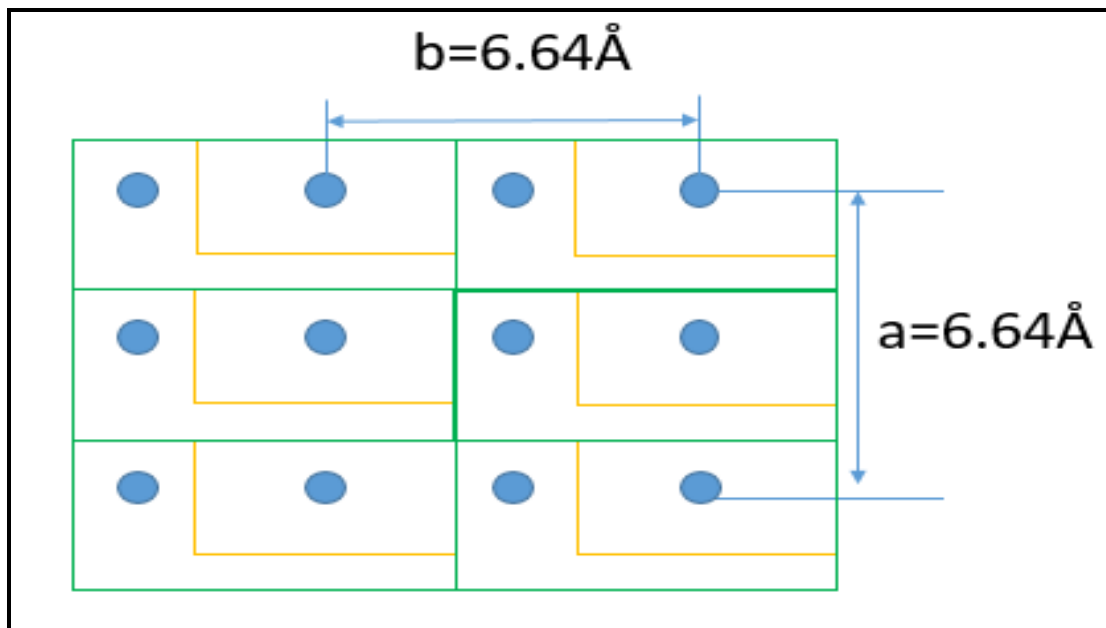
Figure 34: Vertical adsorption of SHA on (001) plane of Gd_2O_3
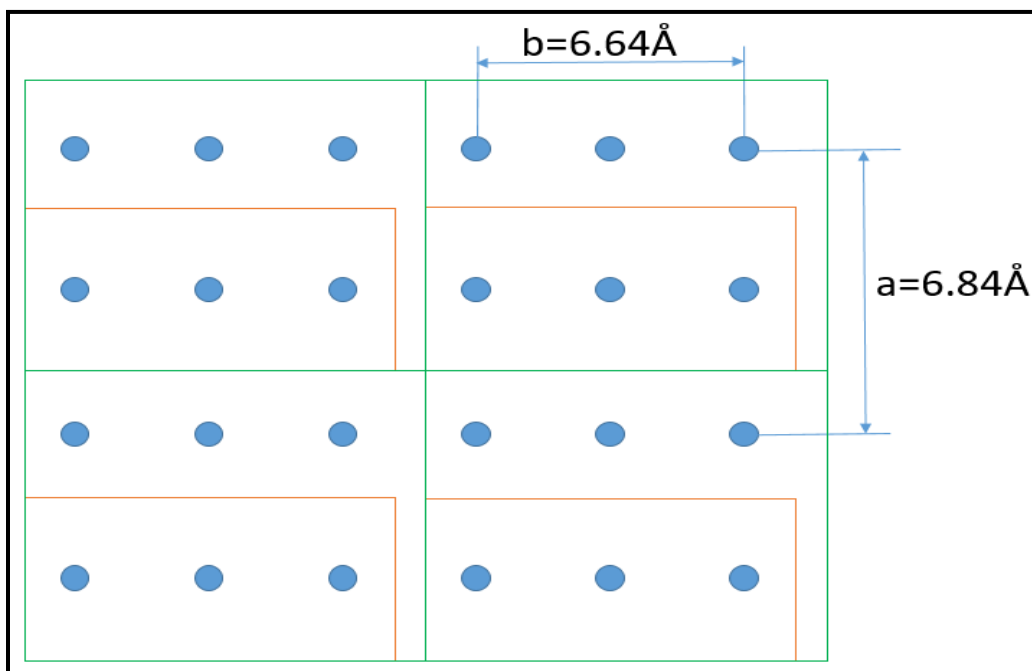
Figure 35: Horizontal longitudinal adsorption of SHA on (001) plane of Gd_2O
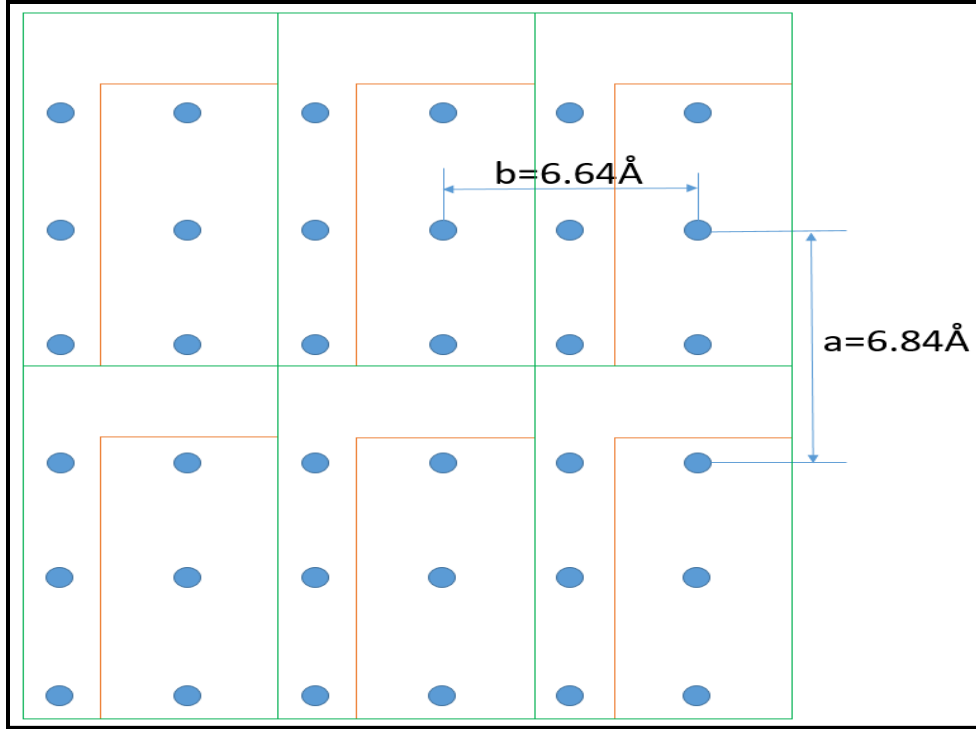
Figure 36: Horizontal latitudinal adsorption of SHA on (001) plane of Gd$_2$O$_3$

$$\frac{1\ SHA\ molecule \times 10^6 \frac{\mu mol}{mol}}{\left(6.64 \times 0.5 \times 6.84\ Å^2\right) \times \left(6.02 \times 10^{23} \frac{molecules}{mole}\right) \times \left(10^{-20} \frac{m^2}{Å^2}\right)} = 7.31\ \mu mol/m^2$$

Equation 30

$$\frac{1\ SHA\ molecule \times 10^6 \frac{\mu mol}{mol}}{\left(6.64 \times 1.33 \times 6.84 Å^2\right) \times \left(6.02 \times 10^{23} \frac{molecules}{mole}\right) \times \left(10^{-20} \frac{m^2}{Å^2}\right)} = 2.75\ \mu mol/m^2$$

Equation 31

$$\frac{1\ SHA\ molecule \times 10^6 \frac{\mu mol}{mol}}{\left(1.5 \times 6.64 \times 6.84 Å^2\right) \times \left(6.02 \times 10^{23} \frac{molecules}{mole}\right) \times \left(10^{-20} \frac{m^2}{Å^2}\right)} = 2.44\ \mu mol/m^2$$

Equation 32

Vertical adsorption is approximately 60% of an LB film, with 50% of Gd sites free.

Similarly, upon horizontal longitudinal and latitudinal adsorption, only a fraction of the Gd sites

will become occupied. Therefore, free Gd sites are expected to solubilize and surface precipitate.

Results for monoclinic REP modelling are summarized in Table XII.

Table XII: Monoclinic REP Theoretical Monolayer Adsorption Densities of SHA on the (001) Plane (μmol/m^2).

Element	Vertical	Horizontal Latitudinal	Horizontal Longitudinal
La	5.68	2.14	1.89
Ce	6.97	2.62	2.32
Pr	7.04	2.65	2.35
Nd	7.09	2.67	2.37
Pm	---	---	---
Sm	7.22	2.71	2.41
Eu	7.27	2.73	2.42
Gd	7.31	2.75	2.44

6.1.2.2.2. Tetragonal REP Modeling

The HREPs are tetragonal (see Figure 38 and Table XI). In this case, the choice of the

same (001) plane also makes modeling easier. Figure 39 shows the lattice spacing of Sc in

ScPO$_4$. Clearly, Sc^{+3} sites on the (001) plane are equally separated in both dimensions. Thus, in

this case, adsorption will only be vertical or horizontal, independent of it being latitudinal or

longitudinal
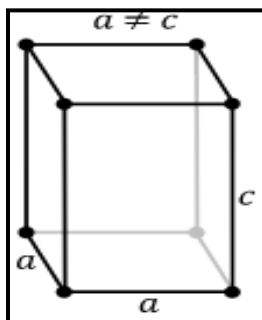
Figure 37: Representation of the simple tetragonal crystal structure
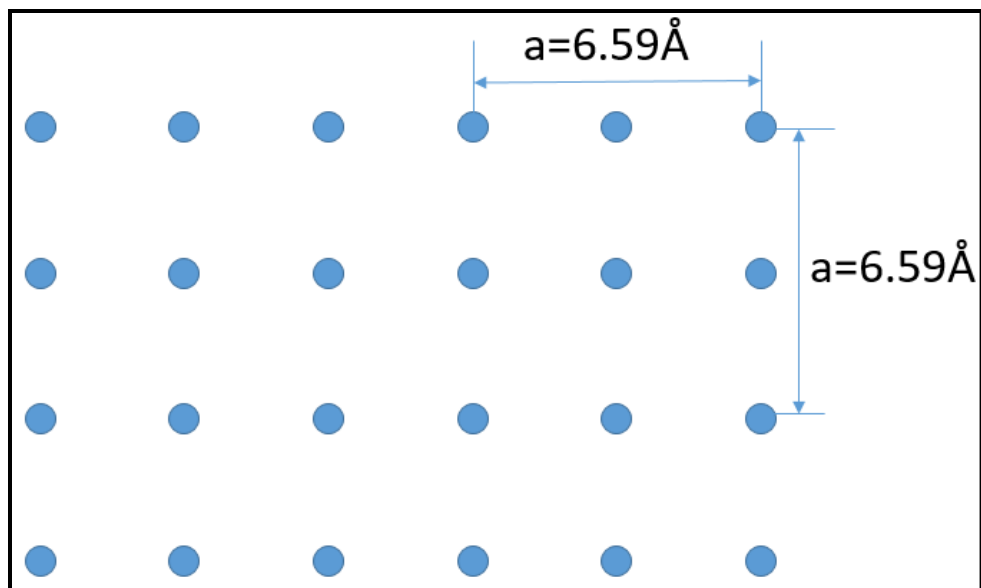
Figure 38: Representation of Sc^{+3} ions centers on the surface of a (001) plane of Sc$_2$O$_3$.

Vertical adsorption illustrated in Figure 39, indicates that 50% of all Sc sites are unoccupied, yielding an adsorption density of 7.65µmol/m^2:

$$\frac{1 \: SHA \: molecule \times 10^6 \frac{\mu mol}{mol}}{\left(0.5 \times 6.59 \times 6.59 \: sq\text{Å}\right) \times \left(6.02 \times 10^{23} \frac{molecules}{mole}\right) \times \left(10^{-20} \frac{m^2}{\text{Å}^2}\right)} = 7.65 \: \mu mol/m^2$$

Equation 33

which is approximately equivalent to 58.6% of a LB film. Surface precipitation is to therefore to be expected.
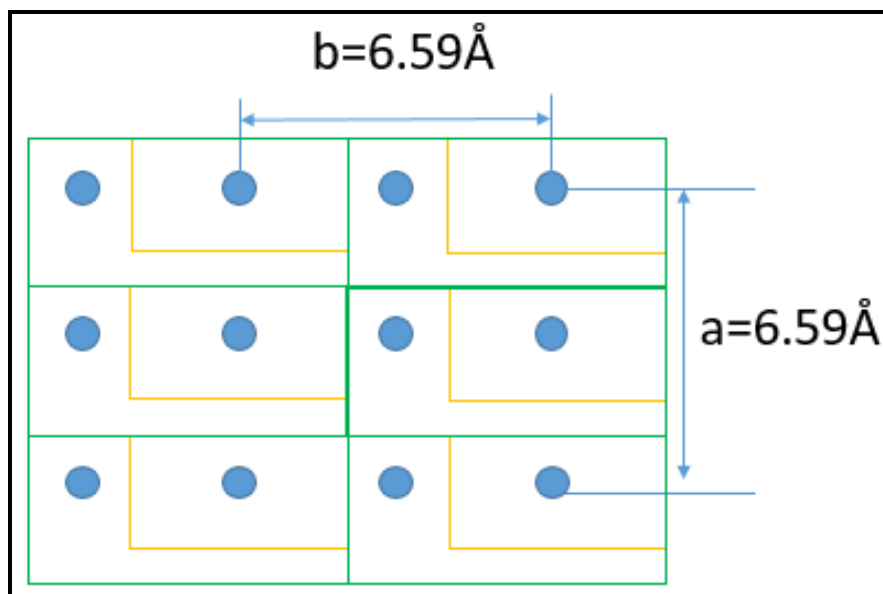
Figure 39: Vertical adsorption of SHA on (001) plane of Sc$_2$O$_3$

By comparison, Figure 41 shows SHA adsorbing horizontally and suggests that the adsorption at one site will sterically hinder adsorption at other sites; however, two sites will be masked and three sites will not be. All five of these unoccupied sites will lead to surface precipitation but will be hindered at the two masked sites. This leads to an adsorption density of 2.88 µmol/m^2 :

$$\frac{1 \; SHA \; molecule \times 10^6 \frac{\mu mol}{mol}}{\left(1.33 \times 6.59 \times 6.59 Å^2\right) \times \left(6.02 \times 10^{23} \frac{molecules}{mole}\right) \times \left(10^{-20} \frac{m^2}{Å^2}\right)} = 2.88 \; \mu mol/m^2$$

Equation 34

which correlates to about 22% of a LB film

Repeating the calculations for the other tetragonal REPs, i.e., the HREPs, yields the results in Table XIII. Once again, adsorption increase with increasing atomic number and is dependent on SHA orientation due to steric hindrance caused by the size of SHA. In this case, vertical orientation ranges from 50% to 60% of a LB film which suggests SHA surface precipitation will occur.
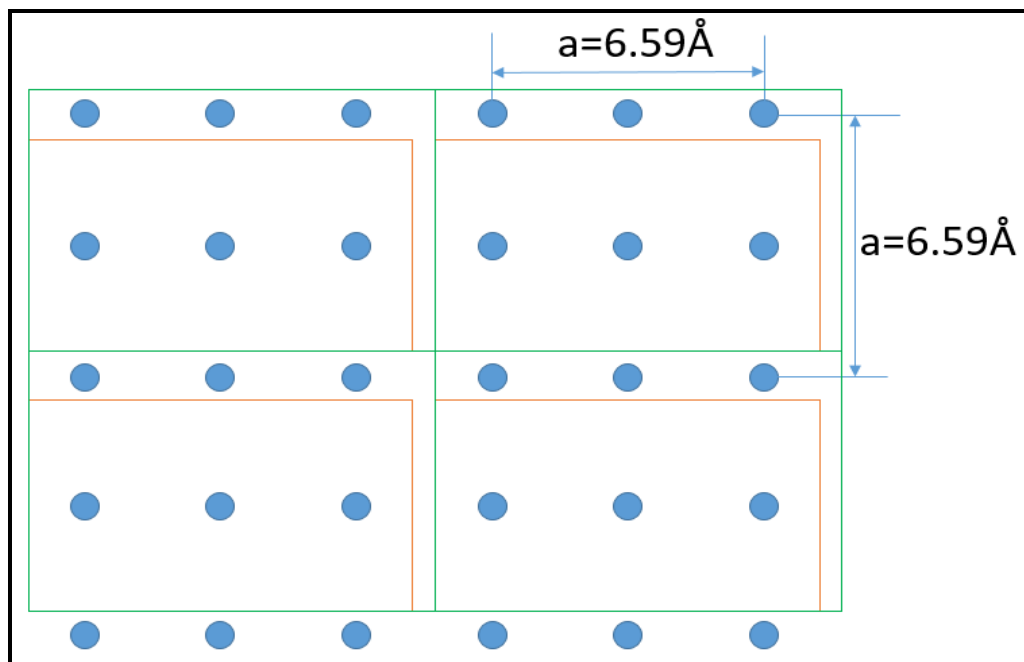
Figure 40: Horizontal adsorption of SHA on (001) plane of Sc_2O_3

Table XIII: Tetragonal REP Theoretical Monolayer Adsorption Densities of SHA on the (001) Plane ($\mu mol/m^2$).

Element	Vertical	Horizontal
Tb	6.92	2.60
Dy	6.97	2.62
Ho	7.02	2.64
Er	7.08	2.66
Tm	7.12	2.68
Yb	7.17	2.69
Lu	7.22	2.71
Sc	7.65	2.88
Y	6.99	2.63

6.1.3. SHA-REC Modelling

Multiple sources, as discussed in Section 2.2.2 attest to the fact that all RECs are orthorhombic in crystal structure. They, however, do not give dimensions of the unit cells as was the case with REOs and RECs. In this section, the calculations are approximated by doing a regression analysis and using the resulting equation to estimate parameters not given in literature. La, Pr, Nd and Er carbonates crystal structures were obtained from (Caro et al., 1972). Ce carbonate from (Bevins et.al. 1985). All the extrapolated parameters are printed in red, while all those obtained from literature will be left in black. This technique does not apply to Sc and Y because they are not lanthanides. Consequently, they are ignored. Figure 42 shows the regression analysis and Table XIV shows the results. It is important to note that the regressions yielded R^2 values near 0.98 which gives strong confidence in the results. However, caution is shared because numbers are being estimated from five data points, and four of those are in close proximity to one another, and the fifth point is not; it is this fifth point that controls the regression. Nevertheless, it is the qualifications that are of main concern and not the precise quantifications.

Table XIV: REC Lattice Structures, Coordination Numbers, Ionic Diameters and Lattice Parameters (from literature and estimated)

Element	Lattice Structure	Coordination Number	Ionic Diameter	Lattice Parameters			
				a(Å)	b(Å)	c(Å)	α=β=γ
La	orthorhombic	10	2.80	9.00	9.56	17.02	90°
Ce	orthorhombic	10	2.78	8.97	9.48	16.94	90°
Pr	orthorhombic	10	2.72	8.91	9.49	16.93	90°
Nd	orthorhombic	10	2.70	8.89	9.44	16.90	90°
Pm	orthorhombic	10	2.68	8.48	9.45	16.63	90°
Sm	orthorhombic	10	2.66	7.85	9.36	16.21	90°
Eu	orthorhombic	10	2.62	7.66	9.34	16.08	90°
Gd	orthorhombic	10	2.62	7.04	9.26	15.66	90°
Tb	orthorhombic	10	2.58	6.85	9.23	15.53	90°
Dy	orthorhombic	10	2.56	6.43	9.18	15.24	90°
Ho	orthorhombic	10	2.52	6.14	9.14	15.05	90°
Er	orthorhombic	10	2.52	6.05	9.13	15.00	90°
Tm	orthorhombic	10	2.50	5.67	9.08	14.73	90°
Yb	orthorhombic	10	2.48	5.19	9.02	14.41	90°
Lu	orthorhombic	10	2.46	4.96	8.99	14.25	90°

Figure scatter plot with regression lines:
$y = -0.0397x + 35.292$, $R^2 = 0.9794$ (c)
$y = -0.0076x + 13.017$, $R^2 = 0.9844$ (b)
$y = -0.0588x + 36.119$, $R^2 = 0.9765$ (a)

Axis labels: a, b and c (Å); REC molecular weight (g/mol)
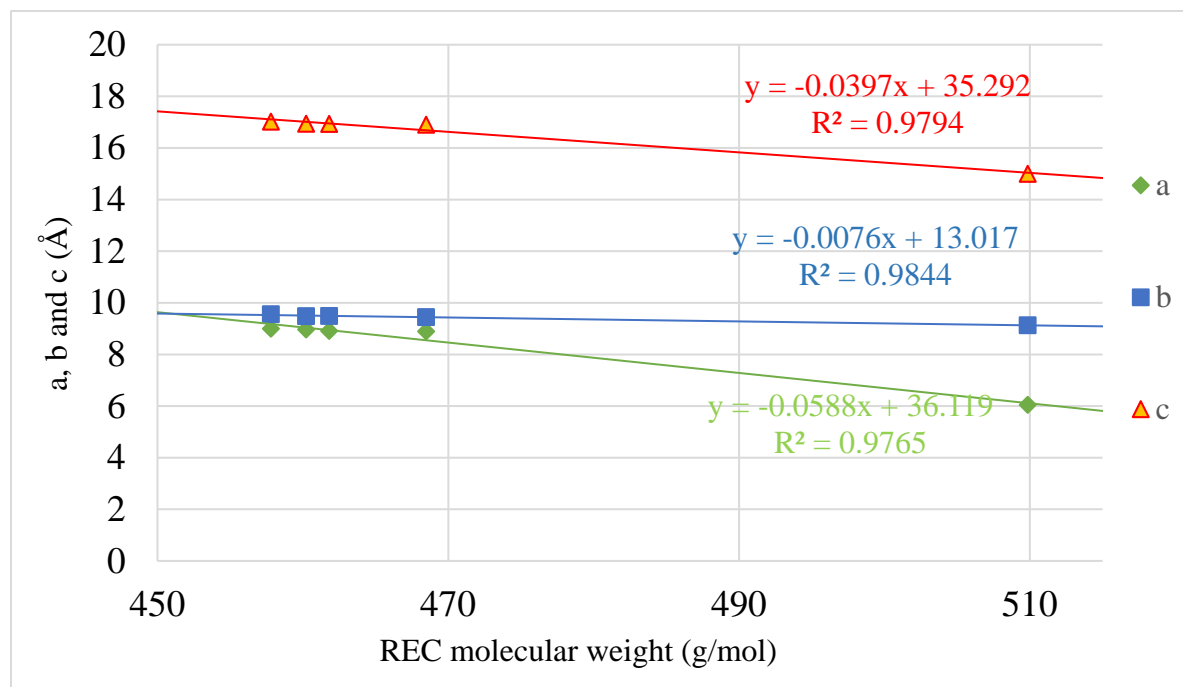
Figure 41: Regression analysis on a, b, and c lattice parameters for RECs

Figure 42 shows the crystal structure of $La_2(CO_3)_3$ and Figure 44 illustrates the spacing between La sites in its (001) plane. Vertical SHA adsorption is illustrated in Figure 45 and horizontal longitudinal and latitudinal SHA adsorption are shown in

Figure 45 and Figure 47 respectively.
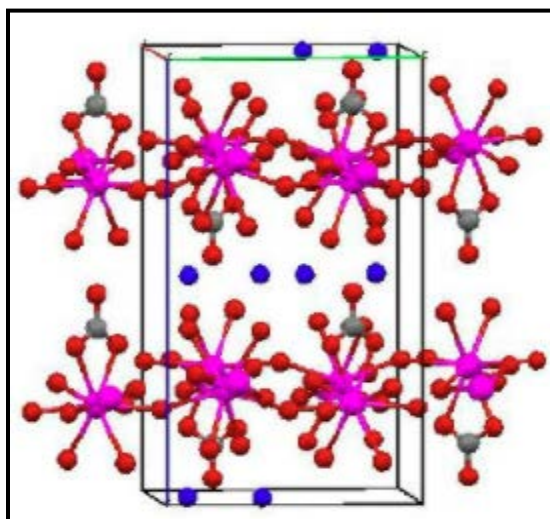
Figure 42: Crystal structure of $La_2(CO_3)_3$ viewed along the b axis with La in pink, O in red and C in grey (researchgate.net, 2013).
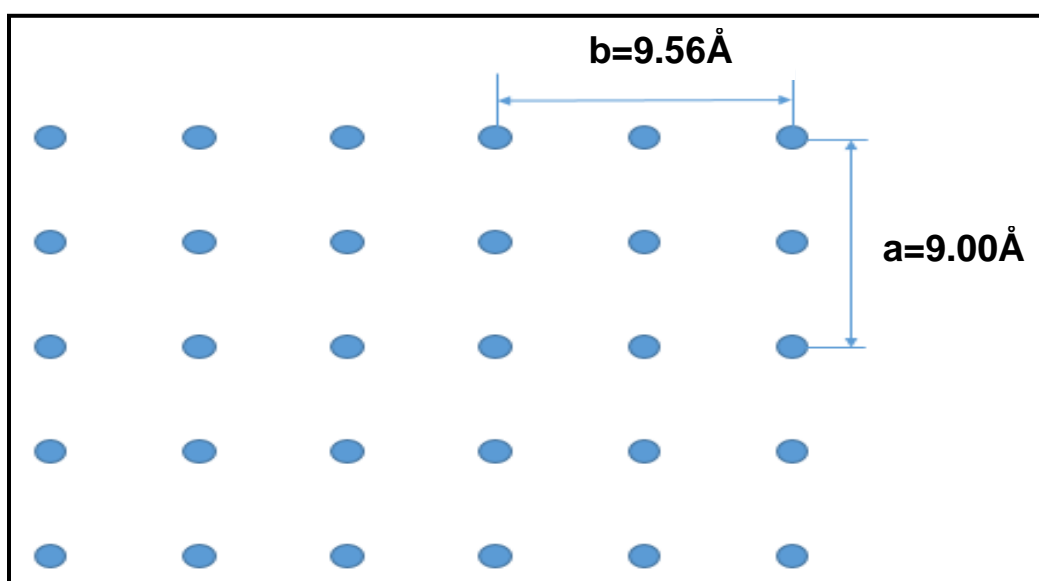
Figure 43: Plane (001) of $La_2(CO_3)_3$
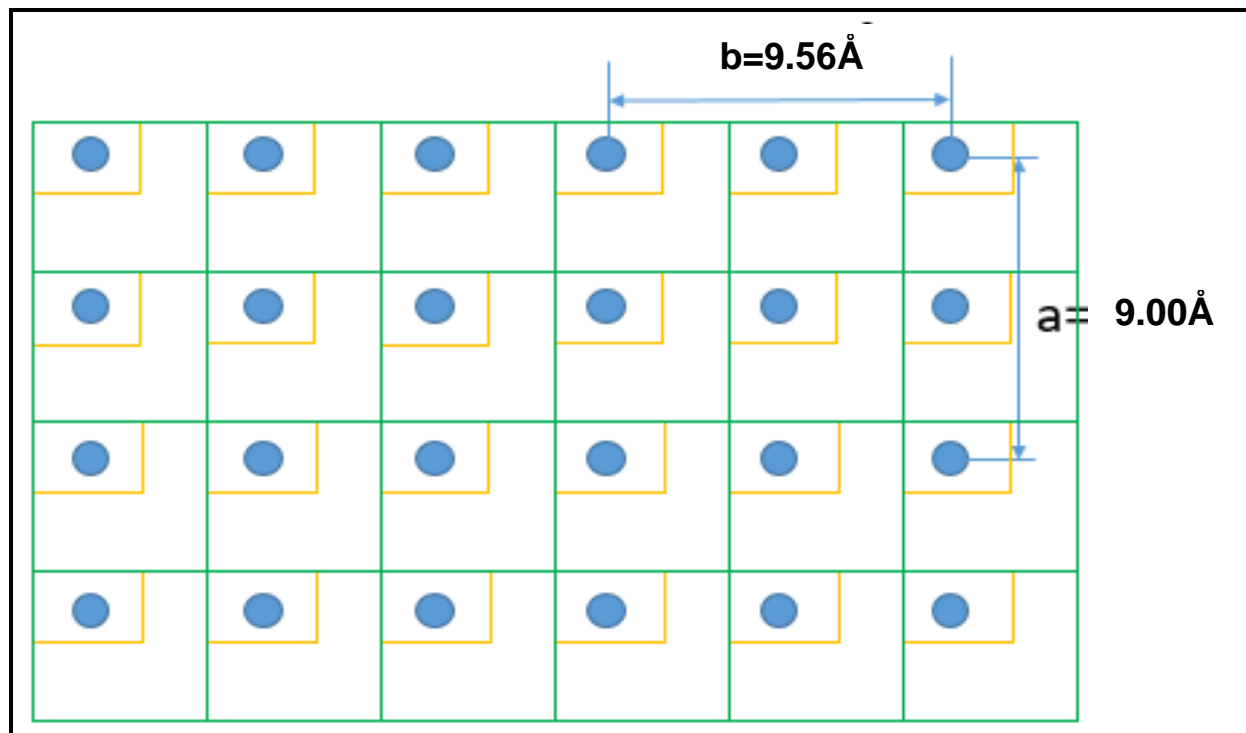
Figure 44: SHA vertical adsorption of SHA at the (001) plane of La$_2$(CO$_3$)$_3$
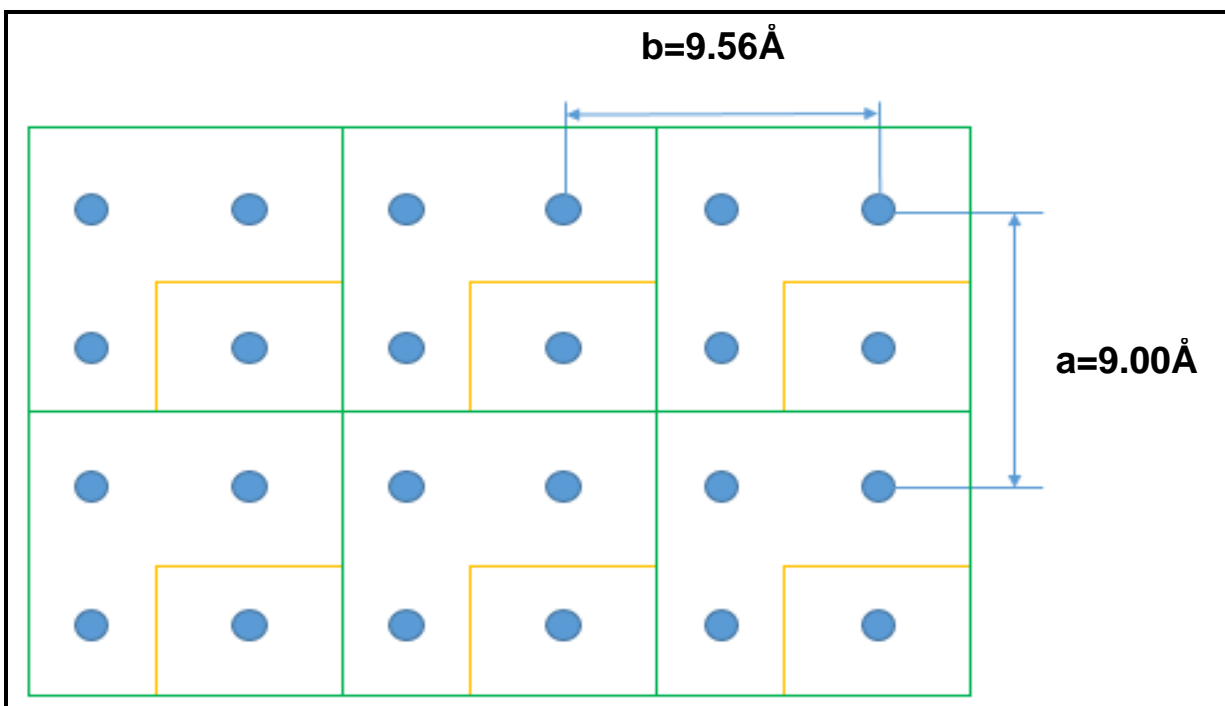
Figure 45 Horizontal longitudinal adsorption of SHA at the (001) plane of La$_2$(CO$_3$)$_3$
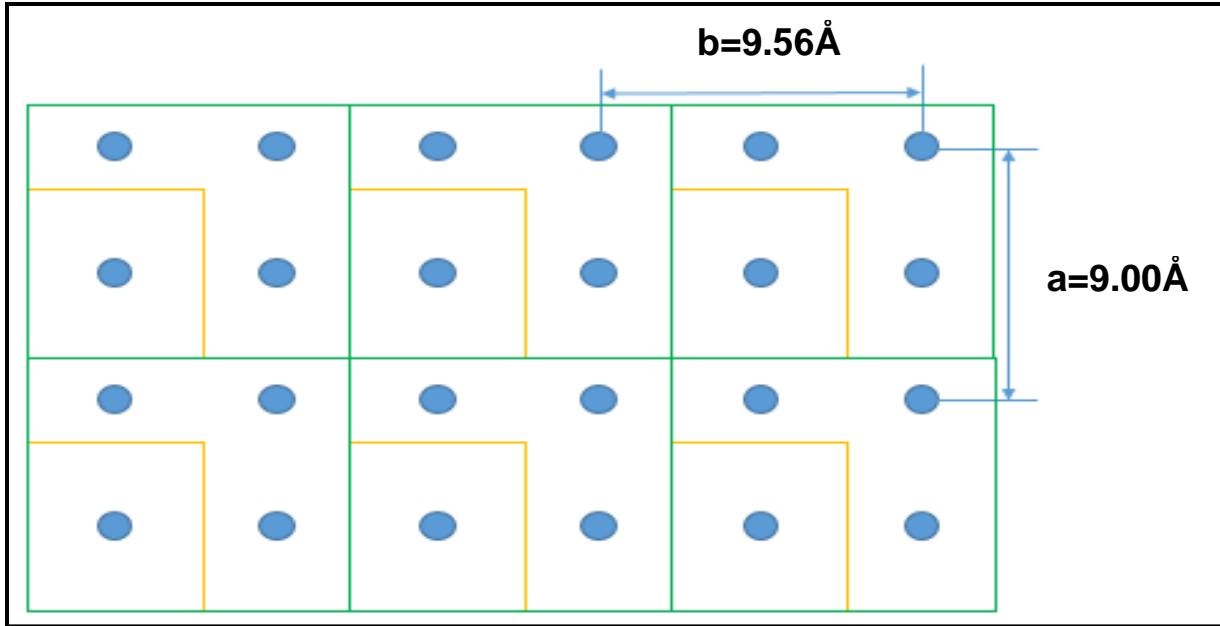
Figure 46: Horizontal latitudinal adsorption of SHA at the (001) plane of La₂(CO₃)₃

Vertical adsorption in Figure 45 indicates all La sites will be occupied with an adsorption

density of 7.73 µmol/m². This equates to approximately 60% of a LB film:

$$\frac{1\ SHAmolecule\times10^6\frac{\mu mol}{mol}}{\left(0.5\times9.00\times0.5\times9.56\ Å^2\right)\times\left(6.02\times10^{23}\frac{molecules}{mole}\right)\times(10^{-20}\frac{m^2}{Å^2})} = 7.73\ \mu mol/m^2$$

Equation 35

In this case, passivation will occur and surface precipitation will be avoided. By comparison,
Figure 45 and Figure 47 both show that only 25% of La sites will be occupied with adsorption

densities of 1.93 µmol/m².

$$\frac{1\ SHA\ molecule\times10^6\frac{\mu mol}{mol}}{\left(9.00\times9.56\ sqÅ\right)\times\left(6.02\times10^{23}\frac{molecules}{mole}\right)\times(10^{-20}\frac{m^2}{Å^2})} = 1.93\ \mu mol/m^2$$

Equation 36

Clearly, in this case, passivation would not occur.

Similarly, the lattice parameters in Table XIV were used to calculate the lattice spacings

of REE sites at (001) plane of the other REC orthorhombic crystals. SHA adsorption modeling

then conducted assuming vertical and horizontal orientations. Results are presented in Table .

Once again these same trends observed for REOs and REPs are observed here for RECs.

Table XV: Orthorhombic REC Theoretical Monolayer Adsorption Densities of SHA on the (001) Plane ($\mu mol/m^2$).

Element	Vertical	Horizontal
La	7.73	1.93
Ce	7.82	1.95
Pr	7.86	1.96
Nd	7.91	1.98
Pm	8.29	2.07
Sm	9.04	2.26
Eu	9.28	2.32
Gd	10.19	2.55
Tb	10.51	2.63
Dy	11.27	2.82
Ho	11.84	2.96
Er	12.03	3.01
Tm	12.91	3.23
Yb	*14.21	3.55
Lu	*14.91	3.73

Both vertical and horizontal adsorption values increase with atomic number, with the former approximately reaching a SHA LB film at Tm, and becoming higher than a LB film for Yb and Lu. Consequently, the adsorption densities for Yb and Lu cannot be calculated based on the models in Figure 45 and Figure 47. Thus, they were recalculated to include steric hindrance. It is noted that

the cell dimensions of $Yb_2(CO_3)_3$ and $Lu_2(CO_3)_3$ are too small in comparison to the other RECs

such that 50% of sites are occupied instead of 100%. (see Figure 48). Thus, the maximum

adsorption values for $Yb_2(CO_3)_3$ and $Lu_2(CO_3)_3$ were calculated using Equation 37 and Equation 38 and are listed in Table XV but clearly do not follow the established pattern.
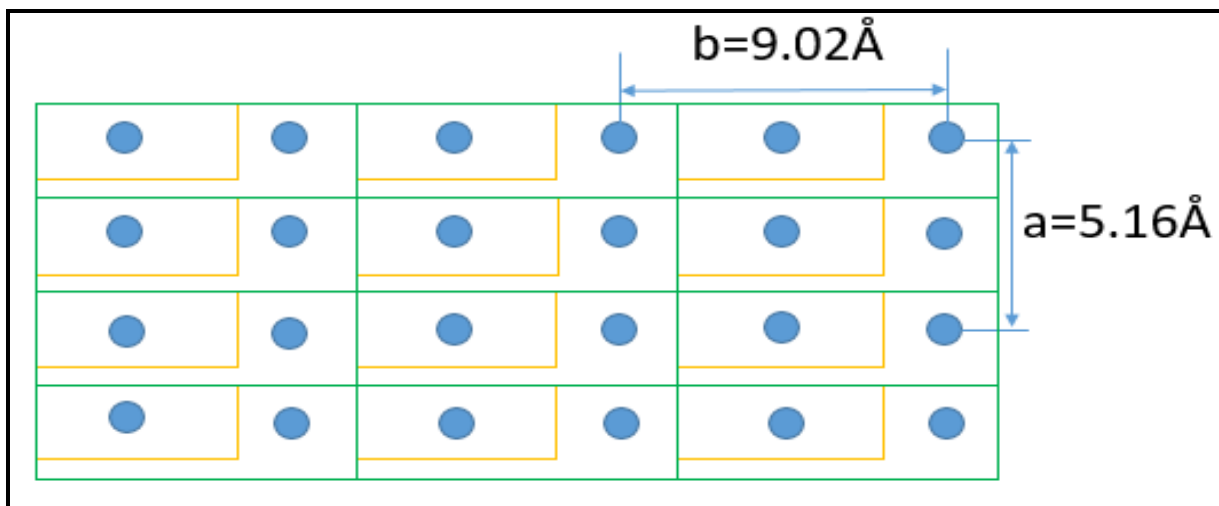
Figure 47: SHA vertical adsorption at (001) plane for $Yb_2(CO_3)_3$

$$\frac{1\ SHAmolecule \times 10^6 \frac{\mu mol}{mol}}{(9.02 \times 0.5 \times 5.16\ \text{Å}^2) \times \left(6.02 \times 10^{23} \frac{molecules}{mole}\right) \times (10^{-20} \frac{m^2}{\text{Å}^2})} = 7.10\ \mu mol/m^2$$

Equation 37

$$\frac{1\ SHAmolecule \times 10^6 \frac{\mu mol}{mol}}{(8.99 \times 0.5 \times 4.96\ \text{Å}^2) \times \left(6.02 \times 10^{23} \frac{molecules}{mole}\right) \times (10^{-20} \frac{m^2}{\text{Å}^2})} = 7.45 \mu mol/m^2$$

Equation 38

It can be observed that SHA adsorption increases with atomic number up to a maximum at Tm, and then drops. This is because surface coverage drops by approximately 50% from Er to Yb, suggesting that for Yb and Lu surface precipitation is to be expected, unlike La through Er. Studies by Galt (2017) and Trant (2018) suggest that for RECs, adsorption is maximum in the heaviest and minimum in the lights. The trend observed here explains the findings of Galt (2017)

and Trant (2018): In the heavies, SHA does not completely passivate the surface, such that more than a monolayer of adsorption can be observed, leading to a higher overall adsorption density.

7. Final Conclusions

The goal of this study was to elucidate the adsorption mechanism of SHA on REMs. It was done using two complementary methods: precipitation studies and modelling.

REEs consist of the fifteen lanthanides as well as Sc and Y. They are relatively abundant in the Earth's Crust. The term "rare" is used to indicate that scarcity of deposits rich enough to allow for economic beneficiation. They are crucial to several domains important to the US Department of Defense, and therefore there is an incentive to investigate their extraction from REMs.

REEs occur mostly as tripositive cations in REMs with O^{2-}, CO_3^{2-} and PO_4^{3-} as some of the most common counter ions. That is why fundamental studies were done on REOs, RECs and REPs. Their ionic diameters depend greatly on their coordination numbers, which are in turn determined by their crystal structures. LREOs are hexagonal, while HREOs are cubic. RECs are orthorhombic. LREPs are monoclinic, and HREPs are tetragonal.

The experimental part of the investigation consisted of synthesizing SHA-REO precipitates, and analyzing them with XRPD and LRS. Results showed that SHA adsorption occurs through a displacement of the hydroxide ion at the surface in an ion exchange mechanism, leading to surface chemisorption and precipitation. Chemisorption predominates in the heavier REOs, while Surface precipitation predominates in the LREOs.

SHA was found to protonate at pH 12.3. Based on the free energy SHA⁻ anion, the free energy of protonated SHA (i.e., SHAH) was determined to be 70.20 kJ/mol. When this value was included in REE-SHA speciation/solubility diagrams, subtle changes in the diagram were observed but remained essentially the same. Thus, the calculations by Galt (2017) are predominantly accurate.

Modelling revealed that adsorption of SHA on REMs' surface is dependent upon the orientation of SHA at the surface as well as the distance between REE sites at the surface. In general, adsorption is relatively constant within each crystal structure type, and increases steadily with atomic number. Where adsorption density nears a LB film, the surface gets passivated by a monolayer of adsorption and surface precipitation is not expected. This is the case with HREOs. Hence it is concluded that surface precipitation is expected for LREOs, but not for HREOs. This is verified by the precipitation studies in Section 4 and by Trant (2018).

For RECs, modelled adsorption densities increase to a near LB film at Tm, and drops at Yb and Lu, thereby leading to the conclusion that they behave opposite that of REOs: surface precipitation on HRECs whereas chemisorption predominates on LREOs. This modelling conclusion is also corroborated by Galt (2017) and Trant (2018).

REP modelling show that only 20% to 60% of a LB film forms from La to Lu, suggesting that both chemisorption and surface precipitation predominate for all REPs, no matter if they are LREPs or HREPs. Unlike the REOs and the RECS, the REPs did not significantly favor adsorption or surface precipitation suggesting that SHA essentially behaved the same on all. Trant (2018) corroborates these conclusions.

If for modelling, other planes were chosen, the actual values for adsorption densities calculated in each cases would change, but the relative values as well as the trends observed and discussed would likely remain the same.

8. Suggested Future Studies

- Determine the Gibbs free energy of REE(SHA)$_{3(s)}$ precipitates;

- Use these free energies in Stabcal to calculate more accurate speciation/stability diagrams;

- Examine rare earth silicates (RESs) and estimate their coordination numbers;

- Do reverse regression analysis to determine the Pm parameters for REOs and REPs; and

- Create a computer program/algorithm to model SHA on all the planes in various REM crystal structures.

9. Bibliography

1. Alonso, E., Sherman, A. M., Wallington, T. J., Everson, M. P., Field, F. R., Roth, R., & Kirchain, R. E. (2012). Evaluating rare earth element availability: A case with revolutionary demand from clean technologies. *Environmental Science and Technology*, *46*(6), 3406–3414. http://doi.org/10.1021/es203518d.

2. Atkins, P., Overton, P. T., Rourke, J., Weller, M., & Armstrong, F. (2010). *Shriver & Atkins' Inorganic Chemistry* (Fifth). Oxford: Oxford University Press.

3. Bärnighausen, H., & Schiller, G. (1985). The crystal structure of A-Ce2O3. *Journal of The Less-Common Metals*, *110*(1–2), 385–390. http://doi.org/10.1016/0022-5088(85)90347-9.

4. Bevins, R.E. Rowbotham, G. Stephens, F.S. Turgoose, S. Williams, P. A. (1985). Lanthanite-(Ce), (Ce, La, Nd)2.8H2O, a new mineral from Wales, U.K. *American Mineralogist*, *70*, 411–413.

5. Binnemans, K., Jones, P. T., Blanpain, B., Van Gerven, T., Yang, Y., Walton, A., & Buchert, M. (2013). Recycling of rare earths: A critical review. *Journal of Cleaner Production*, *51*, 1–22. http://doi.org/10.1016/j.jclepro.2012.12.037.

6. Boldish, S. I., & White, W. B. (1979). Vibrational spectra of crystals with the A-type rare earth oxide structure—I. La2O3 and Nd2O3. *Spectrochimica Acta Part A: Molecular Spectroscopy*, *35*(11), 1235–1242. http://doi.org/10.1016/0584-8539(79)80204-4.

7. Caravan Peter, Ellison Jeffrey J., McMurry Thomas, L. J. B., & Randall. (1999). Gadolinium(III) chelates as MRI contrast agents: Structure, dynamics, and applications. *Chemical Reviews*, *99*(9), 2293–2352. http://doi.org/10.1021/cr980440x.

8. Caro, P. E., Sawyer, J. O., & Eyning, L. (1972). The infrared spectra of rare earth

carbonates. *Spectrochimica Acta Part A: Molecular Spectroscopy*, *28*(6), 1167–1173. http://doi.org/10.1016/0584-8539(72)80088-6.

9. Chunhui Huang (Ed.). (2010). *Rare Earth Coordination Chemistry: Fundamentals and Applications*.

10. Ericsson, A., Bach-Gansmo, T., Niklasson, F., & Hemmingsson, A. (1995). Combination of gadolinium and dysprosium chelates as a cellular integrity marker in MR imaging. *Acta Radiologica*, *36*(1), 41–46. http://doi.org/10.1177/028418519503600107

11. Feng, P. K., & Fernando, Q. (1962). Stabilities of Divalent Metal Complexes of Certain Substituted 4-Hydroxybenzothiazoles. *Inorganic Chemistry*, *1*(2), 426–427. http://doi.org/10.1021/ic50002a047.

12. Galt, G. E. (2017). *Asorption of Salicylhydroxamic Acid on Selected Rare Earth Oxides and Carbonates*. Montana Tech of the University of Montana.

13. Glushkova, V. B., & Boganov, A. G. (1965). Polymorphism of rare-earth sesquioxides. *Bulletin of the Academy of Sciences, USSR Division of Chemical Science*, *14*(7), 1101–1107. http://doi.org/10.1007/BF00847877.

14. Grasso, V. . (2013). Rare earth elements in national defense: Backgroung, oversight issues, and options for congress. In *Washington, DC .: Congressional Research service*.

15. Guentert, O. J., & Mozzi, R. L. (1958). The monoclinic modification of gadolinium sesquioxide Gd 2 O 3. *Acta Crystallographica*, *11*(10), 746–746. http://doi.org/10.1107/S0365110X58002012.

16. Güntherodt, H. J., Hauser, E., & Künzi, H. U. (1974). The electrical resistivity of rare earth metals at high temperatures and in the liquid state. *Physics Letters A*, *50*(4), 313–314. http://doi.org/10.1016/0375-9601(74)90767-1.

17. Haxel, G.B., Hedrick, J.B., Orris, G. J. (2002). Rare Earth Elements — Critical Resources for High Technology. *United States Geological Survey Fact Sheet*, *087*, 4. http://doi.org/10.1017/CBO9781107415324.004.

18. Jia, Y. Q. (1991). Crystal radii and effective ionic radii of the rare earth ions. *Journal of Solid State Chemistry*, *95*(1), 184–187. http://doi.org/10.1016/0022-4596(91)90388-X.

19. Kim, E., & Osseo-Asare, K. (2012). Aqueous stability of thorium and rare earth metals in monazite hydrometallurgy: Eh-pH diagrams for the systems Th-, Ce-, La-, Nd- (PO4)-(SO4)-H2O at 25 °c. *Hydrometallurgy*, *113–114*, 67–78. http://doi.org/10.1016/j.hydromet.2011.12.007.

20. Krishnamurthy, N., & Gupta, C. K. (2015). *Extractive metallurgy of rare earths. CRC press.* (CRC Press).

21. LaDouceur, R. (2018). *High Fidelity Model for Flotation: Applications to Rare Earth Elements and Copper/Molybdenum Separations*. Montana Tech of the University of Montana.

22. Legvold, S. (1980). *Rare earth metals and alloys. Handbook of Ferromagnetic Materials* (1st ed.).

23. Mackintosh, A. R. (1991). *Rare earth magnetism: structures and excitations.* Clarendon Press.

24. Paton, M. G., & Maslen, E. N. (1965). A refinement of the crystal structure of yttria. *Acta Crystallographica*, *19*(3), 307–310. http://doi.org/10.1107/S0365110X65003365.

25. Pavez O., Brandao P. R. G., & P. A. E. C. (1996). Technical note adsorption of oleate and octyl-hydroxamate on to rare-earths minerals. *Minerals Engineering, 3*(9), 357–366.

26. Pearson, R. G. (1963). Hard and Soft Acids and Bases. *Journal of the American*

Chemical Society, *85*(22), 3533–3539. http://doi.org/10.1021/ja00905a001.

27. Shinn, D. B., & Eick, H. A. (1968). The Crystal Structure of Lanthanum Carbonate Octahydrate. *Inorganic Chemistry*, *7*(7), 1340–1345. http://doi.org/10.1021/ic50065a018.

28. Sreenivas, T., & Padmanabhan, N. P. H. (2002). Surface chemistry and flotation of cassiterite with alkyl hydroxamates. *Colloids and Surfaces A: Physicochemical and Engineering Aspects*, *205*(1–2), 47–59. http://doi.org/10.1016/S0927-7757(01)01146-3.

29. Thiel, C. W. (2003). *Energies of Rare-Earth Ion States Relative Host Bands in Optical Materials from Photoemission Spectroscopy*. University of Montana.

30. Trant, S. (2018). *Adsorption of Salicylhydroxamic acid on the surface of selected rare earth carbonates and phosphates*. Montana Technological University.

31. Warshaw, I., & Roy, R. (1961). Polymorphism of the Rare Earth Sesquioxides. *Journal of Physical Chemistry*, *65*(11), 2048–2051. http://doi.org/10.1021/j100828a030.

32. William Zachariasen. (1926). Die KristallStruktur der A-Modifikation von den Sesquioxyden de Seltenen Erdmetalle. (La2O3,Ce2O3,Pr2O3,Nd2O3). *ZeitSchrift Fur Physikalische Chemie*, *123U*(1), 134–150. http://doi.org/1926-12309.

33. Wyckoff, R. W. G. (1963). *Crystal structure of uraninite*. *Crystal Structures 1*. Retrieved from http://www.scirp.org/(S(oyulxb452alnt1aej1nfow45))/reference/ReferencesPapers.aspx?ReferenceID=1952937.

34. Yunxiang Ni, Hughes, J. M., & Mariano, A. N. (1995). Crystal chemistry of the monazite and xenotime structures. *American Mineralogist*, *80*(1–2), 21–26. http://doi.org/0003-004X/95/0102-0021.

35. Zachariasen, W. (1927). The Crystal Structure of the Modification of C of the

sesquioxides of rare earth metals, and of indium and Thallium. *Norsk Geologisk Tidsskrift*, *9*, 310–316.

36. Zachariasen, W. (1928). Untersuchen ueber die KristallStruktur von Sesquixyden und Verbindungen ABO3. *Skrifter Utgitt Av Det Norske Videnskaps i Oslo*, *1*, 1–165.

37. Gordon Haxel, USGS, https://www.sigmaaldrich.com/technical-documents/articles/materials-science/rare-earth-crisis.html (last assessed 11/2018)

38. Atkinson, S. C. (2014). *Crystal structures and phase transitions in the rare earth oxides* (Doctoral dissertation, University of Salford).

10. Appendix A: Final Titration Plots

Titration of the water used to prepare SHA⁻ solution 2nd run

titration of the water used to prepare Ob- solution 3rd run

Titration of 5.352x10^{-3} M SHA$^-$ with 0.0518 M HCl, second run

titration of 5.352x10^{-3} M SHA$^-$ with 0.0518 M HCl, third run

titration of 5.352x10^{-3} M SHA$^-$ with 0.0518 M HCl, fourth run
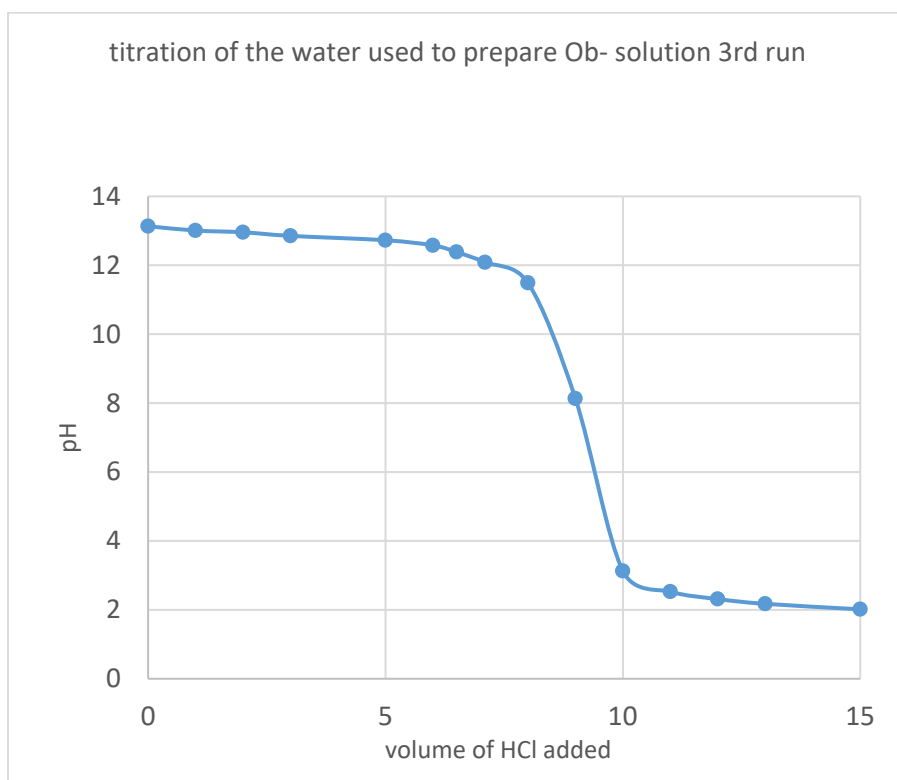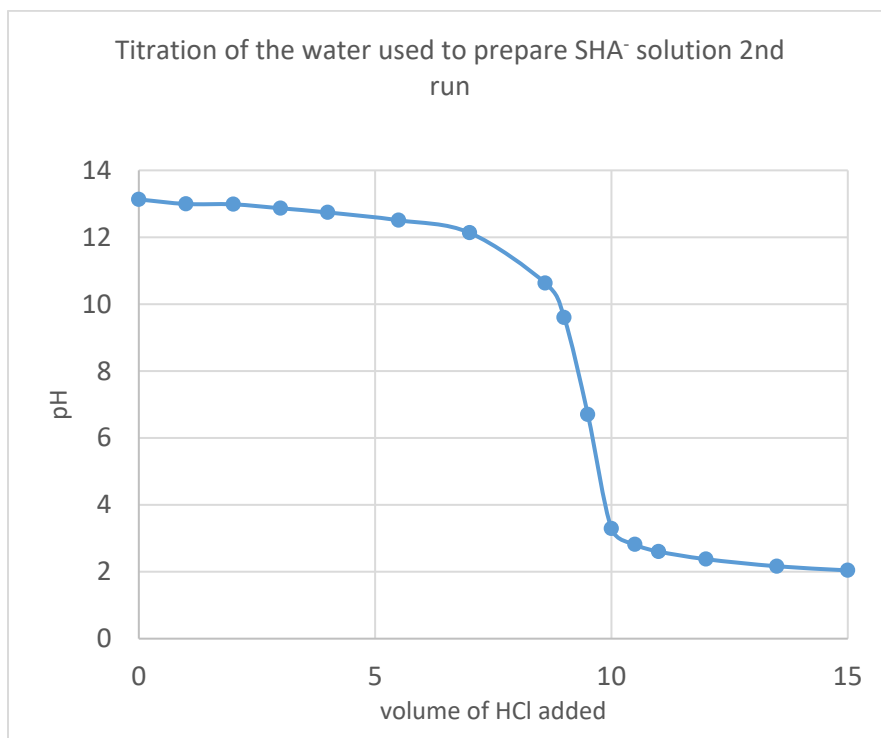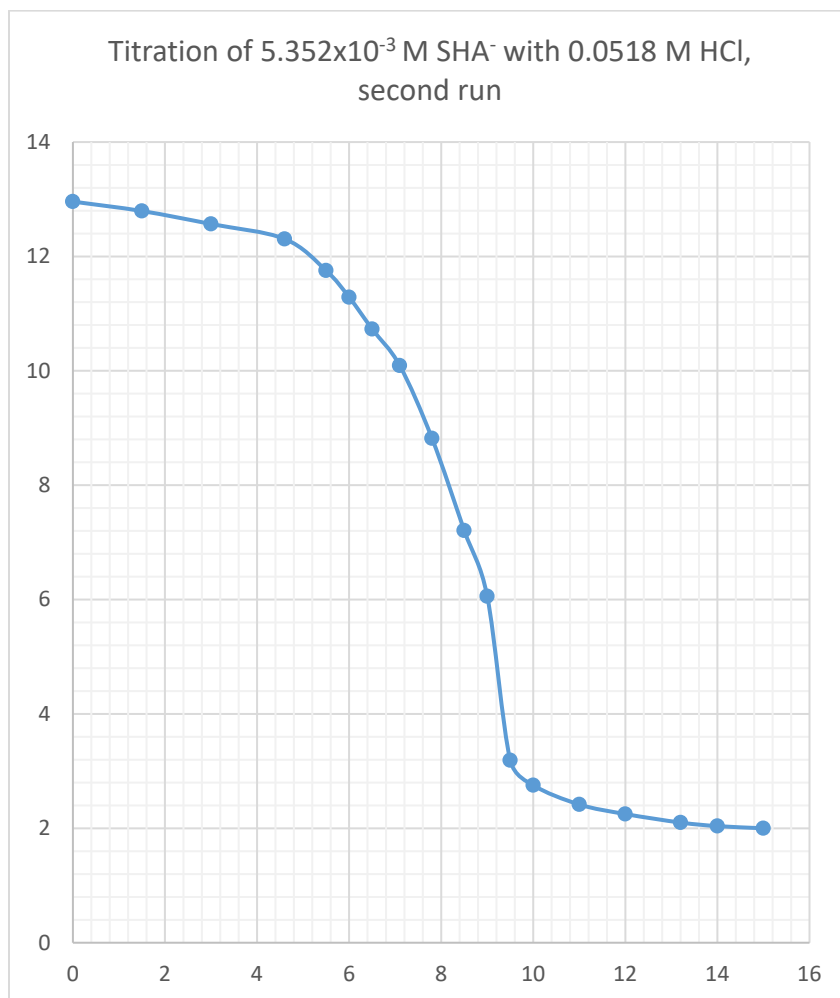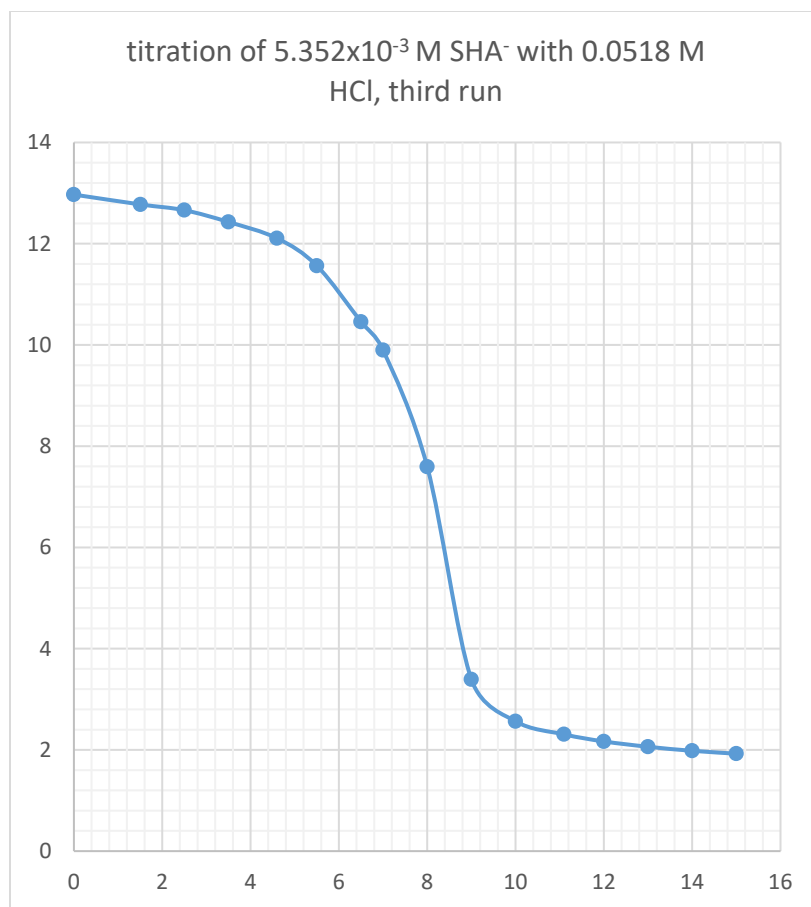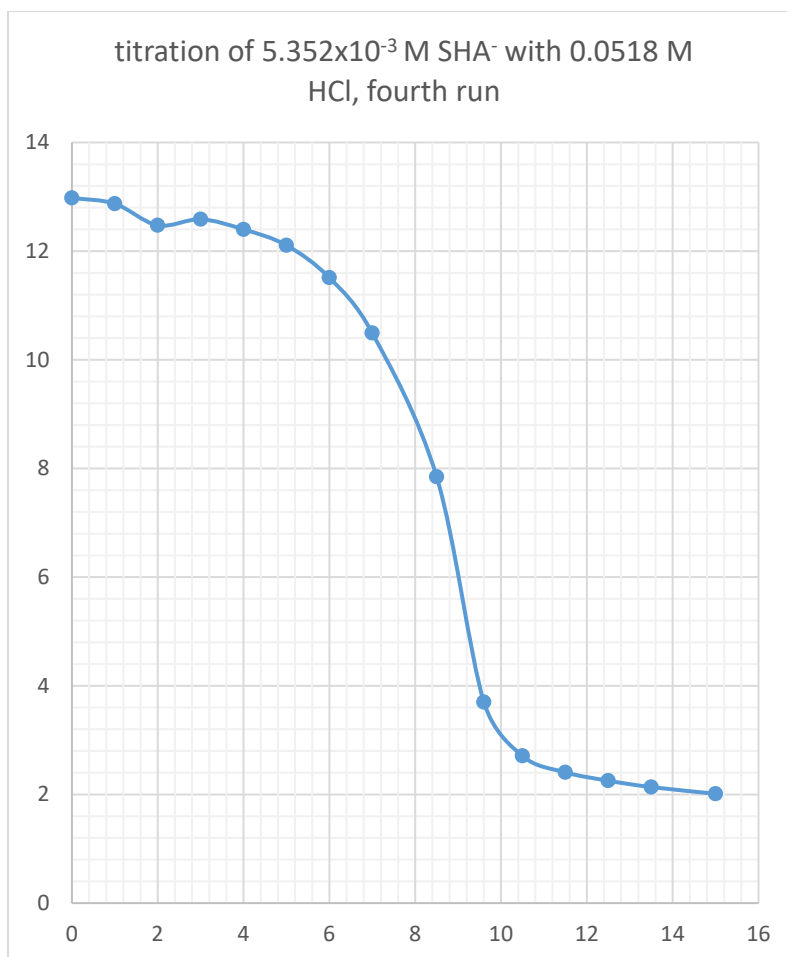
11. Appendix B: Preliminary Titration Plots

6.7×10^{-2} M SHA$^-$ with 0.21M HCl titration first run

6.7x10^{-2} M SHA$^-$ with 0.21M HCl titration , second run

6.7x10^{-2} M SHA^{-} with 0.21M HCl titration , third run

6.7x10^{-2} M SHA$^-$ with 0.21M HCl titration , fourth run

6.7×10^{-2} M SHA⁻ with 0.21M HCl titration , fifth run
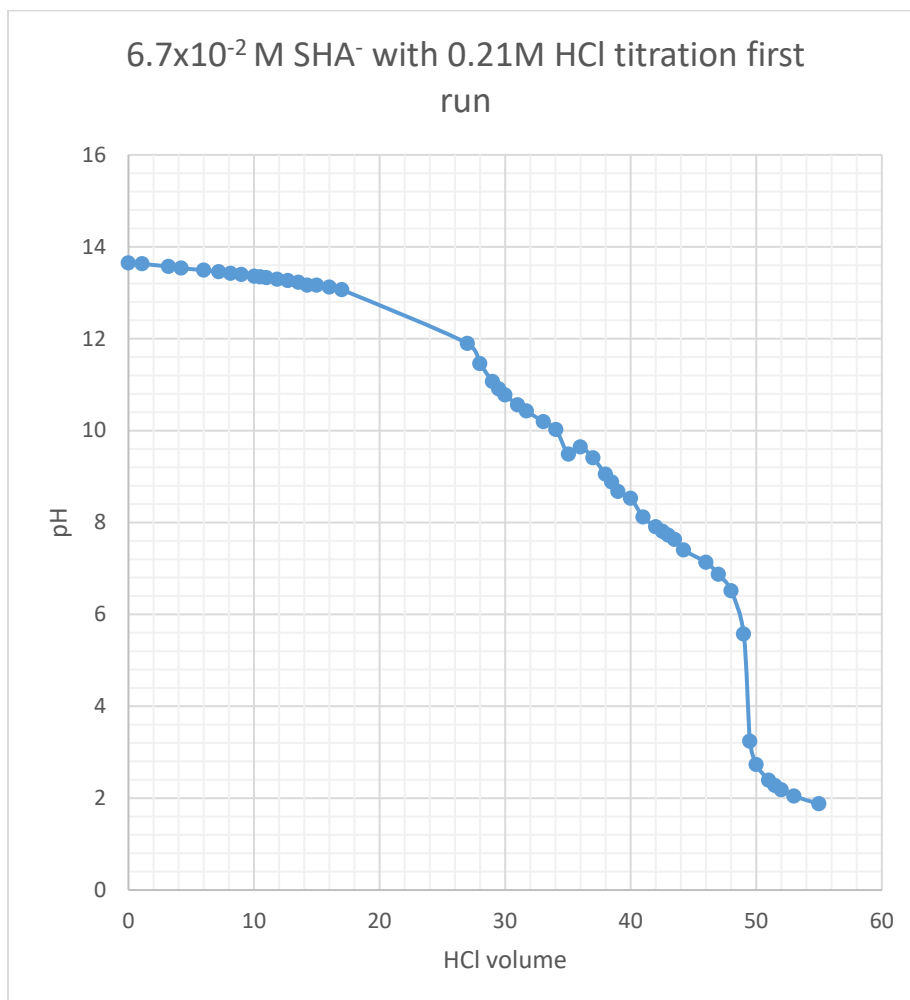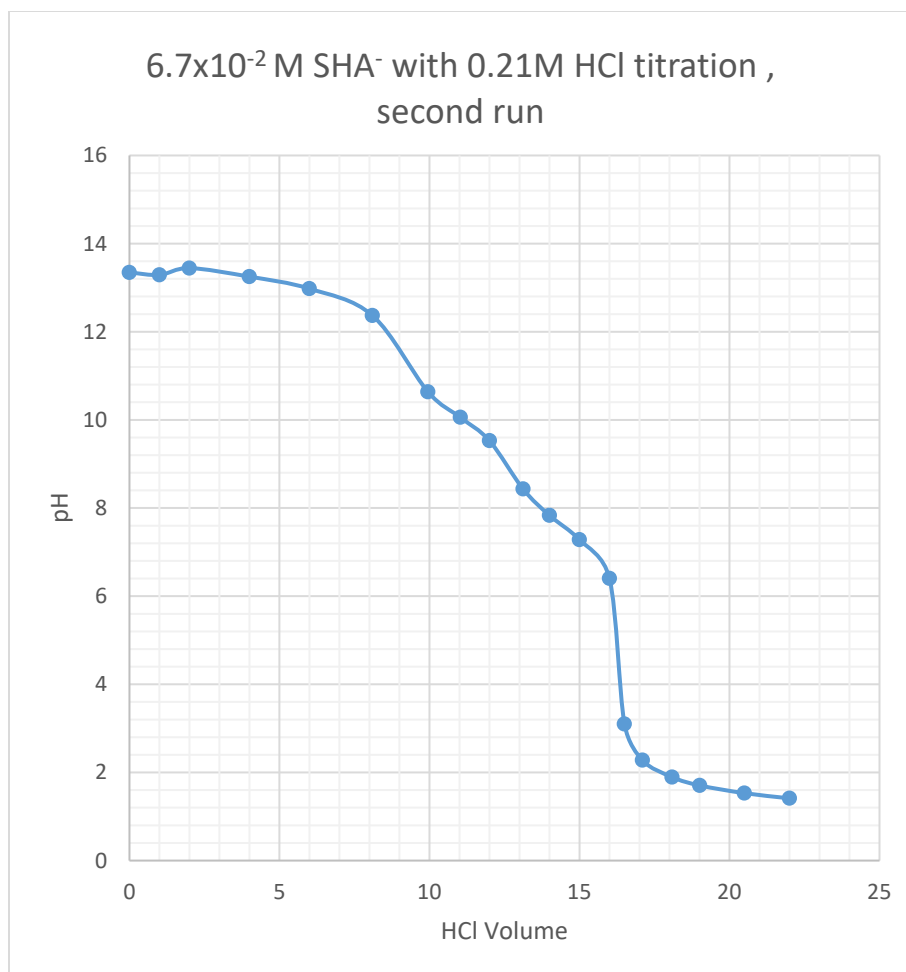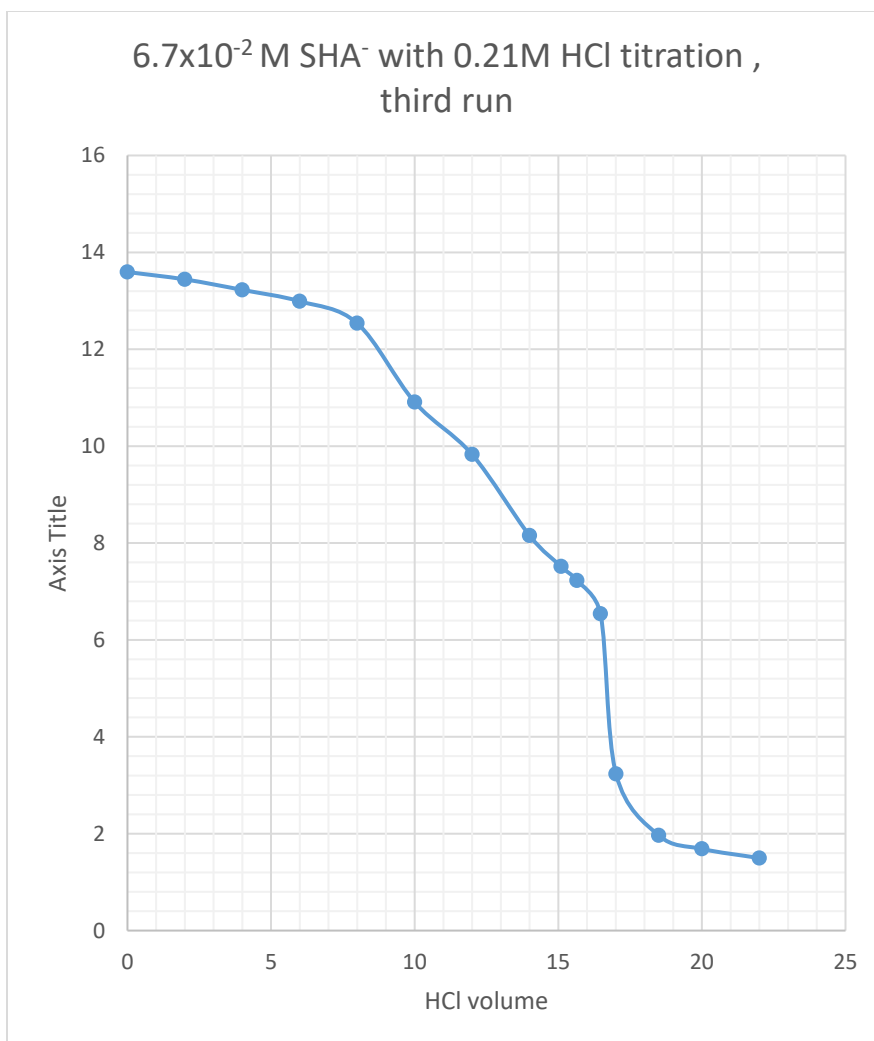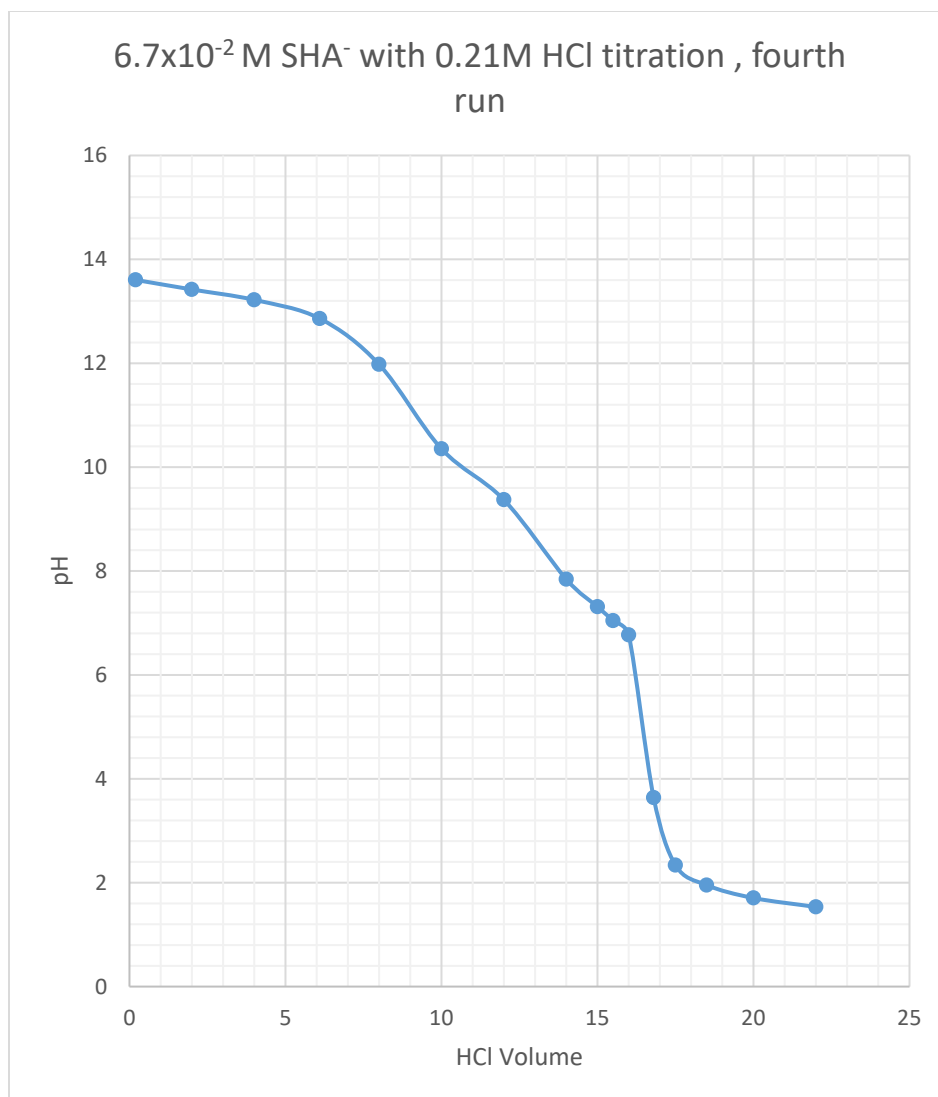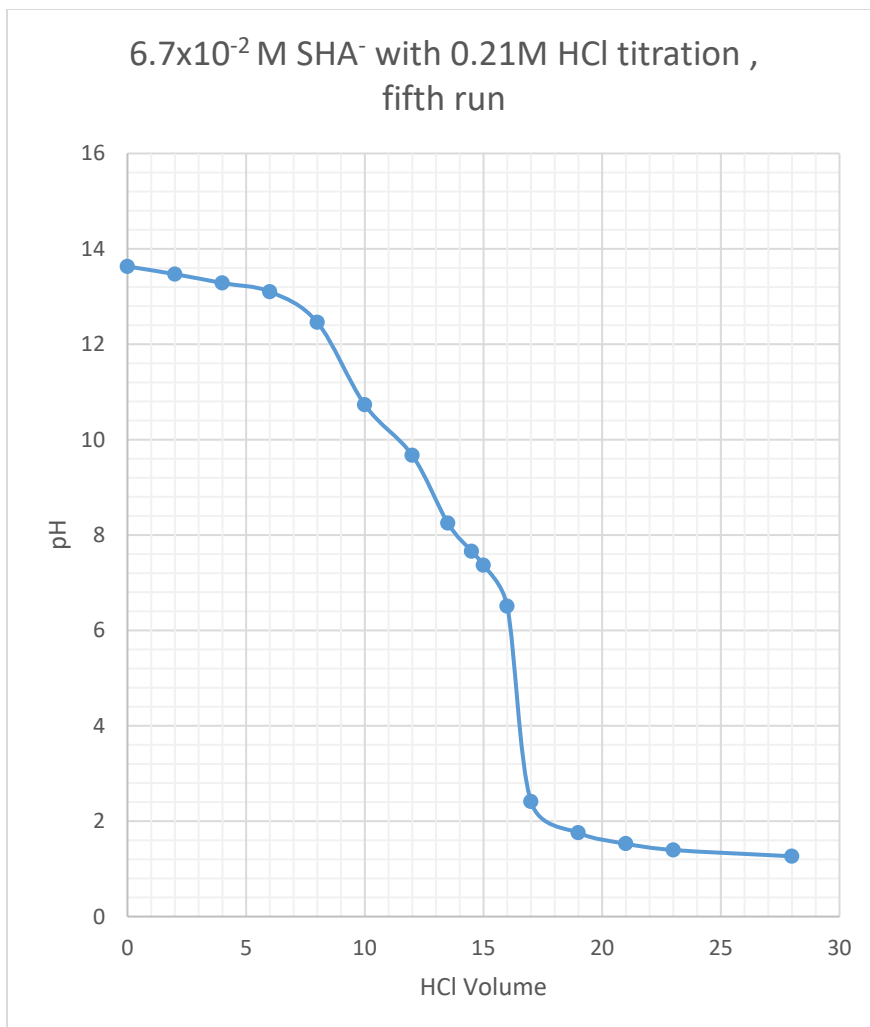
SIGNATURE PAGE

This is to certify that the thesis prepared by Marc Freddy Sime entitled "Surface Chemistry and Modelling of Salicyl Hydroxamic Acid at the Surface of Rare Earth Oxides, Carbonates and Phosphates" has been examined and approved for acceptance by the Department of Metallurgical and Materials Engineering, Montana Technological University, on this 15th day of November, 2018.

_____

Courtney A. Young, PhD, Professor
Department Head
Metallurgical and Materials Engineering
Chair, Examination Committee

_____

Avimanyu Das, PhD, Associate Professor
Metallurgical and Materials Engineering
Member, Examination Committee

_____
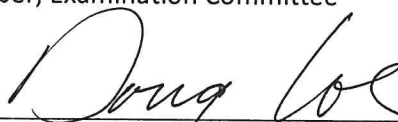
Doug Coe, PhD, Professor Emeritus of Physical Chemistry
Department of Chemistry and Geochemistry
Member, Examination Committee